CT-free Total-body PET segmentation

Song Xue, Christoph Clement, Marco Viscione, Rui Guo, Axel Rominger, Biao Li, Kuangyu Shi

- Low-dose PET => CT-based PET attenuation and scatter correction
- CT est important pour l'attenuation and scatter correction
- Mais le CT ajoute une dose importante de radiation
- <u>But:</u> Segmentation multi-organes corps entier à partir des images PET non corrigées
- Première étape vers du "true CT-free PET"

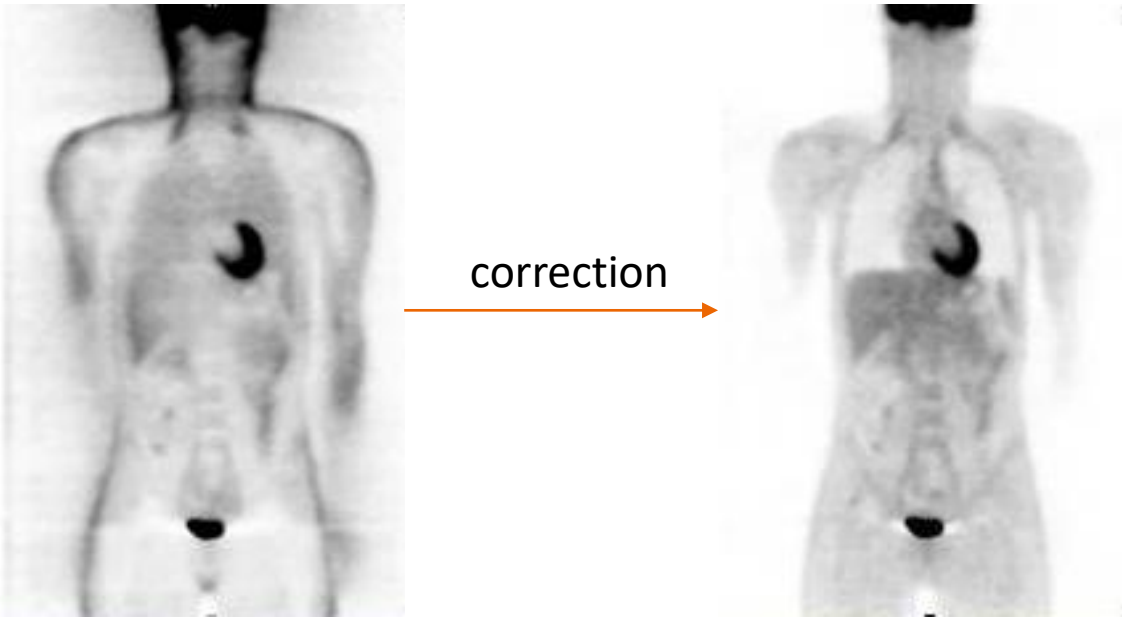

CT-free Total-body PET segmentation

Song Xue, Christoph Clement, Marco Viscione, Rui Guo, Axel Rominger, Biao Li, Kuangyu Shi

- 18F-FDG PET/CT corps entier de 114 patients
- Ground truth génerée par MOOSE sur les images CT images
- nnU-Net architecture
- Entraîné sur les non-attenuation and non-scatter corrected PET images
- Average DICE : 0,82
- Trois médecins nucléaires ont confirmé que les segmentations étaient fiables

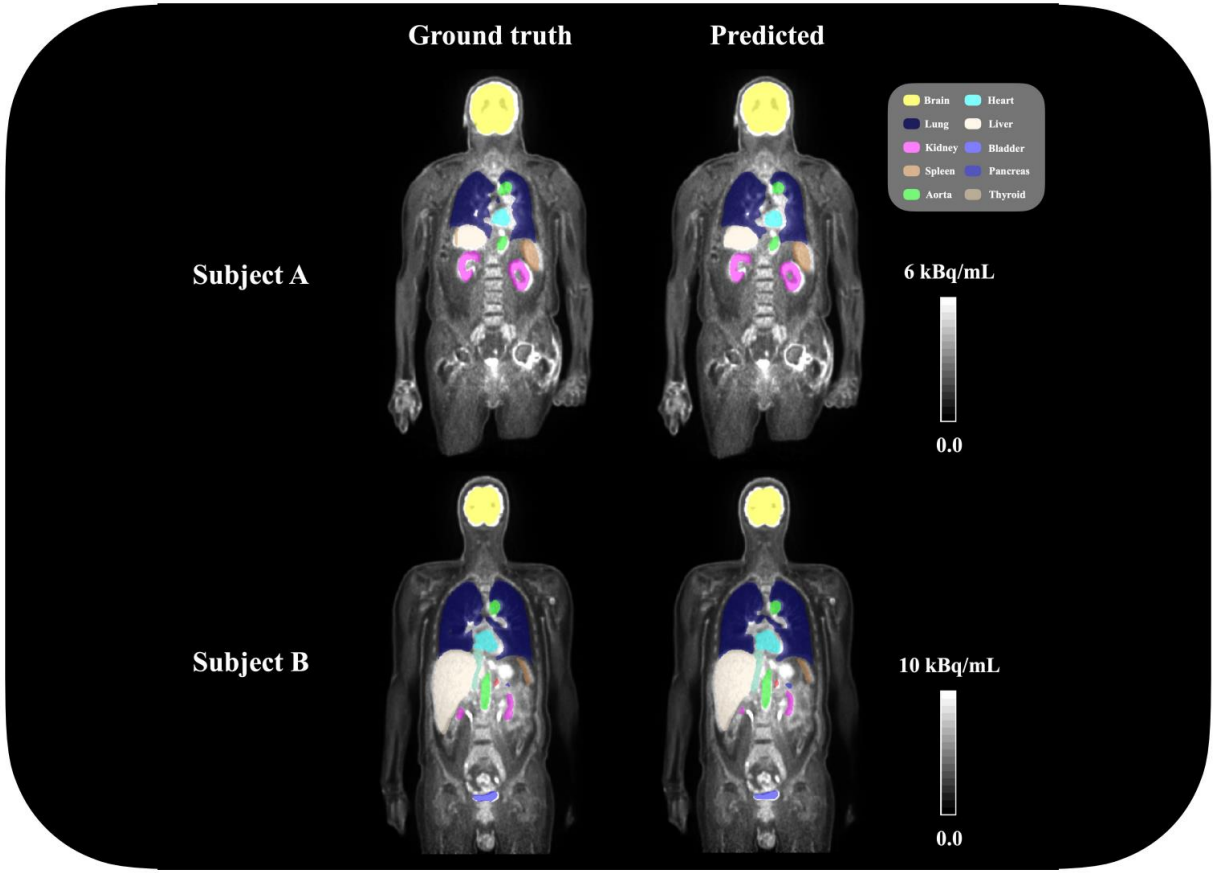

CT-free Total-body PET segmentation

Song Xue, Christoph Clement, Marco Viscione, Rui Guo, Axel Rominger, Biao Li, Kuangyu Shi

- Average DICE : 0,82
- 70% des organs ont un DICE > 0,80
- Mais il y en a des plus difficiles:
  - Vessie (0,70)
  - Thyroïde (0,69)
  - Pancréas (0,59)
- Développements futurs:
  - Délinéation manuelle des organes
  - Données d'autres scanners

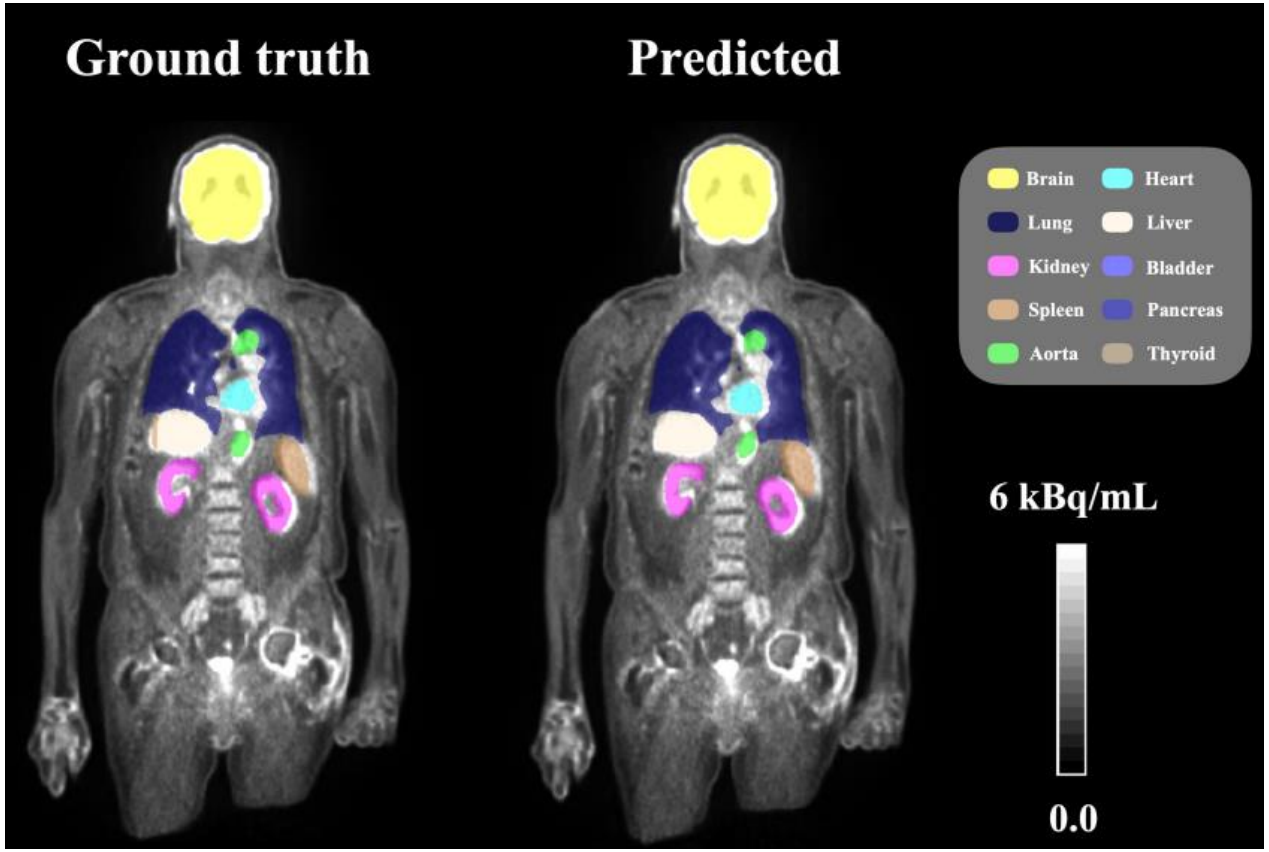

Deep learning-based synthesis of whole-body contrast-enhanced-like CT images from dynamic PET and low-dose CT images using long axial field-of-view PET/CT scanners

Hasan Sari, Ian L. Alberts, Clemens Mingels, Kuangyu Shi, Axel Rominger

- Contrast-enhanced CT (ceCT): administration d'un agent de contraste à base d'iodine
- Améliore l'interprétation morphologique des lésions
- Améliore la délinéation des vaisseaux et des tissus mous
- Problèmes:
  - Réactions allergiques
  - Contre indiqué chez les patients avec d'insuffisances rénales ou de problème de thyroïde
  - Inconfortable
  - Plus grande dose de radiations
- <u>But:</u> déterminer l'image ceCT à partir du PET et du neCT

Reactions to iodinated contrast media
(Tasker F. et al., Clin. Exp. Dermatol., 2019)

Deep learning-based synthesis of whole-body contrast-enhanced-like CT images from dynamic PET and low-dose CT images using long axial field-of-view PET/CT scanners

Hasan Sari, Ian L. Alberts, Clemens Mingels, Kuangyu Shi, Axel Rominger

- 10 patients (cross validation 8/2)
- Biograph Vision Quadra
- 2D Residual Unet model
- Prédiction sur les 2D axial slices

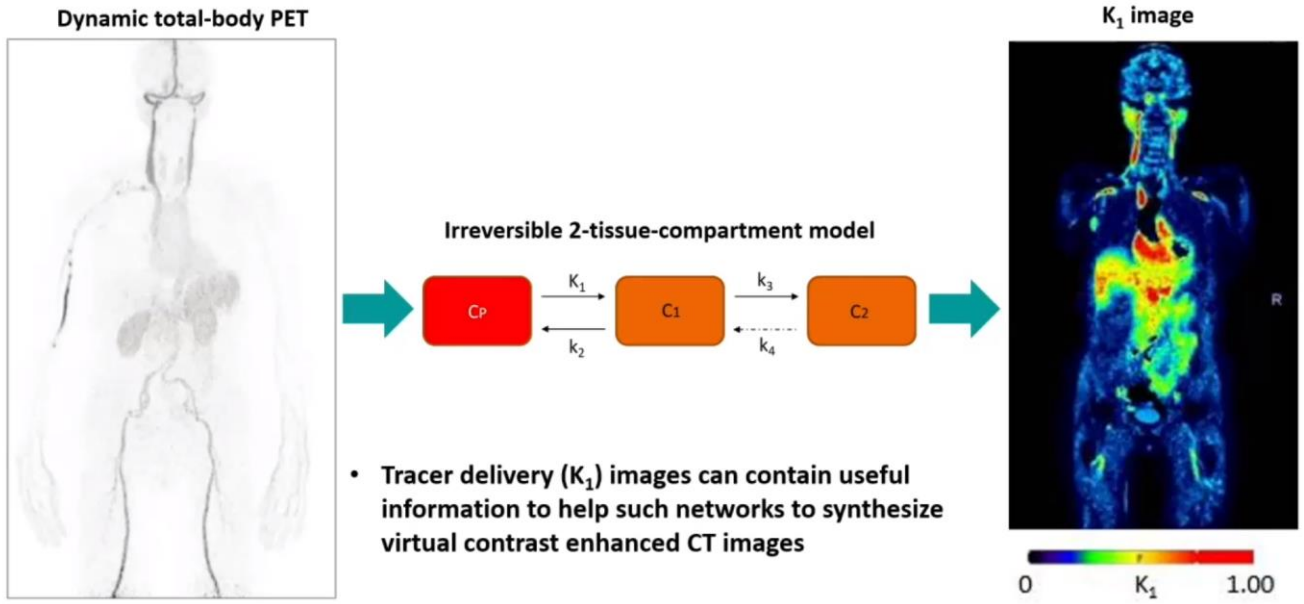

Deep learning-based synthesis of whole-body contrast-enhanced-like CT images from dynamic PET and low-dose CT images using long axial field-of-view PET/CT scanners

Hasan Sari, Ian L. Alberts, Clemens Mingels, Kuangyu Shi, Axel Rominger

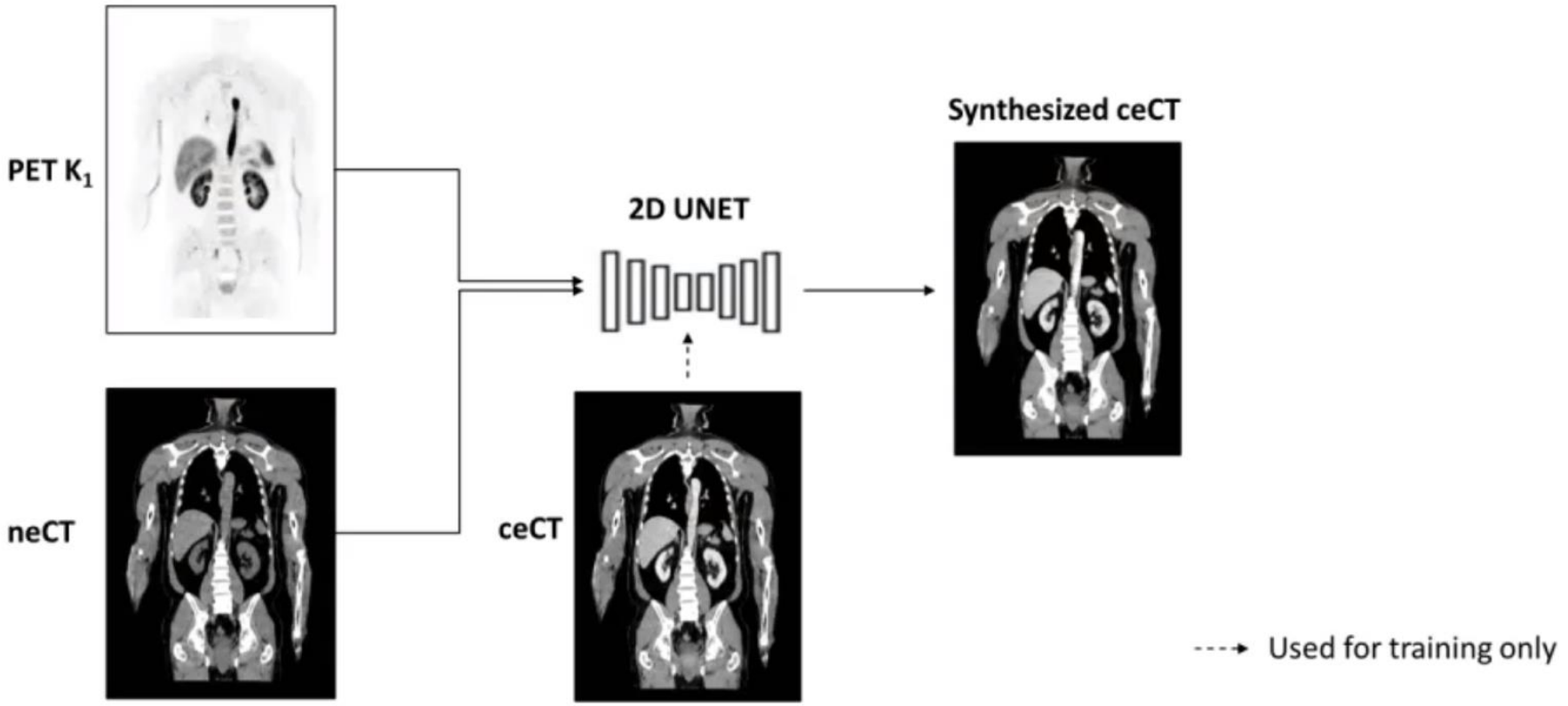

Deep learning-based synthesis of whole-body contrast-enhanced-like CT images from dynamic PET and low-dose CT images using long axial field-of-view PET/CT scanners

Hasan Sari, Ian L. Alberts, Clemens Mingels, Kuangyu Shi, Axel Rominger

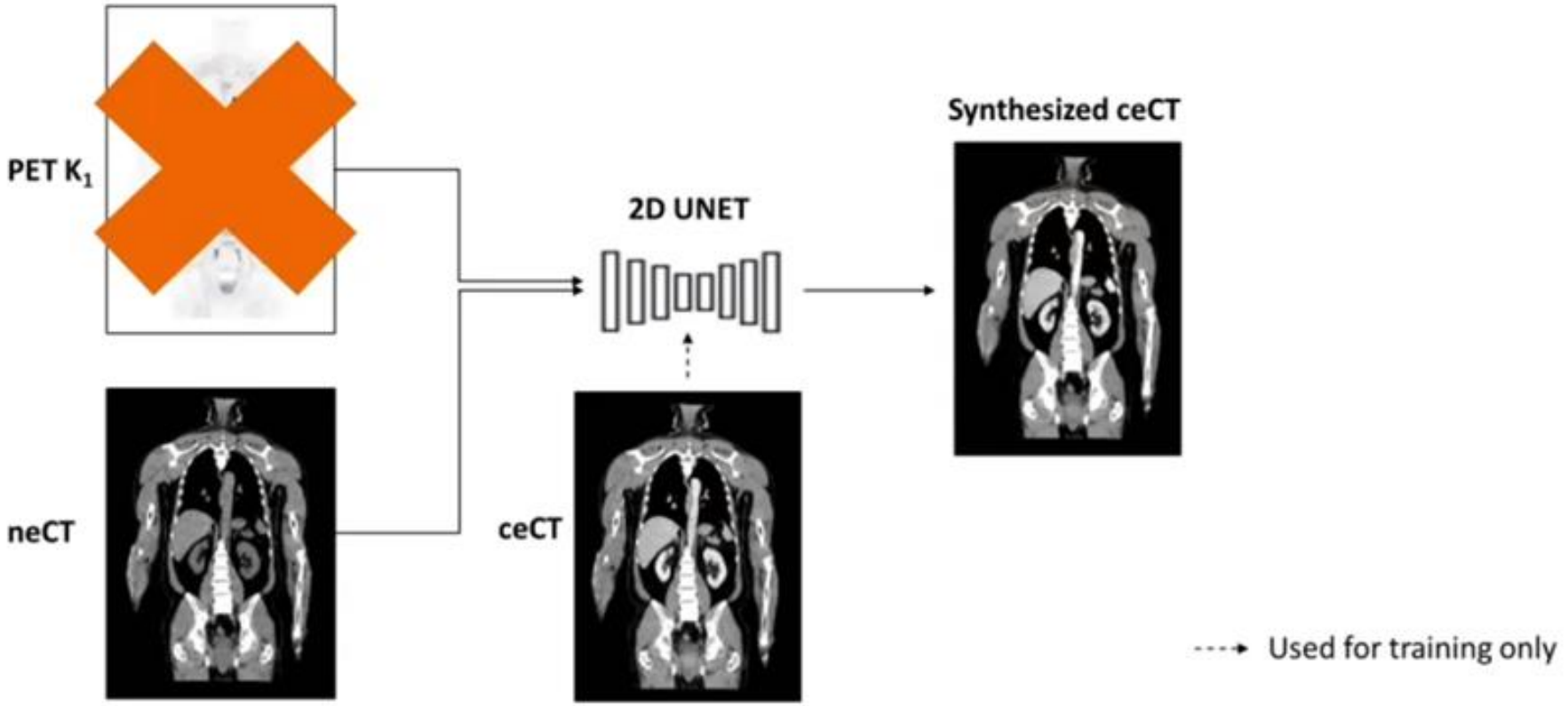

Deep learning-based synthesis of whole-body contrast-enhanced-like CT images from dynamic PET and low-dose CT images using long axial field-of-view PET/CT scanners

Hasan Sari, Ian L. Alberts, Clemens Mingels, Kuangyu Shi, Axel Rominger

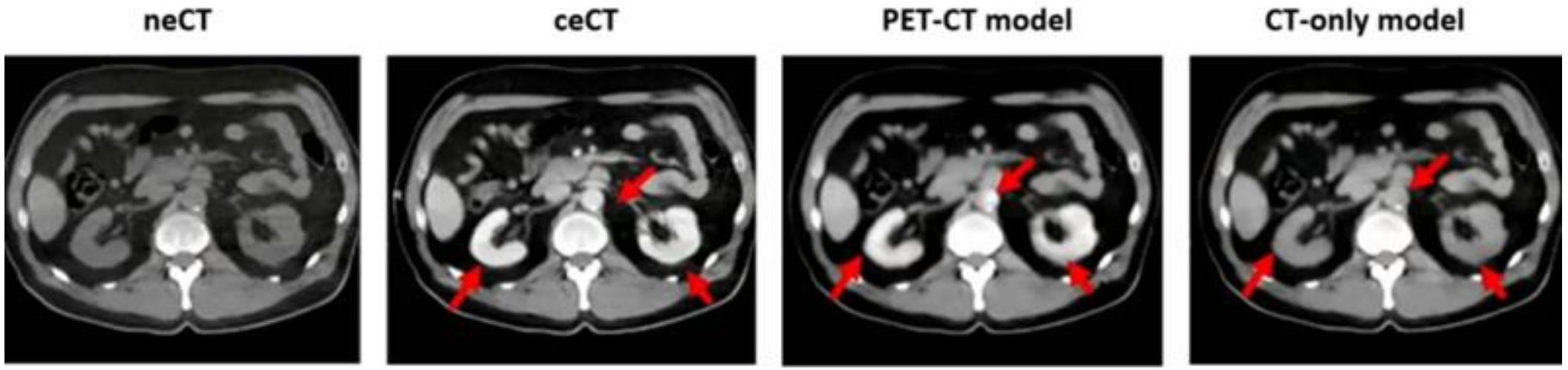

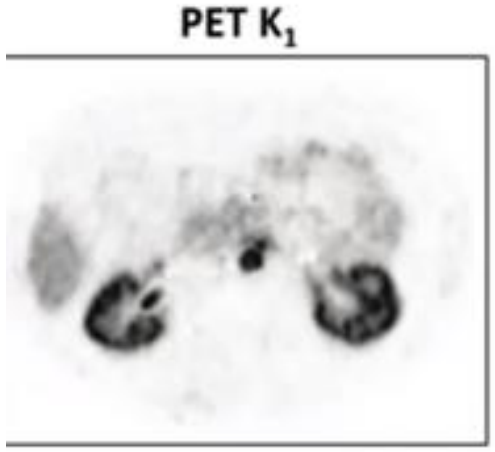

Better renal contrast in the images generated with the PET+CT model

Deep learning-based synthesis of whole-body contrast-enhanced-like CT images from dynamic PET and low-dose CT images using long axial field-of-view PET/CT scanners

Hasan Sari, Ian L. Alberts, Clemens Mingels, Kuangyu Shi, Axel Rominger

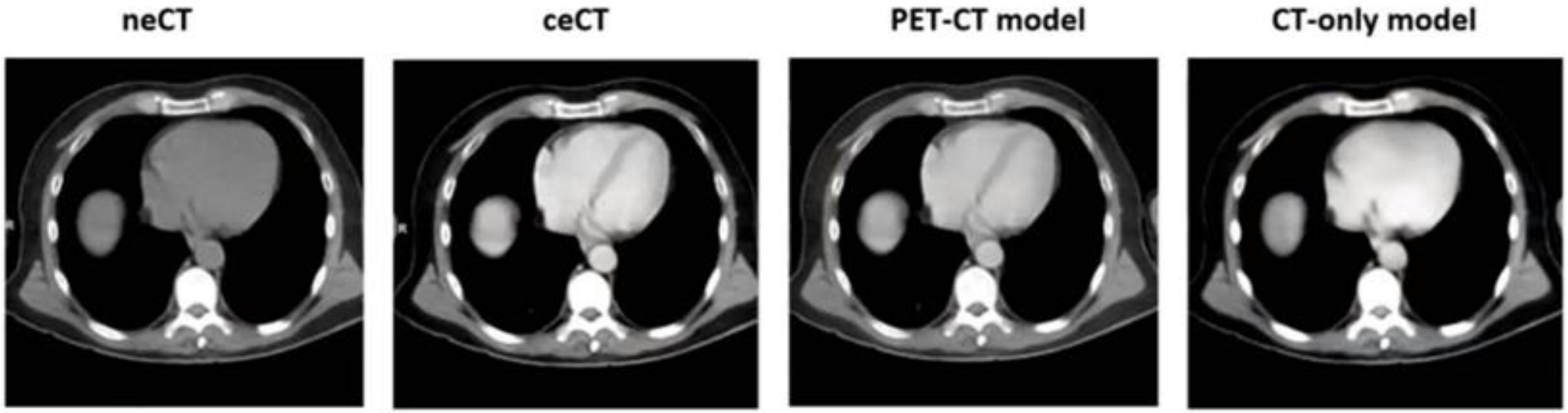

High contrast of vascular versus non vascular structures - the CT-only model could not reproduce this

Deep learning-based synthesis of whole-body contrast-enhanced-like CT images from dynamic PET and low-dose CT images using long axial field-of-view PET/CT scanners

Hasan Sari, Ian L. Alberts, Clemens Mingels, Kuangyu Shi, Axel Rominger

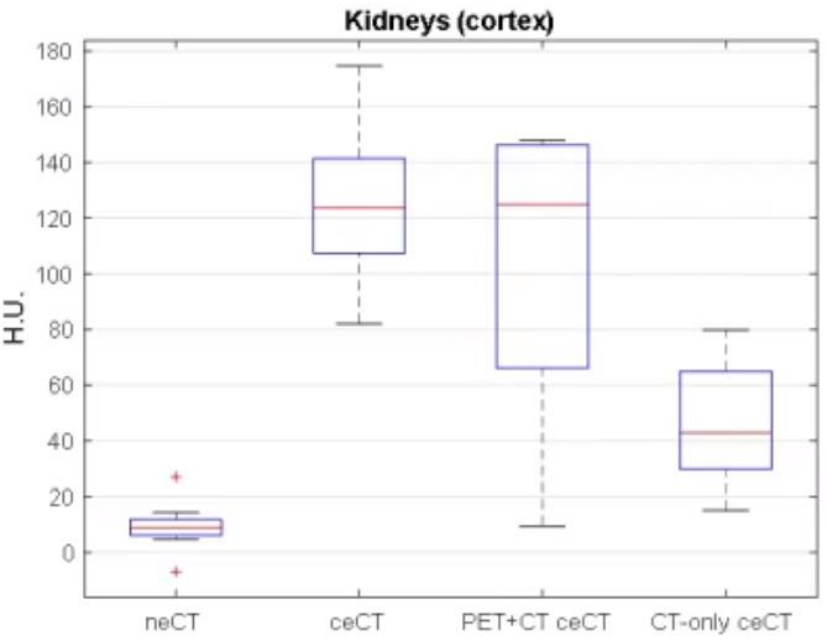

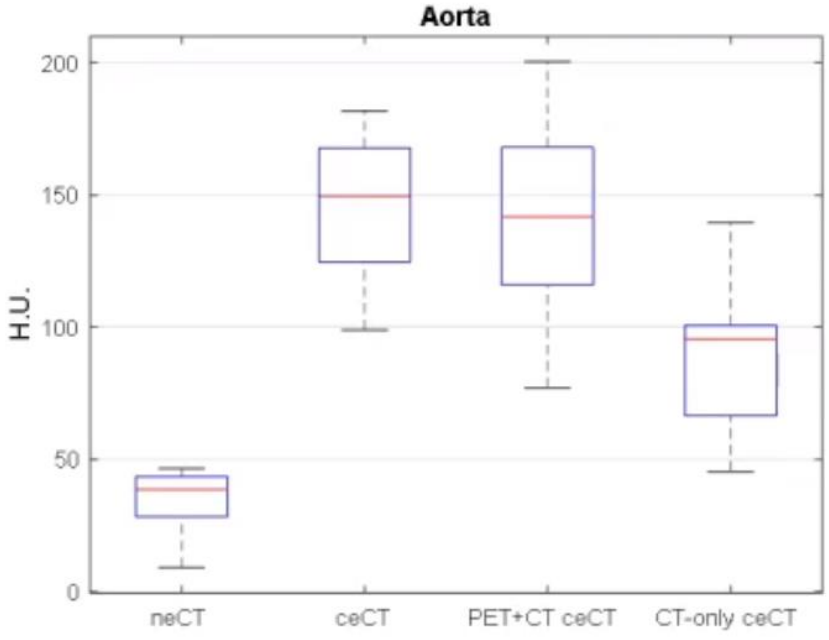

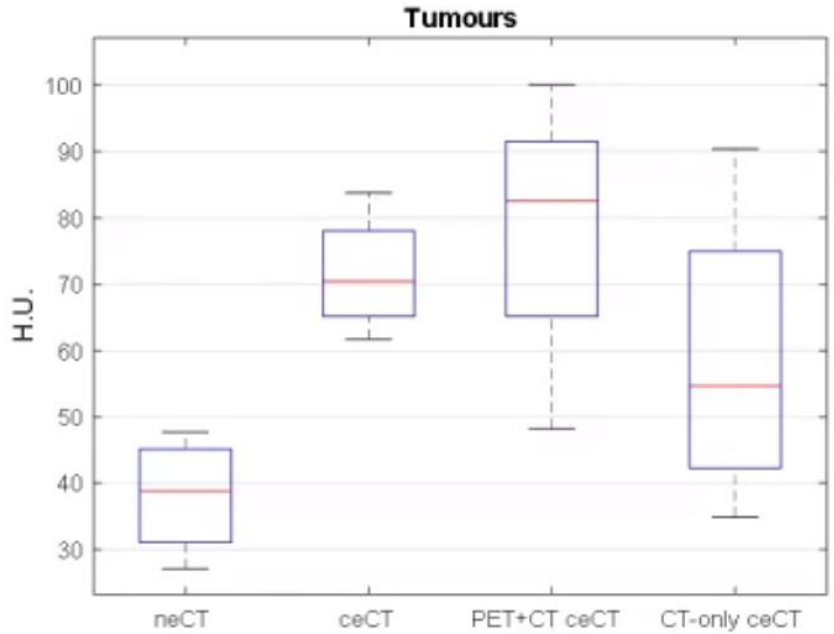

Nicolas

SNMMI 2023

institut Curie

Inserm
La science pour la santé
From science to health

LITO

Poster 1: generate radiomic features not images

Improving treatment response prediction in lymphoma patients by generating synthetic [18F]-FDG-PET radiomic features using CTGAN

Yashar Ahmadyar[1], Rezvan Samimi[1], Alireza Kamali-Asl[1], Parham Geramifar[2]

[1] Department of Medical Radiation Engineering, Shahid Beheshti University, Tehran, Iran.
[2] Research Center for Nuclear Medicine, Shariati Hospital, Tehran University of Medical Sciences, Tehran, Iran.

June 24-27 2023 SNMMI ANNUAL MEETING Chicago, Illinois, USA

*From 45 lymphoma patients (75 responders and 51 non-responders to neoadjuvant chemotherapy)

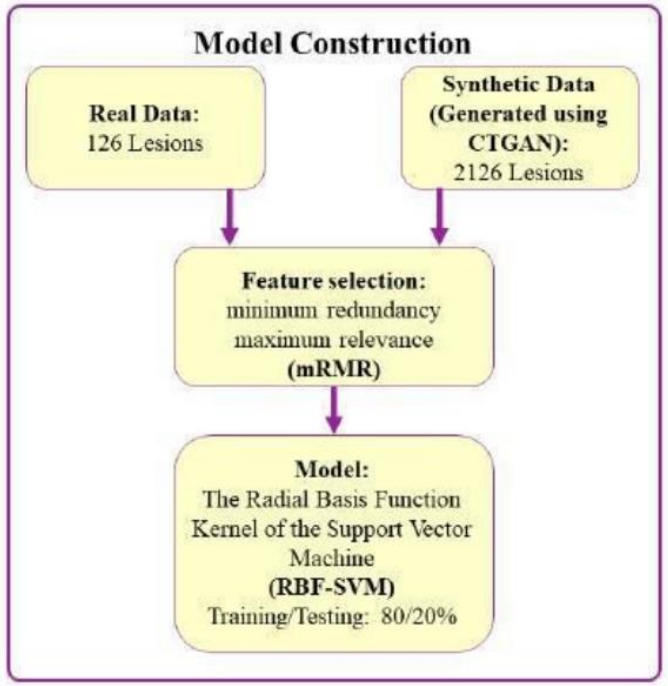

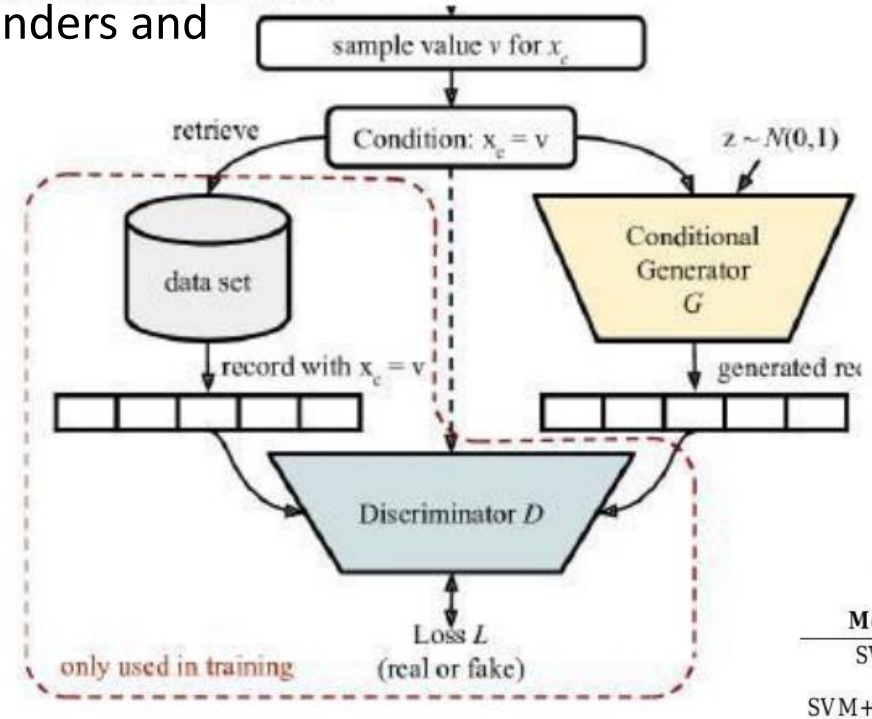

TABLE 1. Evaluation Metrics for SVM and SVM+CTGAN models

Model	ACC	AUC	SEN	SPE
SVM	84%	85%	88%	72%
SVM+CTGAN	92%	92%	92%	91%

"How to Generate Real-World Synthetic Data with CTGAN" - Miriam Santos – TowardsDataScience

Poster 2: leverage unsupervised learning for new discoveries ?

Annotation-free deep representation learning for automated cardiac amyloidosis detection on ^{99m}Tc scintigraphy

Clemens P. Spielvogel[1*], David Haberl[1*], Jing Ning[2], Tatjana Traub-Weidinger[1], Rhodri H. Davies[3,5], Iain Pierce[3,5], Kush Patel[5], Kilian Kluge[1], Thomas Nakuz[1], Adelina Göllner[1], Dominik Amareller[1], Michael Weber[1], Min Zhao[1], Xiaowei Ma[7], Xiang Li[1], Alexander R. Haug[1], Raffaella Calabretta[1], Leon Menezes[5], Roberto Sciagra[8], Thomas Treibel[3,5], Marcus Hacker[1] and Christian Nitsche[3,4,5]

MEDICAL UNIVERSITY OF VIENNA

*~16000 patients with 99mTC scintigraphy scans (4 different tracers, 9 centers, 10 scanners…)

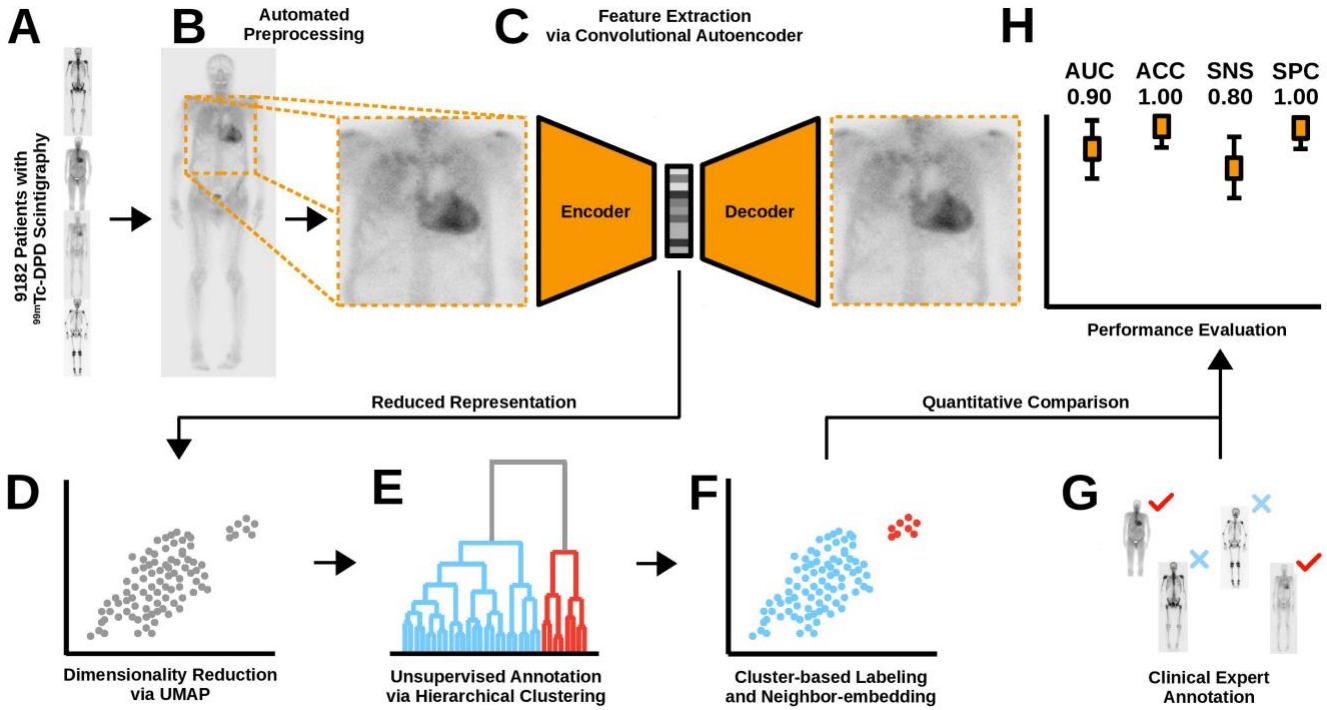

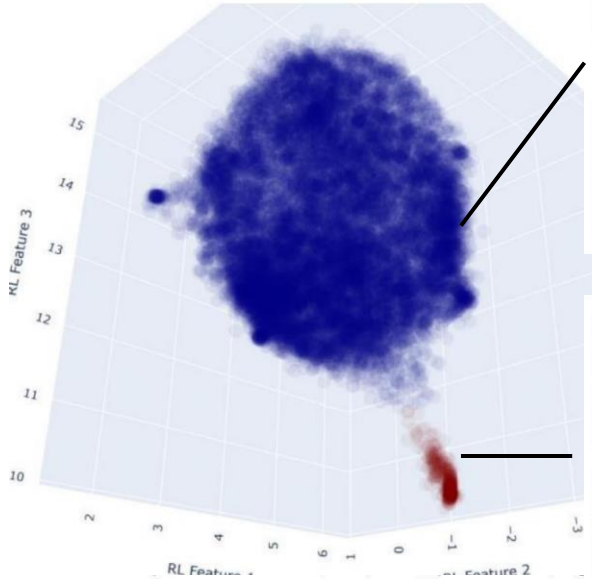

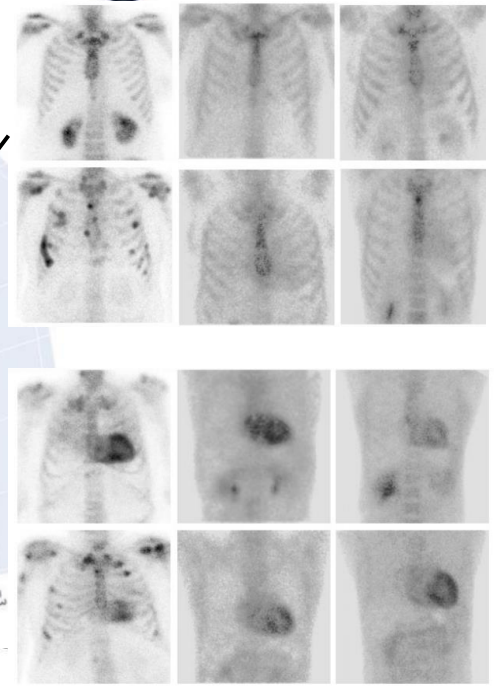

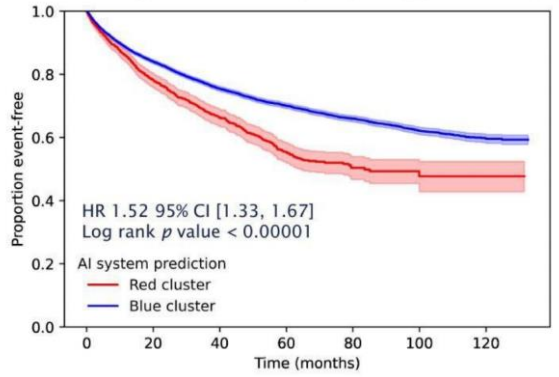

Poster 3: multimodal approach and interpretation strategies

MICHIGAN STATE UNIVERSITY

Adaptable Feature Importance Estimation Framework for Fusion-based Multimodal Deep Neural Networks

Muneeza Azmat*, Henry Fessler, Adam M. Alessio
Michigan State University

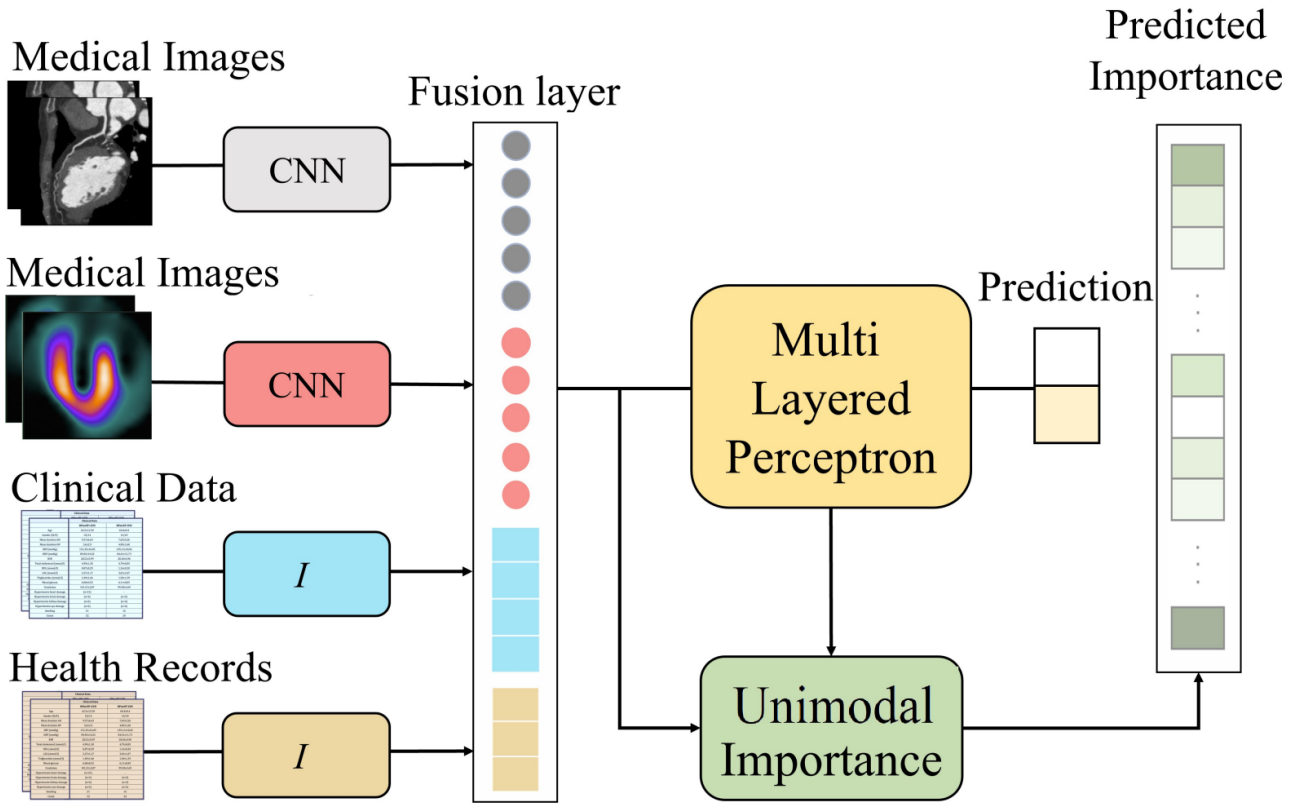

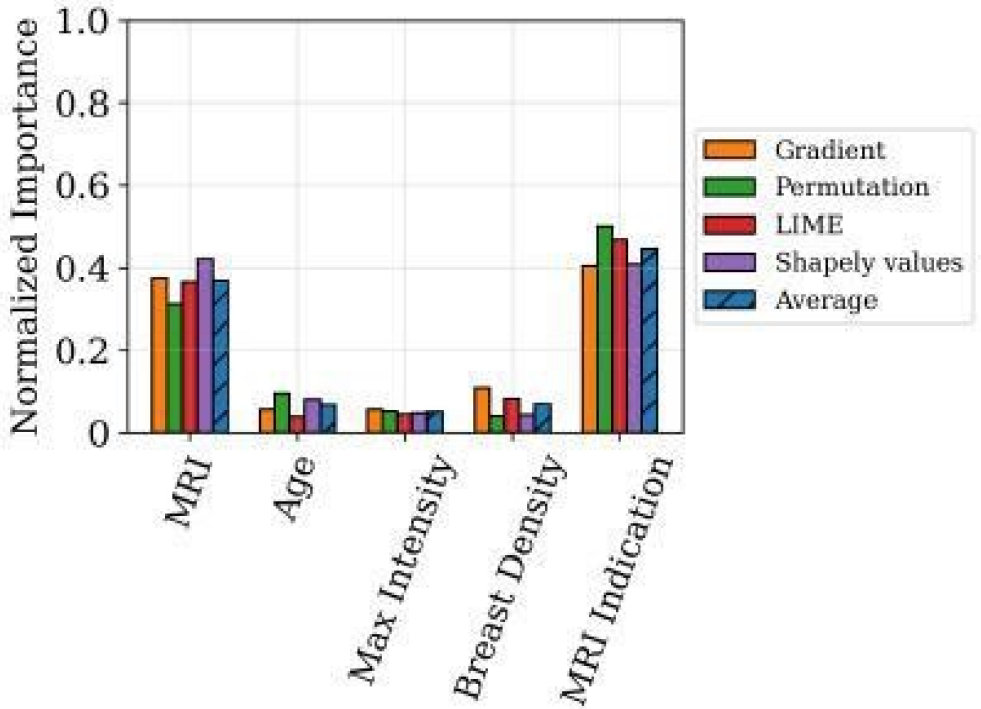

Predict malignancy for 5248 women who underwent breast examination (from DCE MRI exam and clinical data)

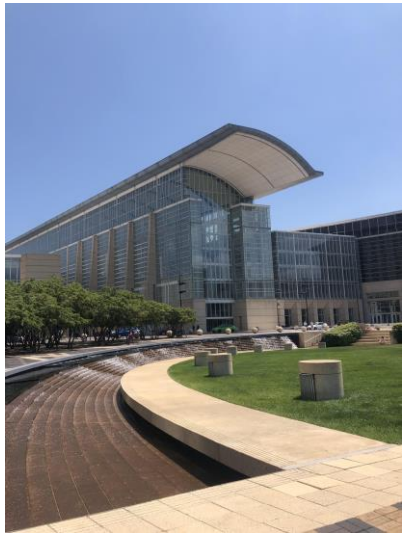

Retour congrès SNMMI

Julie - 07/06/2023

June 24-27 2023 SNMMI ANNUAL MEETING CHICAGO Illinois, USA
EYE ON THE PATIENT

#1

FDG PET/CT tumor dissemination characteristic predicts the outcome of first-line systemic therapy in non-small cell lung cancer

Weiyue Tan[1,2], Yi Zhang[1,2], Jie Wang[1,2], Zhonghang Zheng[1,2], Ligang Xing[3] , Xiaorong Sun[2]
[1] Department of Graduate, Shandong First Medical University and Shandong Academy of Medical Sciences, Jinan, Shandong, China
[2] Department of Nuclear Medicine, Shandong Cancer Hospital and Institute, Shandong First Medical University and Shandong Academy of Medical Sciences, Jinan, Shandong, China
[3] Department of Radiation Oncology, Shandong Cancer Hospital and Institute, Shandong First Medical University and Shandong Academy of Medical Sciences, Jinan, Shandong, China

Objectif : étudier la corrélation entre les caractéristiques de la dissémination tumorale sur les images TEP/TDM au 18F-FDG et la réponse au traitement du cancer du poumon non à petites cellules (NSCLC) de stade IV.

Méthodes :

- 101 patients NSCLC:
  - Examen pré-thérapeutique TEP/TDM au 18F-FDG
  - Données cliniques : âge, sexe, statut tabagique, histologie (adénocarcinome, squameux, autres)
  - Données radiomiques (lésion primaire + métastases) : SUVmax, SUVmean, TLG, MTV, TMTV, Dmax
- Analyses de survie (courbes de Kaplan Meier + Cox) : OS, PFS

Résultats :

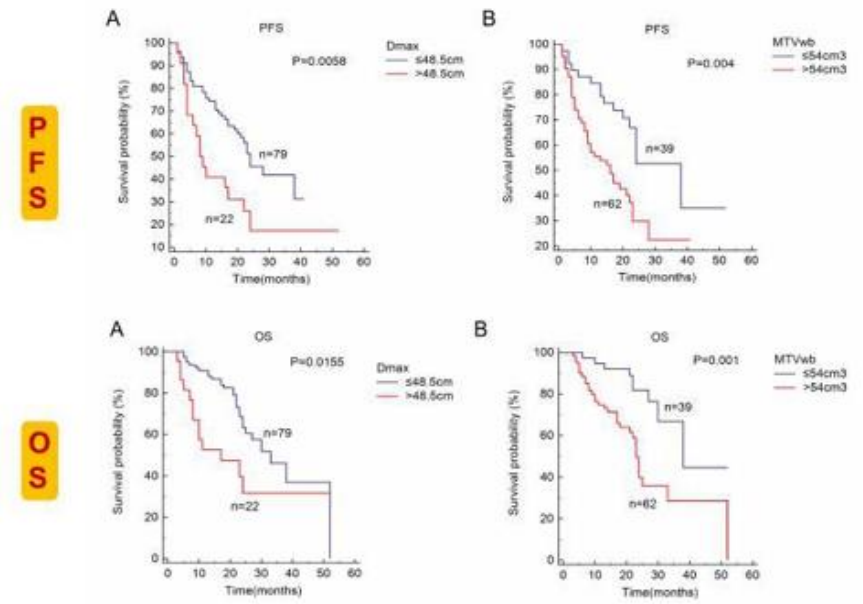

Figure 1 Kaplan–Meier analyses of PFS and OS according to D_{max} or MTV_{wb}

↘ OS et PFS lorsque TMTV > 53 cm³ et Dmax > 48.5 cm

June 24-27 2023 SNMMI ANNUAL MEETING CHICAGO Illinois, USA EYE ON THE PATIENT

FDG PET/CT tumor dissemination characteristic predicts the outcome of first-line systemic therapy in non-small cell lung cancer

Weiyue Tan[1,2], Yi Zhang[1,2], Jie Wang[1,2], Zhonghang Zheng[1,2], Ligang Xing[3] , Xiaorong Sun[2]
[1] Department of Graduate, Shandong First Medical University and Shandong Academy of Medical Sciences, Jinan, Shandong, China
[2] Department of Nuclear Medicine, Shandong Cancer Hospital and Institute, Shandong First Medical University and Shandong Academy of Medical Sciences, Jinan, Shandong, China
[3] Department of Radiation Oncology, Shandong Cancer Hospital and Institute, Shandong First Medical University and Shandong Academy of Medical Sciences, Jinan, Shandong, China

Objectif : étudier la corrélation entre les caractéristiques de la dissémination tumorale sur les images TEP/TDM au 18F-FDG et la réponse au traitement du cancer du poumon non à petites cellules (NSCLC) de stade IV.

Méthodes :

- 101 patients NSCLC:
  - Examen pré-thérapeutique TEP/TDM au 18F-FDG
  - Données cliniques : âge, sexe, statut tabagique, histologie (adénocarcinome, squameux, autres)
  - Données radiomiques (lésion primaire + métastases) : SUVmax, SUVmean, TLG, MTV, TMTV, Dmax
- Analyses de survie (courbes de Kaplan Meier + Cox) : OS, PFS

Résultats :

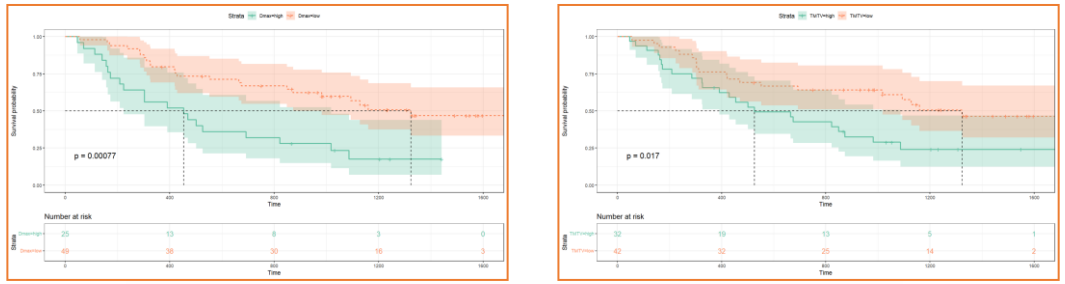

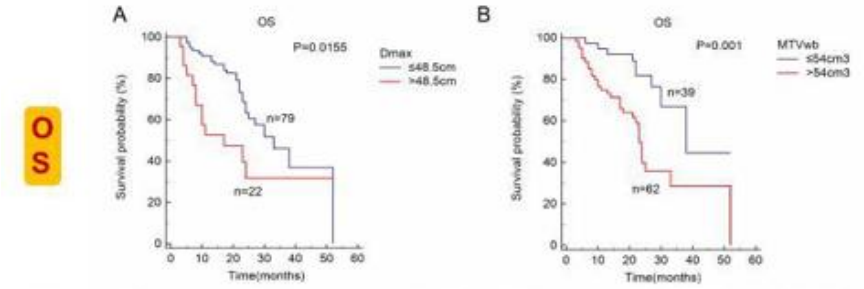

Figure 1 Kaplan–Meier analyses of PFS and OS according to D_{max} or MTV_{wb}

LITO (Capricorne)

↘ **OS lorsque TMTV > 90 cm³ et Dmax > 28.4 cm**

Résultats:

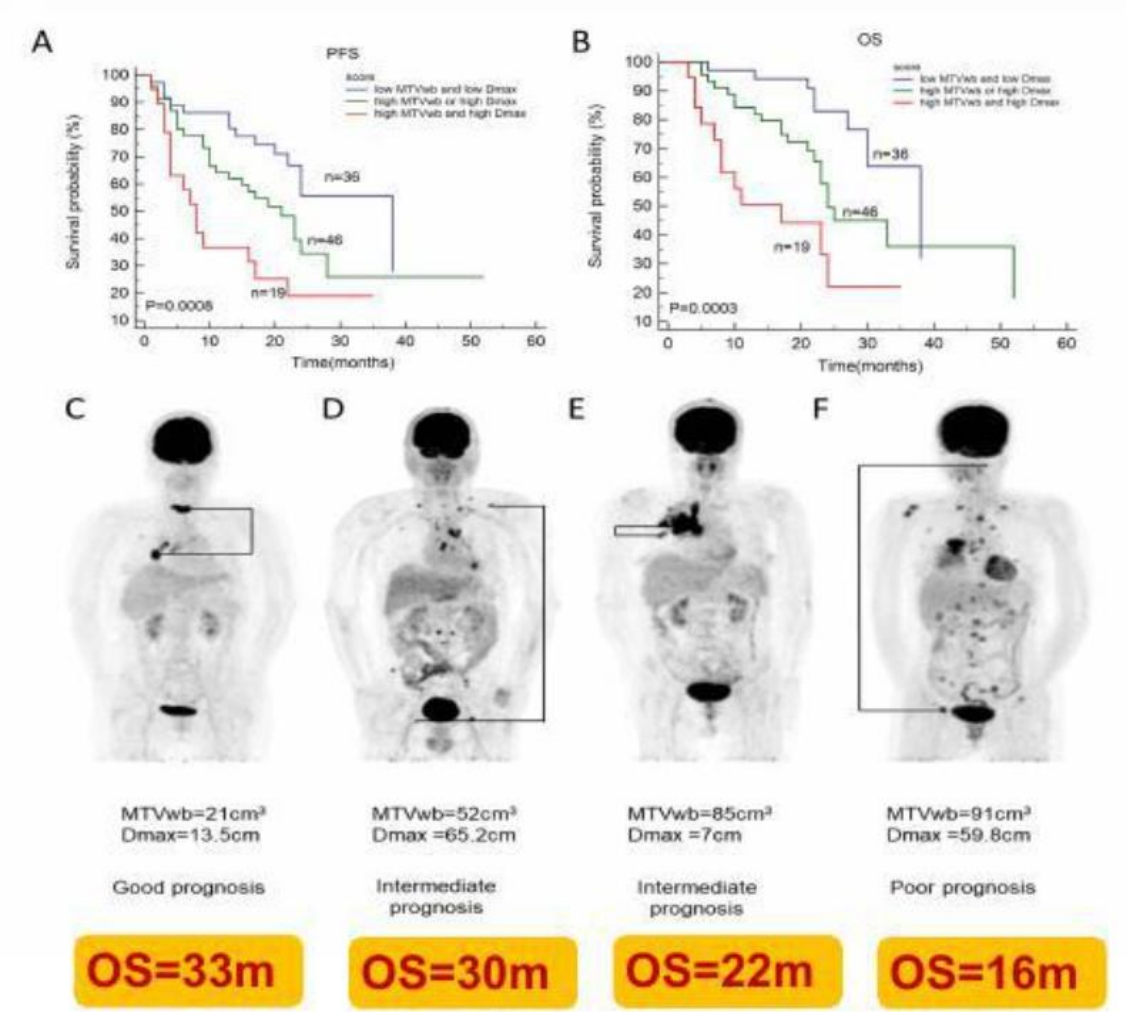

Figure 2 Kaplan–Meier analyses of PFS (A) and OS (B) according to the prognostic score constructed by D_{max} and MTV_{wb}.(C) A 73-year-old female (score 0) had an overall survival of 33 months. (D) A 59-year-old male (Score 1) had an overall survival of 30 months. (E) A 59-year-old female (Score 1) had an overall survival of 22 months. (F) A 51-year-old female (Score 2) had an overall survival of 16 months.

3 scores déterminés par facteurs de risque (0, 1 ou 2):

- **Score 0 (bon pronostic)** = TMTV ≤ 54cm^3 et Dmax ≤ 48.5cm
- **Score 1 (pronostic intermédiaire)** : TMTV > 54cm^3 ou Dmax > 48.5cm
- **Score 2 (mauvais pronostic)** : TMTV > 54cm^3 et Dmax > 48.5cm

Résultats:

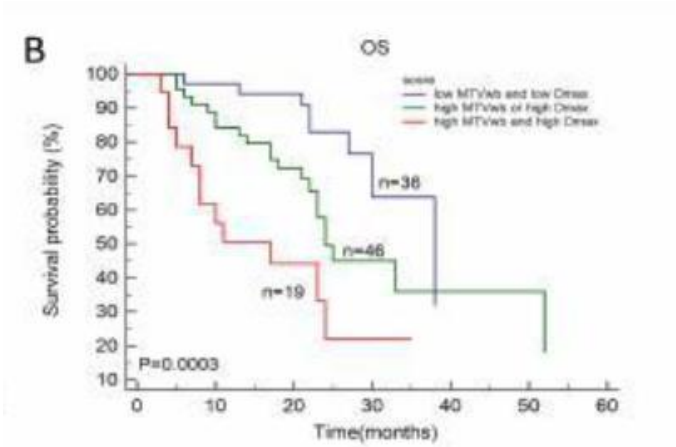

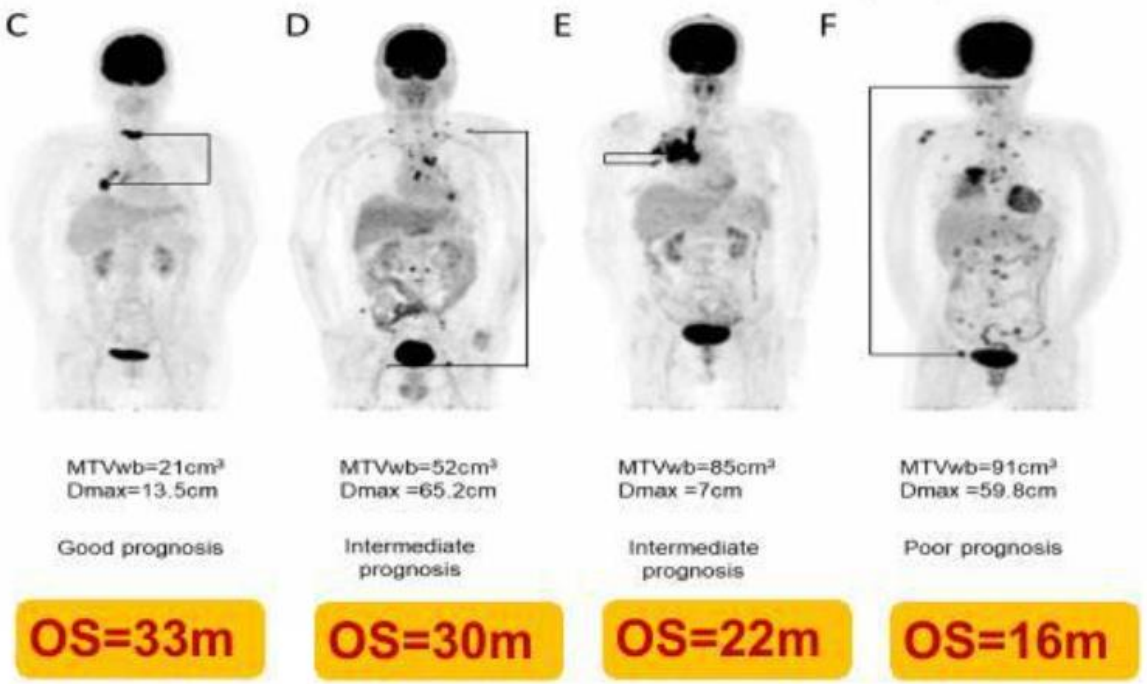

LITO (Capricorne)

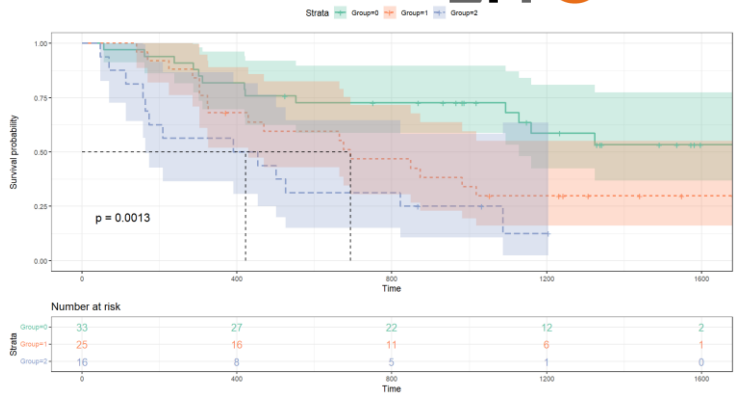

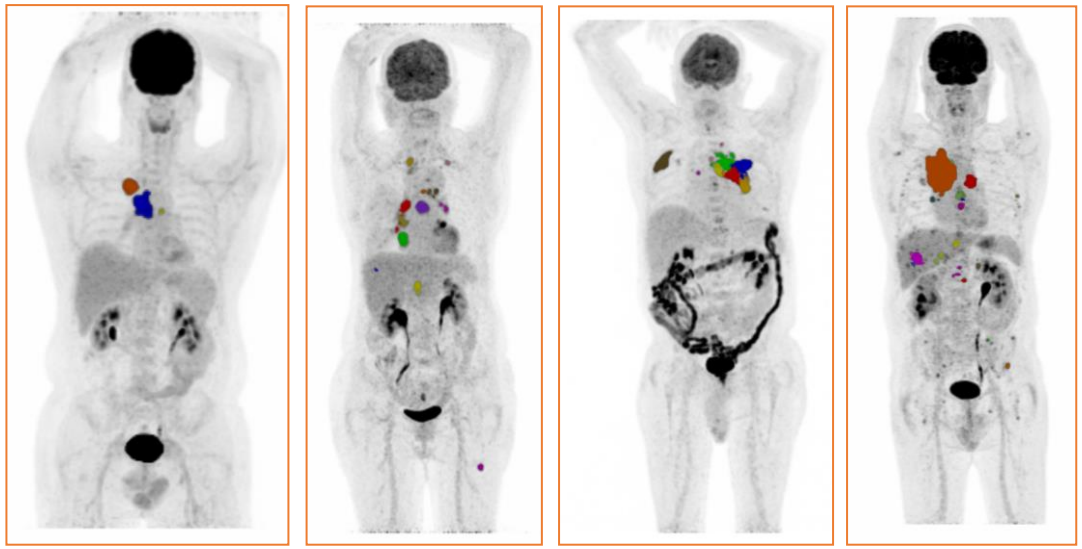

TMTV= 60cm³
Dmax=11.16cm
OS=51m

TMTV=35cm³
Dmax=67cm
OS=15m

TMTV=138cm³
Dmax=23.7cm
OS=22m

TMTV=307cm³
Dmax=57.9cm
OS=1m

Conclusion : la combinaison de la dissémination de la tumeur (Dmax) et de la charge tumorale (TMTV) permet d'améliorer la stratification du pronostic du NSCLC.

June 24-27 2023 SNMMI ANNUAL MEETING CHICAGO Illinois, USA EYE ON THE PATIENT

#2 Visceral adipose tissue glucose uptake can predict distant metastasis in non-small cell lung cancer

Qiannan Wang[1,2], Caozhe Cui[1,2], Xiaomeng Li[1,2], Doudou Lv[1,2], Yiyi Hu[1,2], Ning Ma[1,2], Weihua Yang[1,2], Zhifang Wu[1,2]*
[1]Department of Nuclear Medicine, the First Hospital of Shanxi Medical University;
[2]Collaborative Innovation Center for Molecular Imaging of Precision Medicine ,Shanxi Medical University , taiyuan , China

Objectif : déterminer la relation entre la fixation du glucose du tissu adipeux sur les images TEP/TDM au 18F-FDG et la survenue de métastases à distance dans le cancer du poumon non à petites cellules (NSCLC).

Méthodes :

- 59 patients NSCLC divisés selon la présence de métastases (24 M0/ 43 M1):
  - Examen pré-thérapeutique TEP/TDM au 18F-FDG
  - Données cliniques : histologie (adénocarcinome, squameux), Ki67, BMI
  - Données radiomiques (3D slicer) : SUVmax, SUVmean, SUVpeak, TLG, MTV, SUVmax_VAT/SAT, SUVmean VAT/SAT, VAT SUVmax/SAT SUVmax (V/S ratio), Volume VAT, Volume SAT.

Résultats :

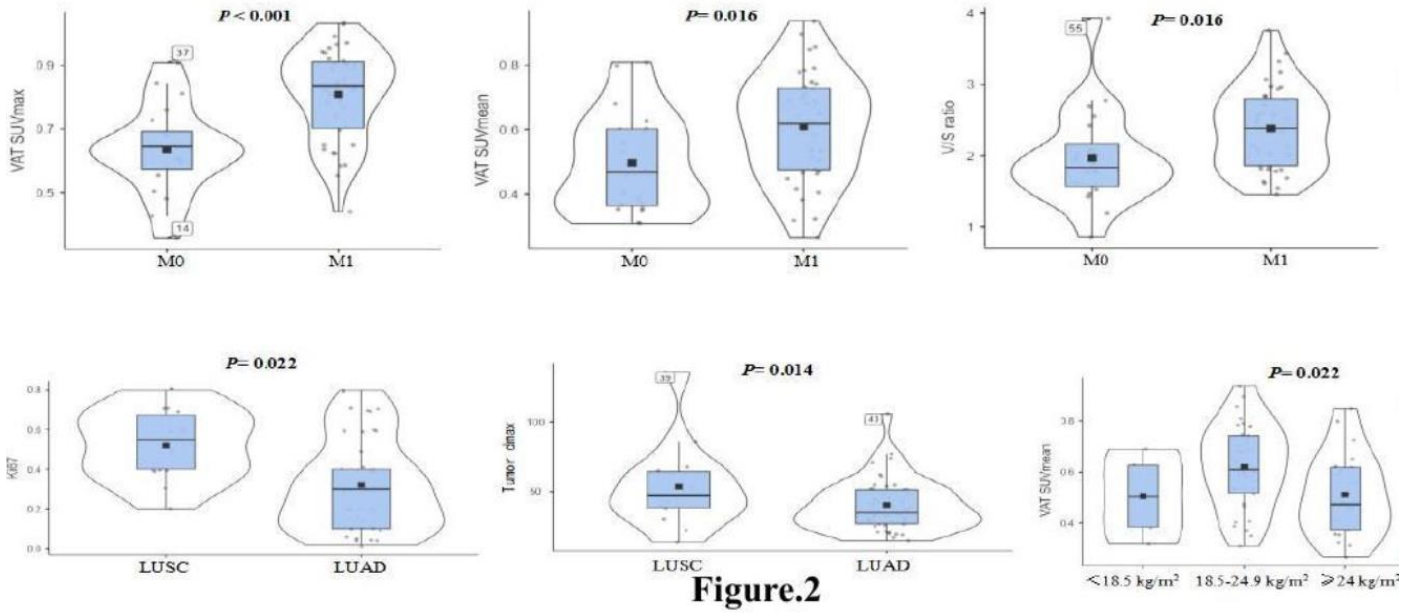

Figure.2

- ↗ VAT SUVmax, VAT SUVmean et V/S ratio chez les patients M1
- ≠ significatives du VAT SUVmean entre les patients en surpoids/obèses (IMC > 24 kg/m²) et les patients avec un IMC normal (18.5-24.9 kg/m²) (p= 0.022)

Résultats :

LITO (Capricorne)

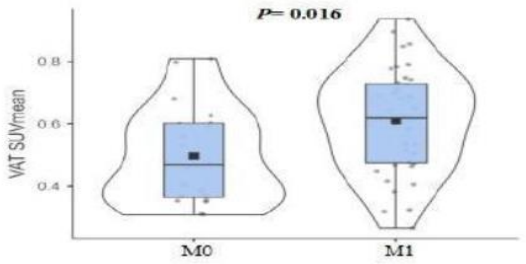

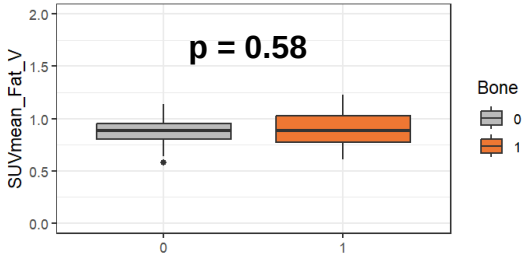

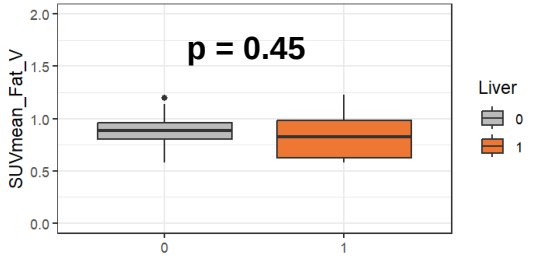

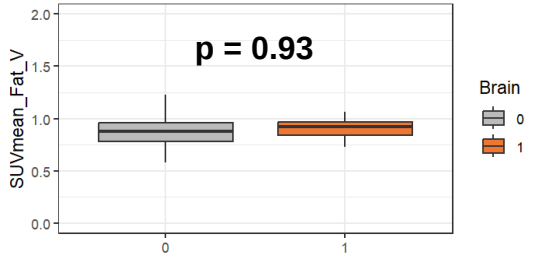

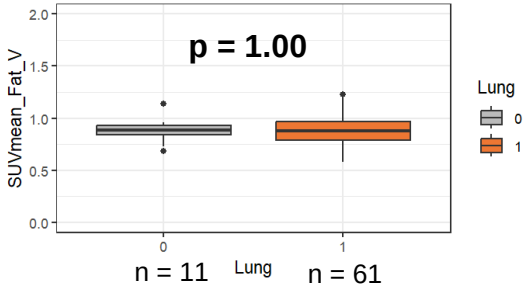

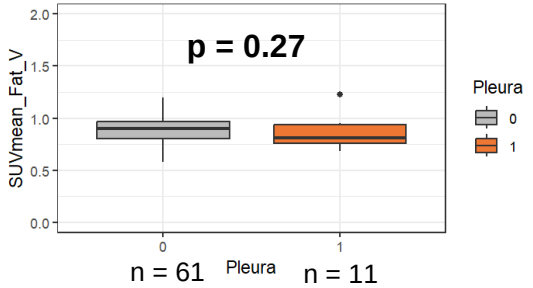

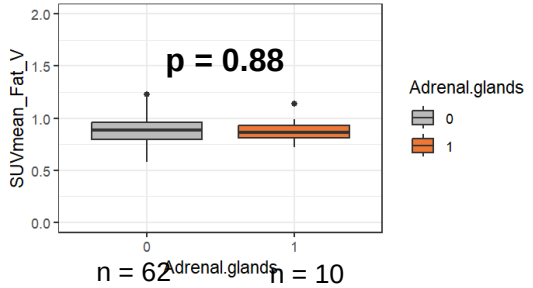

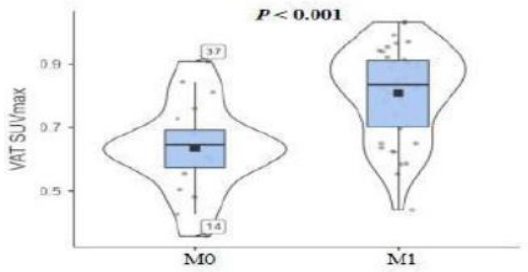

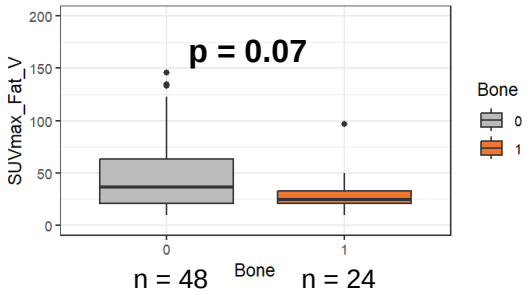

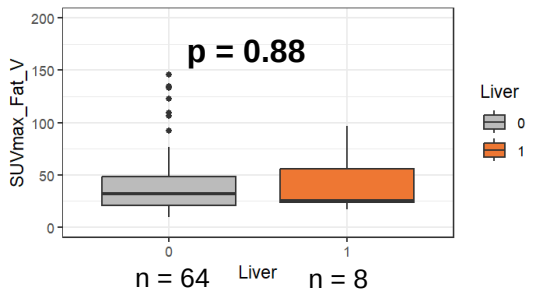

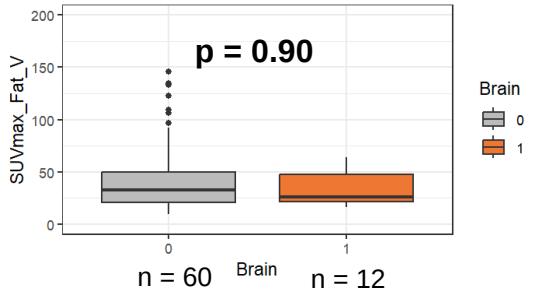

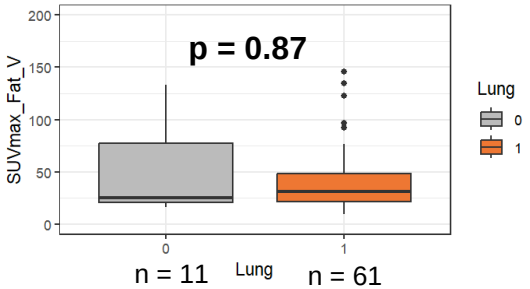

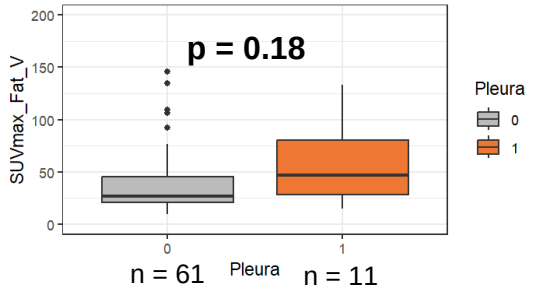

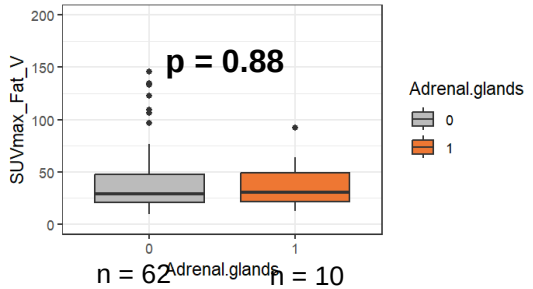

LITO (Capricorne)

Résultats :

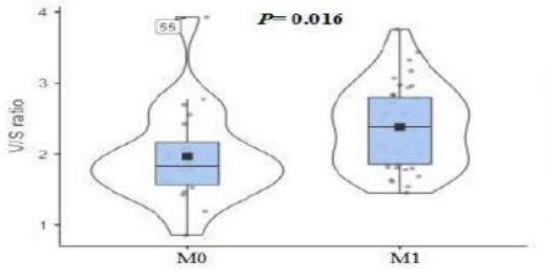

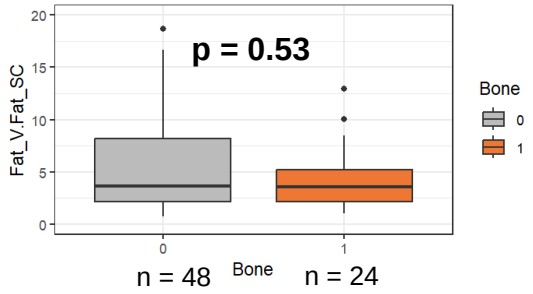

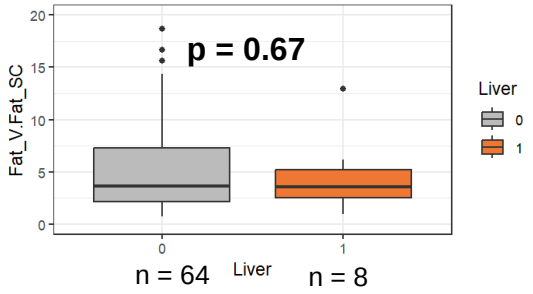

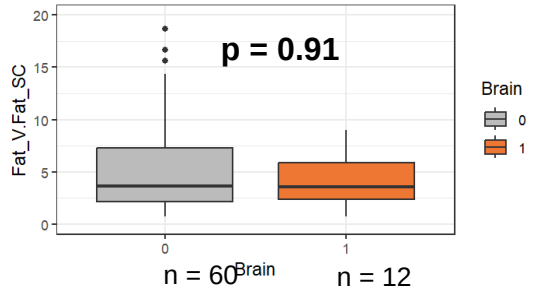

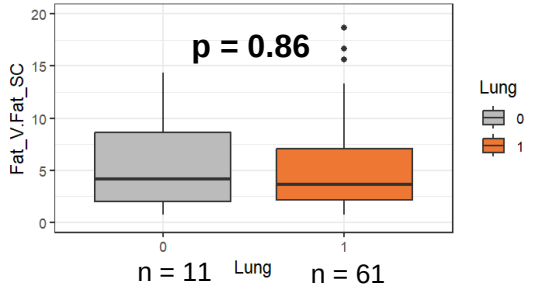

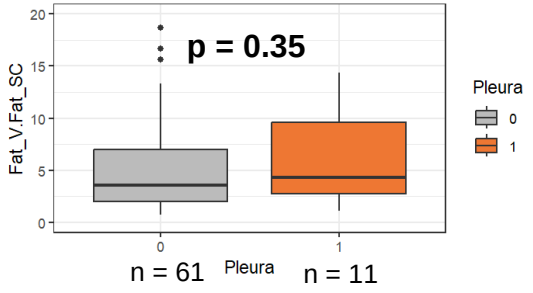

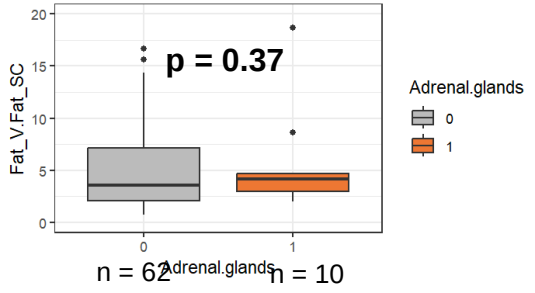

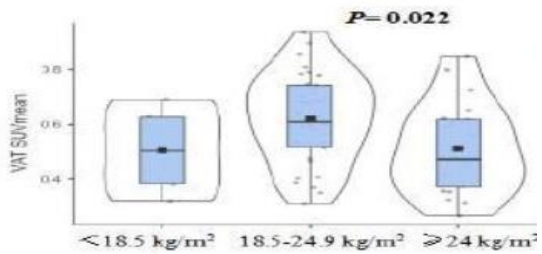

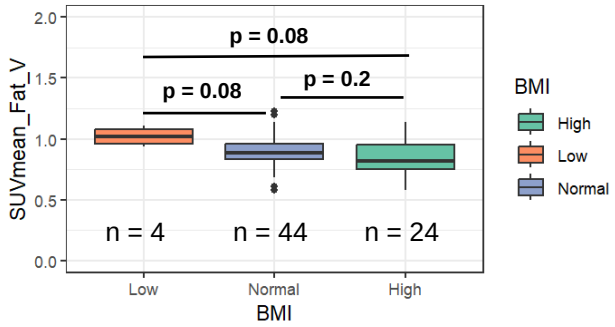

Conclusion :

- Les patients ayant des métastases présentent un SUV VAT et un ratio VAT/SAT plus élevé que les patients non métastatiques.
- La fixation du glucose de la graisse viscérale peut servir de biomarqueur potentiel de l'agressivité de la tumeur et prédire la survenue de métastases à distance chez les patients NSCLC.

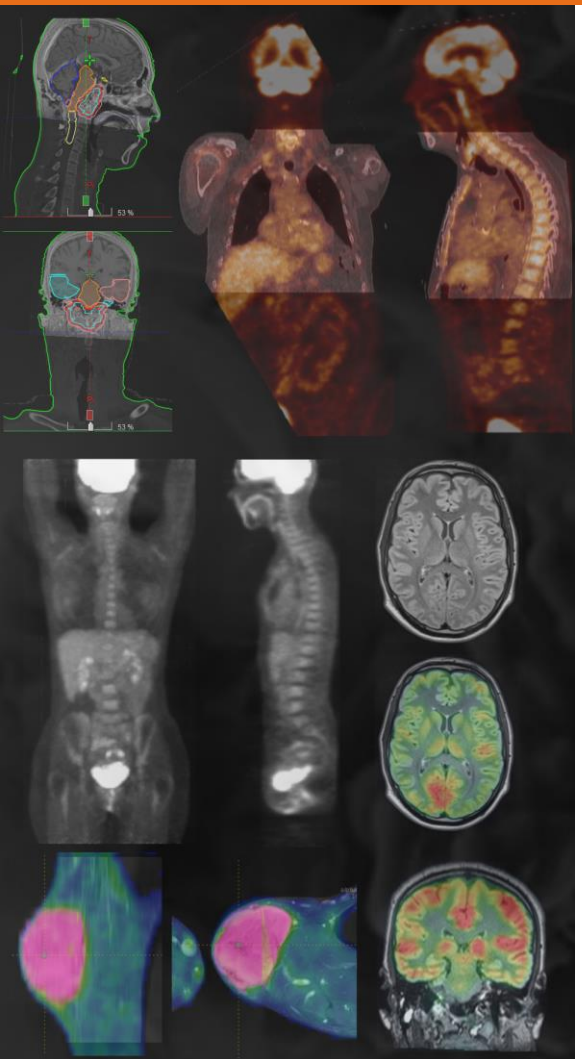

Retour congrès SNMMI - Chicago

Fanny – 6 juillet 2023

Improvement of Gleason Grading Prediction in Prostate Cancer Stratification for Radical Prostatectomy: a Machine Learning- based Theranostic Multi-omics Study

Jing Ning*[1,2,3], Clemens Spielvogel*[1,3], David Haberl [1,3], Karolina Tractova [1,4], Stefan Stoiber [1,2], Sazan Rasul [3], Vojtech Bystry [4], Elisabeth Gurnhofer [2], Gerald Timelthaler [5], Laszlo Papp [3], Michaela Schlederer [2], Marcus Hacker [3], Alexander Haug [1,3], Lukas Kenner[1,2,6]

[1] Christian Doppler Laboratory for Applied Metabolomics, 1090 Vienna, Austria. [2] Division of Experimental and Translational Pathology, Department of Pathology, Medical University of Vienna, 1090 Vienna, Austria. [3] Division of Nuclear Medicine, Department of Biomedical Imaging and Image-Guided Therapy, Medical University of Vienna, 1090 Vienna, Austria. [4] Central European Institute of Technology, Masaryk University, Brno 62500, Czech Republic. [5] Unit of Laboratory Animal Pathology, University of Veterinary Medicine Vienna, 1210 Vienna, Austria. [6] Christian Doppler Laboratory for Applied Metabolomics, 1090 Vienna, Austria. [7] Christian Doppler Laboratory for Applied Metabolomics, 1090 Vienna, Austria. [8] Christian Doppler Laboratory for Applied Metabolomics, 1090 Vienna, Austria. [9] Christian Doppler Laboratory for Applied Metabolomics, 1090 Vienna, Austria. [10] Christian Doppler Laboratory for Applied Metabolomics, 1090 Vienna, Austria. [11] Christian Doppler Laboratory for Applied Metabolomics, 1090 Vienna, Austria. [12] Christian Doppler Laboratory for Applied Metabolomics, 1090 Vienna, Austria. [13] Christian Doppler Laboratory for Applied Metabolomics, 1090 Vienna, Austria. [14] Christian Doppler Laboratory for Applied Metabolomics, 1090 Vienna, Austria. [15] Christian Doppler Laboratory for Applied Metabolomics, 1090 Vienna, Austria. [16] Christian Doppler Laboratory for Applied Metabolomics, 1090 Vienna, Austria. [17] Christian Doppler Laboratory for Applied Metabolomics, 1090 Vienna, Austria. [18] Christian Doppler Laboratory for Applied Metabolomics, 1090 Vienna, Austria. [19] Christian Doppler Laboratory for Applied Metabolomics, 1090 Vienna, Austria. [20] Christian Doppler Laboratory for Applied Metabolomics, 1090 Vienna, Austria. [21] Christian Doppler Laboratory for Applied Metabolomics, 1090 Vienna, Austria. [22] Christian Doppler Laboratory for Applied Metabolomics, 1090 Vienna, Austria. [23] Christian Doppler Laboratory for Applied Metabolomics, 1090 Vienna, Austria. [24] Christian Doppler Laboratory for Applied Metabolomics, 1090 Vienna, Austria. [25] Christian Doppler Laboratory for Applied Metabolomics, 1090 Vienna, Austria. [26] Christian Doppler Laboratory for Applied Metabolomics, 1090 Vienna, Austria. [27] Christian Doppler Laboratory for Applied Metabolomics, 1090 Vienna, Austria. [28] Christian Doppler Laboratory for Applied Metabolomics, 1090 Vienna, Austria. [29] Christian Doppler Laboratory for Applied Metabolomics, 1090 Vienna, Austria. [30] Christian Doppler Laboratory for Applied Metabolomics, 1090 Vienna, Austria. [31] Christian Doppler Laboratory for Applied Metabolomics, 1090 Vienna, Austria. [32] Christian Doppler Laboratory for Applied Metabolomics, 1090 Vienna, Austria. [33] Christian Doppler Laboratory for Applied Metabolomics, 1090 Vienna, Austria. [34] Christian Doppler Laboratory for Applied Metabolomics, 1090 Vienna, Austria. [35] Christian Doppler Laboratory for Applied Metabolomics, 1090 Vienna, Austria. [36] Christian Doppler Laboratory for Applied Metabolomics, 1090 Vienna, Austria. [37] Christian Doppler Laboratory for Applied Metabolomics, 1090 Vienna, Austria. [38] Christian Doppler Laboratory for Applied Metabolomics, 1090 Vienna, Austria. [39] Christian Doppler Laboratory for Applied Metabolomics, 1090 Vienna, Austria. [40] Christian Doppler Laboratory for Applied Metabolomics, 1090 Vienna, Austria. [41] Christian Doppler Laboratory for Applied Metabolomics, 1090 Vienna, Austria. [42] Christian Doppler Laboratory for Applied Metabolomics, 1090 Vienna, Austria. [43] Christian Doppler Laboratory for Applied Metabolomics, 1090 Vienna, Austria. [44] Christian Doppler Laboratory for Applied Metabolomics, 1090 Vienna, Austria. [45] Christian Doppler Laboratory for Applied Metabolomics, 1090 Vienna, Austria. [46] Christian Doppler Laboratory for Applied Metabolomics, 1090 Vienna, Austria. [47] Christian Doppler Laboratory for Applied Metabolomics, 1090 Vienna, Austria. [48] Christian Doppler Laboratory for Applied Metabolomics, 1090 Vienna, Austria. [49] Christian Doppler Laboratory for Applied Metabolomics, 1090 Vienna, Austria. [50] Christian Doppler Laboratory for Applied Metabolomics, 1090 Vienna, Austria. [51] Christian Doppler Laboratory for Applied Metabolomics, 1090 Vienna, Austria. [52] Christian Doppler Laboratory for Applied Metabolomics, 1090 Vienna, Austria. [53] Christian Doppler Laboratory for Applied Metabolomics, 1090 Vienna, Austria. [54] Christian Doppler Laboratory for Applied Metabolomics, 1090 Vienna, Austria. [55] Christian Doppler Laboratory for Applied Metabolomics, 1090 Vienna, Austria. [56] Christian Doppler Laboratory for Applied Metabolomics, 1090 Vienna, Austria. [57] Christian Doppler Laboratory for Applied Metabolomics, 1090 Vienna, Austria. [58] Christian Doppler Laboratory for Applied Metabolomics, 1090 Vienna, Austria. [59] Christian Doppler Laboratory for Applied Metabolomics, 1090 Vienna, Austria. [60] Christian Doppler Laboratory for Applied Metabolomics, 1090 Vienna, Austria. [61] Christian Doppler Laboratory for Applied Metabolomics, 1090 Vienna, Austria. [62] Christian Doppler Laboratory for Applied Metabolomics, 1090 Vienna, Austria. [63] Christian Doppler Laboratory for Applied Metabolomics, 1090 Vienna, Austria. [64] Christian Doppler Laboratory for Applied Metabolomics, 1090 Vienna, Austria. [65] Christian Doppler Laboratory for Applied Metabolomics, 1090 Vienna, Austria. [66] Christian Doppler Laboratory for Applied Metabolomics, 1090 Vienna, Austria. [67] Christian Doppler Laboratory for Applied Metabolomics, 1090 Vienna, Austria. [68] Christian Doppler Laboratory for Applied Metabolomics, 1090 Vienna, Austria. [69] Christian Doppler Laboratory for Applied Metabolomics, 1090 Vienna, Austria. [70] Christian Doppler Laboratory for Applied Metabolomics, 1090 Vienna, Austria. [71] Christian Doppler Laboratory for Applied Metabolomics, 1090 Vienna, Austria. [72] Christian Doppler Laboratory for Applied Metabolomics, 1090 Vienna, Austria. [73] Christian Doppler Laboratory for Applied Metabolomics, 1090 Vienna, Austria. [74] Christian Doppler Laboratory for Applied Metabolomics, 1090 Vienna, Austria. [75] Christian Doppler Laboratory for Applied Metabolomics, 1090 Vienna, Austria. [76] Christian Doppler Laboratory for Applied Metabolomics, 1090 Vienna, Austria. [77] Christian Doppler Laboratory for Applied Metabolomics, 1090 Vienna, Austria. [78] Christian Doppler Laboratory for Applied Metabolomics, 1090 Vienna, Austria. [79] Christian Doppler Laboratory for Applied Metabolomics, 1090 Vienna, Austria. [80] Christian Doppler Laboratory for Applied Metabolomics, 1090 Vienna, Austria. [81] Christian Doppler Laboratory for Applied Metabolomics, 1090 Vienna, Austria. [82] Christian Doppler Laboratory for Applied Metabolomics, 1090 Vienna, Austria. [83] Christian Doppler Laboratory for Applied Metabolomics, 1090 Vienna, Austria. [84] Christian Doppler Laboratory for Applied Metabolomics, 1090 Vienna, Austria. [85] Christian Doppler Laboratory for Applied Metabolomics, 1090 Vienna, Austria. [86] Christian Doppler Laboratory for Applied Metabolomics, 1090 Vienna, Austria. [87] Christian Doppler Laboratory for Applied Metabolomics, 1090 Vienna, Austria. [88] Christian Doppler Laboratory for Applied Metabolomics, 1090 Vienna, Austria. [89] Christian Doppler Laboratory for Applied Metabolomics, 1090 Vienna, Austria. [90] Christian Doppler Laboratory for Applied Metabolomics, 1090 Vienna, Austria. [91] Christian Doppler Laboratory for Applied Metabolomics, 1090 Vienna, Austria. [92] Christian Doppler Laboratory for Applied Metabolomics, 1090 Vienna, Austria. [93] Christian Doppler Laboratory for Applied Metabolomics, 1090 Vienna, Austria. [94] Christian Doppler Laboratory for Applied Metabolomics, 1090 Vienna, Austria. [95] Christian Doppler Laboratory for Applied Metabolomics, 1090 Vienna, Austria. [96] Christian Doppler Laboratory for Applied Metabolomics, 1090 Vienna, Austria. [97] Christian Doppler Laboratory for Applied Metabolomics, 1090 Vienna, Austria. [98] Christian Doppler Laboratory for Applied Metabolomics, 1090 Vienna, Austria. [99] Christian Doppler Laboratory for Applied Metabolomics, 1090 Vienna, Austria. [100] Christian Doppler Laboratory for Applied Metabolomics, 1090 Vienna, Austria. [101] Christian Doppler Laboratory for Applied Metabolomics, 1090 Vienna, Austria. [102] Christian Doppler Laboratory for Applied Metabolomics, 1090 Vienna, Austria. [103] Christian Doppler Laboratory for Applied Metabolomics, 1090 Vienna, Austria. [104] Christian Doppler Laboratory for Applied Metabolomics, 1090 Vienna, Austria. [105] Christian Doppler Laboratory for Applied Metabolomics, 1090 Vienna, Austria. [106] Christian Doppler Laboratory for Applied Metabolomics, 1090 Vienna, Austria. [107] Christian Doppler Laboratory for Applied Metabolomics, 1090 Vienna, Austria. [108] Christian Doppler Laboratory for Applied Metabolomics, 1090 Vienna, Austria. [109] Christian Doppler Laboratory for Applied Metabolomics, 1090 Vienna, Austria. [110] Christian Doppler Laboratory for Applied Metabolomics, 1090 Vienna, Austria. [111] Christian Doppler Laboratory for Applied Metabolomics, 1090 Vienna, Austria. [112] Christian Doppler Laboratory for Applied Metabolomics, 1090 Vienna, Austria. [113] Christian Doppler Laboratory for Applied Metabolomics, 1090 Vienna, Austria. [114] Christian Doppler Laboratory for Applied Metabolomics, 1090 Vienna, Austria. [115] Christian Doppler Laboratory for Applied Metabolomics, 1090 Vienna, Austria. [116] Christian Doppler Laboratory for Applied Metabolomics, 1090 Vienna, Austria. [117] Christian Doppler Laboratory for Applied Metabolomics, 1090 Vienna, Austria. [118] Christian Doppler Laboratory for Applied Metabolomics, 1090 Vienna, Austria. [119] Christian Doppler Laboratory for Applied Metabolomics, 1090 Vienna, Austria. [120] Christian Doppler Laboratory for Applied Metabolomics, 1090 Vienna, Austria. [121] Christian Doppler Laboratory for Applied Metabolomics, 1090 Vienna, Austria. [122] Christian Doppler Laboratory for Applied Metabolomics, 1090 Vienna, Austria. [123] Christian Doppler Laboratory for Applied Metabolomics, 1090 Vienna, Austria. [124] Christian Doppler Laboratory for Applied Metabolomics, 1090 Vienna, Austria. [125] Christian Doppler Laboratory for Applied Metabolomics, 1090 Vienna, Austria. [126] Christian Doppler Laboratory for Applied Metabolomics, 1090 Vienna, Austria. [127] Christian Doppler Laboratory for Applied Metabolomics, 1090 Vienna, Austria. [128] Christian Doppler Laboratory for Applied Metabolomics, 1090 Vienna, Austria. [129] Christian Doppler Laboratory for Applied Metabolomics, 1090 Vienna, Austria. [130] Christian Doppler Laboratory for Applied Metabolomics, 1090 Vienna, Austria. [131] Christian Doppler Laboratory for Applied Metabolomics, 1090 Vienna, Austria. [132] Christian Doppler Laboratory for Applied Metabolomics, 1090 Vienna, Austria. [133] Christian Doppler Laboratory for Applied Metabolomics, 1090 Vienna, Austria. [134] Christian Doppler Laboratory for Applied Metabolomics, 1090 Vienna, Austria. [135] Christian Doppler Laboratory for Applied Metabolomics, 1090 Vienna, Austria. [136] Christian Doppler Laboratory for Applied Metabolomics, 1090 Vienna, Austria. [137] Christian Doppler Laboratory for Applied Metabolomics, 1090 Vienna, Austria. [138] Christian Doppler Laboratory for Applied Metabolomics, 1090 Vienna, Austria. [139] Christian Doppler Laboratory for Applied Metabolomics, 1090 Vienna, Austria. [140] Christian Doppler Laboratory for Applied Metabolomics, 1090 Vienna, Austria. [141] Christian Doppler Laboratory for Applied Metabolomics, 1090 Vienna, Austria. [142] Christian Doppler Laboratory for Applied Metabolomics, 1090 Vienna, Austria. [143] Christian Doppler Laboratory for Applied Metabolomics, 1090 Vienna, Austria. [144] Christian Doppler Laboratory for Applied Metabolomics, 1090 Vienna, Austria. [145] Christian Doppler Laboratory for Applied Metabolomics, 1090 Vienna, Austria. [146] Christian Doppler Laboratory for Applied Metabolomics, 1090 Vienna, Austria. [147] Christian Doppler Laboratory for Applied Metabolomics, 1090 Vienna, Austria. [148] Christian Doppler Laboratory for Applied Metabolomics, 1090 Vienna, Austria. [149] Christian Doppler Laboratory for Applied Metabolomics, 1090 Vienna, Austria. [150] Christian Doppler Laboratory for Applied Metabolomics, 1090 Vienna, Austria. [151] Christian Doppler Laboratory for Applied Metabolomics, 1090 Vienna, Austria. [152] Christian Doppler Laboratory for Applied Metabolomics, 1090 Vienna, Austria. [153] Christian Doppler Laboratory for Applied Metabolomics, 1090 Vienna, Austria. [154] Christian Doppler Laboratory for Applied Metabolomics, 1090 Vienna, Austria. [155] Christian Doppler Laboratory for Applied Metabolomics, 1090 Vienna, Austria. [156] Christian Doppler Laboratory for Applied Metabolomics, 1090 Vienna, Austria. [157] Christian Doppler Laboratory for Applied Metabolomics, 1090 Vienna, Austria. [158] Christian Doppler Laboratory for Applied Metabolomics, 1090 Vienna, Austria. [159] Christian Doppler Laboratory for Applied Metabolomics, 1090 Vienna, Austria. [160] Christian Doppler Laboratory for Applied Metabolomics, 1090 Vienna, Austria. [161] Christian Doppler Laboratory for Applied Metabolomics, 1090 Vienna, Austria. [162] Christian Doppler Laboratory for Applied Metabolomics, 1090 Vienna, Austria. [163] Christian Doppler Laboratory for Applied Metabolomics, 1090 Vienna, Austria. [164] Christian Doppler Laboratory for Applied Metabolomics, 1090 Vienna, Austria. [165] Christian Doppler Laboratory for Applied Metabolomics, 1090 Vienna, Austria. [166] Christian Doppler Laboratory for Applied Metabolomics, 1090 Vienna, Austria. [167] Christian Doppler Laboratory for Applied Metabolomics, 1090 Vienna, Austria. [168] Christian Doppler Laboratory for Applied Metabolomics, 1090 Vienna, Austria. [169] Christian Doppler Laboratory for Applied Metabolomics, 1090 Vienna, Austria. [170] Christian Doppler Laboratory for Applied Metabolomics, 1090 Vienna, Austria. [171] Christian Doppler Laboratory for Applied Metabolomics, 1090 Vienna, Austria. [172] Christian Doppler Laboratory for Applied Metabolomics, 1090 Vienna, Austria. [173] Christian Doppler Laboratory for Applied Metabolomics, 1090 Vienna, Austria. [174] Christian Doppler Laboratory for Applied Metabolomics, 1090 Vienna, Austria. [175] Christian Doppler Laboratory for Applied Metabolomics, 1090 Vienna, Austria. [176] Christian Doppler Laboratory for Applied Metabolomics, 1090 Vienna, Austria. [177] Christian Doppler Laboratory for Applied Metabolomics, 1090 Vienna, Austria. [178] Christian Doppler Laboratory for Applied Metabolomics, 1090 Vienna, Austria. [179] Christian Doppler Laboratory for Applied Metabolomics, 1090 Vienna, Austria. [180] Christian Doppler Laboratory for Applied Metabolomics, 1090 Vienna, Austria. [181] Christian Doppler Laboratory for Applied Metabolomics, 1090 Vienna, Austria. [182] Christian Doppler Laboratory for Applied Metabolomics, 1090 Vienna, Austria. [183] Christian Doppler Laboratory for Applied Metabolomics, 1090 Vienna, Austria. [184] Christian Doppler Laboratory for Applied Metabolomics, 1090 Vienna, Austria. [185] Christian Doppler Laboratory for Applied Metabolomics, 1090 Vienna, Austria. [186] Christian Doppler Laboratory for Applied Metabolomics, 1090 Vienna, Austria. [187] Christian Doppler Laboratory for Applied Metabolomics, 1090 Vienna, Austria. [188] Christian Doppler Laboratory for Applied Metabolomics, 1090 Vienna, Austria. [189] Christian Doppler Laboratory for Applied Metabolomics, 1090 Vienna, Austria. [190] Christian Doppler Laboratory for Applied Metabolomics, 1090 Vienna, Austria. [191] Christian Doppler Laboratory for Applied Metabolomics, 1090 Vienna, Austria. [192] Christian Doppler Laboratory for Applied Metabolomics, 1090 Vienna, Austria. [193] Christian Doppler Laboratory for Applied Metabolomics, 1090 Vienna, Austria. [194] Christian Doppler Laboratory for Applied Metabolomics, 1090 Vienna, Austria. [195] Christian Doppler Laboratory for Applied Metabolomics, 1090 Vienna, Austria. [196] Christian Doppler Laboratory for Applied Metabolomics, 1090 Vienna, Austria. [197] Christian Doppler Laboratory for Applied Metabolomics, 1090 Vienna, Austria. [198] Christian Doppler Laboratory for Applied Metabolomics, 1090 Vienna, Austria. [199] Christian Doppler Laboratory for Applied Metabolomics, 1090 Vienna, Austria. [200] Christian Doppler Laboratory for Applied Metabolomics, 1090 Vienna, Austria.

Background & Aim

Gleason Score (GS) in needle biopsy is the main determining factor for the decision of radical prostatectomy (RP). However, it brings various challenges to patients' quality of life, such as post-procedure infections and the multiple invasiveness. A promising standardized workflow is in urgent need to be well established for the aid of precise clinical decisions.

In this study, we aim to **predict the whole mount Gleason grading in prostate cancer for smart and precise patient stratification for radical prostatectomy using a high-throughput machine learning (ML) model and compare its predictive performance with that of needle biopsy.**

Results

01 Genomics

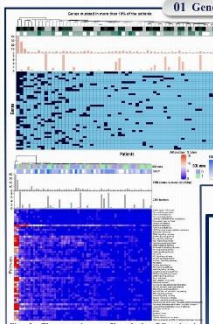

Fig. 1. Genes' mutation profile of the primary prostate cancer cohort with prognostic genomic biomarkers (CNV burden*, TMB*) and clinical markers (BCR* status and ISUP*). The figure profiled the genes with the frequency of more than 10% in the cohort but the distribution of genes mutations status is sparse. There is no clear associated pattern between the gene mutation profile and the clinical prognostic markers; For genomic markers, the gene mutation profile is consistent with TMB.

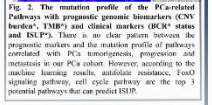

Fig. 2. The mutation profile of the PCa-related Pathways with prognostic genomic biomarkers (CNV burden*, TMB*) and clinical markers (BCR* status and ISUP*). There is no clear pattern between the prognostic markers and the mutation profile of pathways correlated with PCa tumorigenesis, progression and metastasis in our PCa cohort. However, according to the machine learning results, antifolate resistance, FoxO signaling pathway, cell cycle pathway are the top 3 potential pathways that can predict ISUP.

02 Pathomics

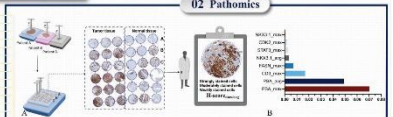

Fig. 3. The workflow of pathomics and important pathomic features derived from ML model to predict ISUP grading. (A) Derived from FFPE samples, we constructed the tumor microarray and stained them with potential prognostic biomarkers. Then pathologists assessed the IHC staining and gave the strongly/ moderately/ weakly stained cells, where H-score was calculated; **(B).** This bar plot showed PSA, CD3, FASN, NKX3.1, STAT3, CDK2 are the most contributing biomarkers to predict Gleason grading. Additionally, it showed the maximum value of the expression score performed better than average value of that.

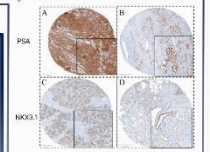

Fig. 4. Representative images of TMA cores stained with PSA and NKX3.1. A. TMA core and the details of tumor tissue with PSA high expression; **B.** TMA core and the details of tumor tissue with PSA low expression; **C.** TMA core and the details of tumor tissue with NKX3.1 high expression; **D.** TMA core and the details of tumor tissue with NKX3.1 low expression.

Methods & Materials

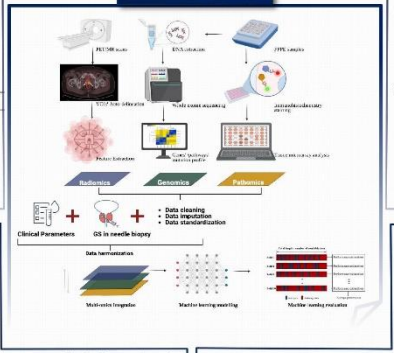

03 Radiomics

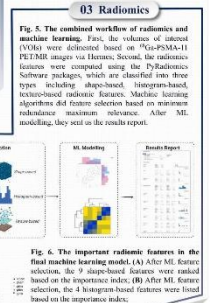

Fig. 5. The combined workflow of radiomics and machine learning. First, the volumes of interest (VOIs) were delineated based on ^{68}Ga-PSMA-11 PET/MR images via Hermes; Second, the radiomics features were computed using the PyRadiomics Software packages, which are classified into three types including shape-based, histogram-based, texture-based radiomic features. Machine learning algorithms did feature selection based on minimum redundance maximum relevance. After ML modelling, they sent us the results report.

Fig. 6. The important radiomic features in the final machine learning model. (A) After ML feature selection, the 9 shape-based features were ranked based on the importance index; **(B)** After ML feature selection, the 4 histogram-based features were listed based on the importance index;

04 Machine Learning

Fig. 7. The performance of different ML models to predict ISUP. Taking all the parameters together, RF* method has the best performance, whose ACC, SNS, SPC, PPV, NPV and AUC are 0.78, 0.83, 0.72, 0.79, 0.80 and 0.87 respectively.

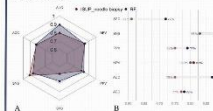

Fig. 8. The comparison of predictive performance between needle biopsy and RF. A. The radar chart showed the overall performance of RF is better than that of needle biopsy; **B.** The lollipop plot showed compared to needle biopsy, the SPC, PPV, ACC and AUC of RF to predict Gleason grading were elevated by 18% (0.81 vs 0.72), 7% (0.75 vs 0.79),1% (0.77 vs 0.78) and 11% (0.75 vs 0.87) respectively while the SNS and NPV were decreased by 7% (0.89 vs 0.83) and 1% (0.81 vs 0.80).

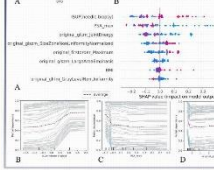

Fig. 9. The most 8 important features in the RF model to predict Gleason grading of PCa. A. The SHAP value plot showed the most important 8 features and the correlation of these 8 features with ISUP. **B.D.** The partial importance plots of the top 3 features confirmed the relationship between the feature value with ISUP value.

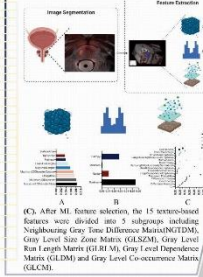

(C). After ML feature selection, the 15 texture-based features were divided into 5 subgroups including Neighbouring Gray Tone Difference Matrix(NGTDM), Gray Level Size Zone Matrix (GLSZM), Gray Level Run Length Matrix (GLRLM), Gray Level Dependence Matrix (GLDM) and Gray Level Co-occurrence Matrix (GLCM).

Conclusion

Our findings demonstrate that our multiomics-based machine learning model has the better performance for the prediction of Gleason grading than the current clinical baseline, which potentially facilitates the clinical decision-making and personalized management of prostate cancer.

PCa: prostate cancer; ML: machine learning; GS: Gleason score; ISUP: International Society of Urological Pathology; CNV: copy number variant; TMB: tumor mutational burden; BCR: biochemical recurrence; AUC: area under the curve; SNS: sensitivity; SPC: specificity; ACC: accuracy; PPV: positive predictive value; NPV: negative predictive value; KNN: K-nearest neighbors; RF: random forest; SVM: support vector machine; RGB: information pairwise; XGB: extreme gradient boosting; PSA: prostate-specific antigen; PSMA: prostate-specific membrane antigen; BMI: body mass index; FFPE: formalin-fixed paraffin-embedded.

Jing Ning
Doctral Researcher @ Medizinische Universität Wien| Cancer Research
jing.ning@meduniwien.ac.at

Improvement of Gleason Grading Prediction in Prostate Cancer Stratification for Radical Prostatectomy: a Machine Learning- based Theranostic Multi-omics Study

Jing Ning*[1,2,3], Clemens Spielvogel*[1,3], David Haberl [1,3], Karolina Tractova [1,4], Stefan Stoiber [1,2], Sazan Rasul [3], Vojtech Bystry [4], Elisabeth Gurnhofer [2], Gerald Timelthaler [5], Laszlo Papp [3], Michaela Schlederer [2], Marcus Hacker [3], Alexander Haug [1,3], Lukas Kenner[1,2,6]

[1] Christian Doppler Laboratory for Applied Metabolomics, 1090 Vienna, Austria. [2] Division of Experimental and Translational Pathology, Department of Pathology, Medical University of Vienna, 1090 Vienna, Austria.
[3] Division of Nuclear Medicine, Department of Biomedical Imaging and Image-Guided Therapy, Medical University of Vienna, 1090 Vienna, Austria. [4] Central European Institute of Technology, Masaryk University, Brno 62500, Czech Republic.
[5] Unit of Laboratory Animal Pathology, University of Veterinary Medicine Vienna, 1210 Vienna, Austria. [6] CBmed Center for Biomarker Research in Medicine GmbH, 8010 Graz, Austria.

Background & Aim

Gleason Score (GS) in needle biopsy is the main determining factor for the decision of radical prostatectomy (RP). However, it brings various challenges to patients' quality of life, such as post-procedure infections and the multiple invasiveness. A promising standardized workflow is in urgent need to be well established for the aid of precise clinical decisions.

In this study, we aim to **predict the whole mount Gleason grading in prostate cancer for smart and precise patient stratification for radical prostatectomy using a high-throughput machine learning (ML) model and compare its predictive performance with that of needle biopsy.**

Patients and Materials From May 2014 to April 2020, 146 patients with newly diagnosed PCa in the Vienna General Hospital were retrospectively enrolled in this study, all of whom underwent ^{68}Ga-PSMA-11 PET/MR scans before radical prostatectomy in the nuclear medicine department of Vienna General Hospital. After the surgery, patients were followed up until 1st December 2021.

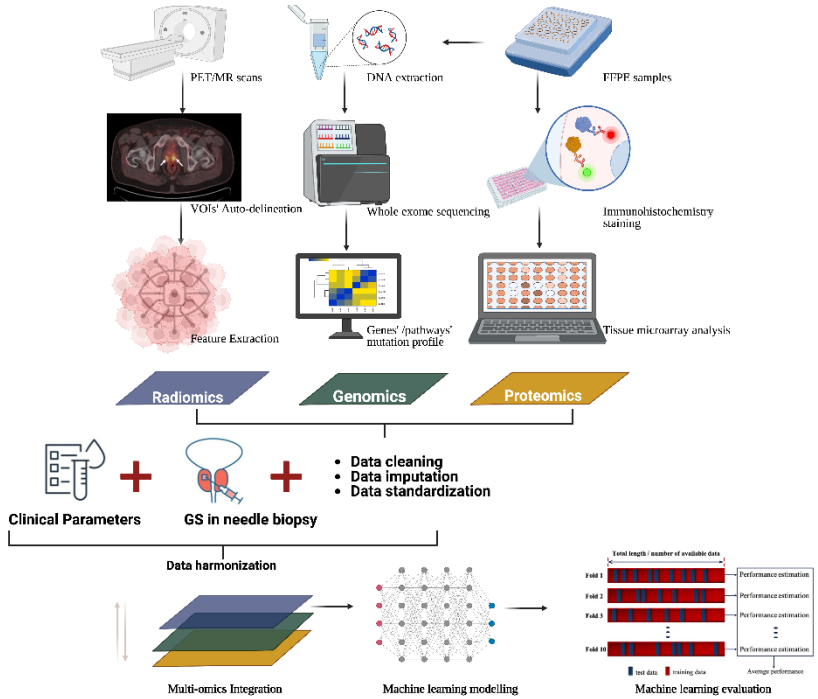

Improvement of Gleason Grading Prediction in Prostate Cancer Stratification for Radical Prostatectomy: a Machine Learning- based Theranostic Multi-omics Study

Jing Ning*[1,2,3], Clemens Spielvogel*[1,3], David Haberl [1,3], Karolina Tractova [1,4], Stefan Stoiber [1,2], Sazan Rasul [3], Vojtech Bystry [4], Elisabeth Gurnhofer [2], Gerald Timelthaler [5], Laszlo Papp [3], Michaela Schlederer [2], Marcus Hacker [3], Alexander Haug [1,3], Lukas Kenner[1,2,6]

[1] Christian Doppler Laboratory for Applied Metabolomics, 1090 Vienna, Austria. [2] Division of Experimental and Translational Pathology, Department of Pathology, Medical University of Vienna, 1090 Vienna, Austria.
[3] Division of Nuclear Medicine, Department of Biomedical Imaging and Image-Guided Therapy, Medical University of Vienna, 1090 Vienna, Austria. [4] Central European Institute of Technology, Masaryk University, Brno 62500, Czech Republic.
[5] Unit of Laboratory Animal Pathology, University of Veterinary Medicine Vienna, 1210 Vienna, Austria. [6] CBmed Center for Biomarker Research in Medicine GmbH, 8010 Graz, Austria.

01 Genomics

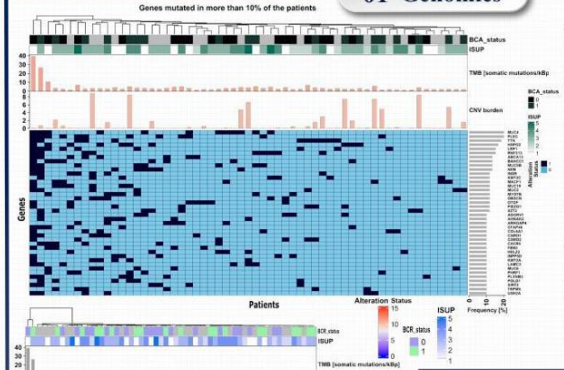

Fig. 1. Genes' mutation profile of the primary prostate cancer cohort with prognostic genomic biomarkers (CNV burden*, TMB*) and clinical markers (BCR* status and ISUP*). The figure profiled the genes with the frequency of more than 10% in the cohort but the distribution of genes mutations status is sparse. There is no clear associated pattern between the gene mutation profile and the clinical prognostic markers; For genomic markers, the gene mutation profile is consistent with TMB.

Fig. 2. The mutation profile of the PCa-related Pathways with prognostic genomic biomarkers (CNV burden*, TMB*) and clinical markers (BCR* status and ISUP*). There is no clear pattern between the prognostic markers and the mutation profile of pathways correlated with PCa tumorigenesis, progression and metastasis in our PCa cohort. However, according to the machine learning results, antifolate resistance, FoxO signaling pathway, cell cycle pathway are the top 3 potential pathways that can predict ISUP.

02 Pathomics

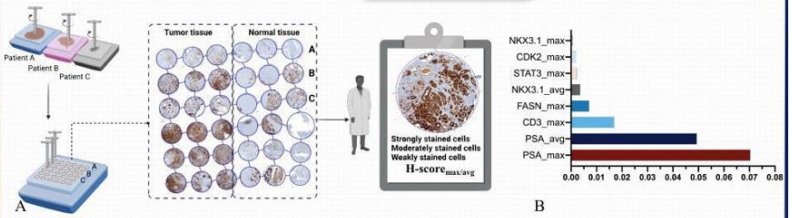

Fig. 3. The workflow of pathomics and important pathomic features derived from ML model to predict ISUP grading. (A) Derived from FFPE samples, we constructed the tumor microarray and stained them with potential prognostic biomarkers. Then pathologists assessed the IHC staining and gave the strongly/ moderately/ weakly stained cells, where H-score was calculated; **(B).**This bar plot showed PSA, CD3, FASN, NKX3.1, STAT3, CDK2 are the most contributing biomarkers to predict Gleason grading. Additionally, it showed the maximum value of the expression score performed better than average value of that.

Genomics Data Acquisition DNA was isolated from the formalin-fixed paraffin-embedded tissue (FFPE) samples derived from the radical prostatectomy. And whole exome sequencing (WES) analysis was performed.

Proteomics Data Acquisition We constructed the tissue microarray from RP specimens in a good pattern which allows a homogeneous fixation for the subsequent immunohistochemistry. Immunohistochemical analysis was performed with PCa-specific biomarkers.

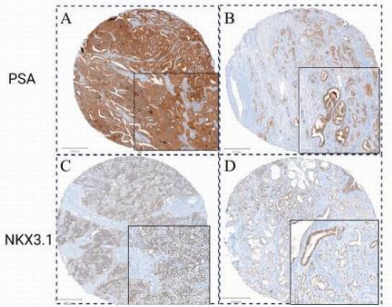

Fig. 4. Representative images of TMA cores stained with PSA and NKX3.1. A. TMA core and the details of tumor tissue with PSA high expression; **B.** TMA core and the details of tumor tissue with PSA low expression; **C.** TMA core and the details of tumor tissue with NKX3.1 high expression; **D.** TMA core and the details of tumor tissue with NKX3.1 low expression.

Improvement of Gleason Grading Prediction in Prostate Cancer Stratification for Radical Prostatectomy: a Machine Learning- based Theranostic Multi-omics Study

Jing Ning*[1,2,3], Clemens Spielvogel*[1,3], David Haberl [1,3], Karolina Tractova [1,4], Stefan Stoiber [1,2], Sazan Rasul [3], Vojtech Bystry [4], Elisabeth Gurnhofer [2], Gerald Timelthaler [5], Laszlo Papp [3], Michaela Schlederer [2], Marcus Hacker [3], Alexander Haug [1,3], Lukas Kenner[1,2,6]

[1] Christian Doppler Laboratory for Applied Metabolomics, 1090 Vienna, Austria. [2] Division of Experimental and Translational Pathology, Department of Pathology, Medical University of Vienna, 1090 Vienna, Austria.
[3] Division of Nuclear Medicine, Department of Biomedical Imaging and Image-Guided Therapy, Medical University of Vienna, 1090 Vienna, Austria. [4] Central European Institute of Technology, Masaryk University, Brno 62500, Czech Republic.
[5] Unit of Laboratory Animal Pathology, University of Veterinary Medicine Vienna, 1210 Vienna, Austria. [6] CBmed Center for Biomarker Research in Medicine GmbH, 8010 Graz, Austria.

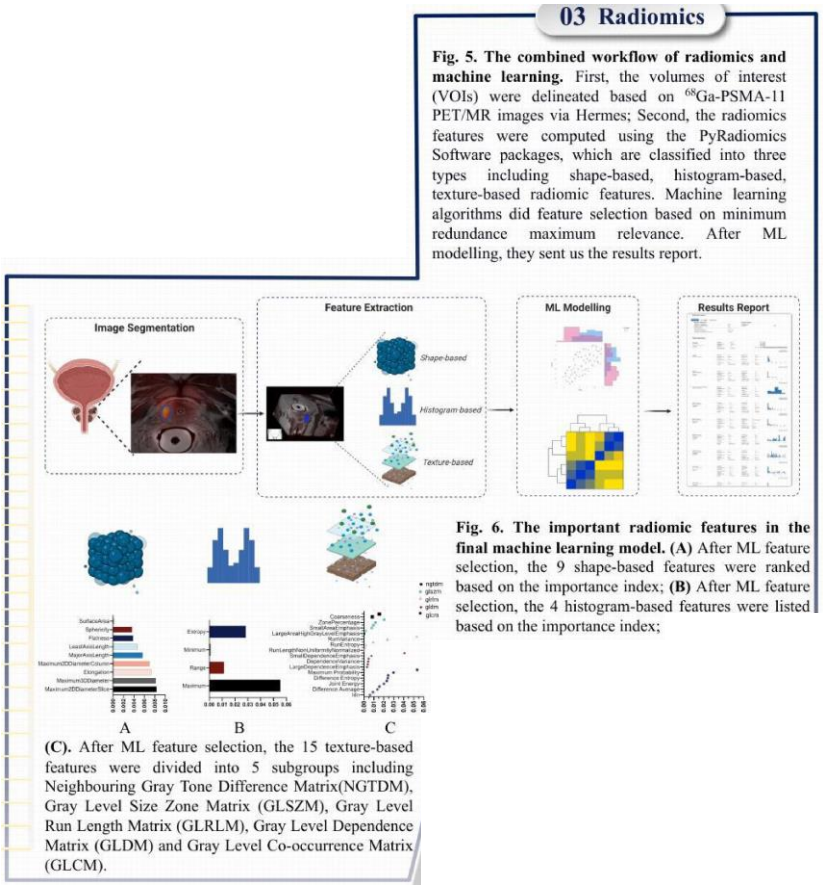

Fig. 5. The combined workflow of radiomics and machine learning. First, the volumes of interest (VOIs) were delineated based on ^{68}Ga-PSMA-11 PET/MR images via Hermes; Second, the radiomics features were computed using the PyRadiomics Software packages, which are classified into three types including shape-based, histogram-based, texture-based radiomic features. Machine learning algorithms did feature selection based on minimum redundance maximum relevance. After ML modelling, they sent us the results report.

Fig. 6. The important radiomic features in the final machine learning model. (A) After ML feature selection, the 9 shape-based features were ranked based on the importance index; **(B)** After ML feature selection, the 4 histogram-based features were listed based on the importance index; **(C).** After ML feature selection, the 15 texture-based features were divided into 5 subgroups including Neighbouring Gray Tone Difference Matrix(NGTDM), Gray Level Size Zone Matrix (GLSZM), Gray Level Run Length Matrix (GLRLM), Gray Level Dependence Matrix (GLDM) and Gray Level Co-occurrence Matrix (GLCM).

Radiomics Data Acquisition To ensure robustness, standardization and to avoid intra-operator and inter-operator variability, an automated U-net-based semantic segmentation algorithm was employed to automatically delineate the prostate based on T2WI images and subsequently perform a PET-based lesion segmentation on the previously created whole-prostate mask.

Improvement of Gleason Grading Prediction in Prostate Cancer Stratification for Radical Prostatectomy: a Machine Learning- based Theranostic Multi-omics Study

Jing Ning*[1,2,3], Clemens Spielvogel*[1,3], David Haberl [1,3], Karolina Tractova [1,4], Stefan Stoiber [1,2], Sazan Rasul [3], Vojtech Bystry [4], Elisabeth Gurnhofer [2], Gerald Timelthaler [5], Laszlo Papp [3], Michaela Schlederer [2], Marcus Hacker [3], Alexander Haug [1,3], Lukas Kenner[1,2,6]

[1] Christian Doppler Laboratory for Applied Metabolomics, 1090 Vienna, Austria. [2] Division of Experimental and Translational Pathology, Department of Pathology, Medical University of Vienna, 1090 Vienna, Austria.
[3] Division of Nuclear Medicine, Department of Biomedical Imaging and Image-Guided Therapy, Medical University of Vienna, 1090 Vienna, Austria. [4] Central European Institute of Technology, Masaryk University, Brno 62500, Czech Republic.
[5] Unit of Laboratory Animal Pathology, University of Veterinary Medicine Vienna, 1210 Vienna, Austria. [6] CBmed Center for Biomarker Research in Medicine GmbH, 8010 Graz, Austria.

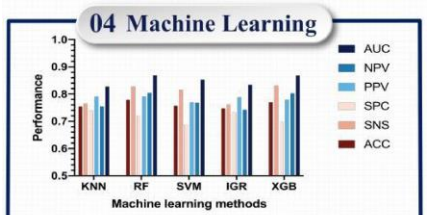

Fig. 7. The performance of different ML models to predict ISUP. Taking all the parameters together, RF* method has the best performance, whose ACC, SNS, SPC, PPV, NPV and AUC are 0.78, 0.83, 0.72, 0.79, 0.80 and 0.87 respectively.

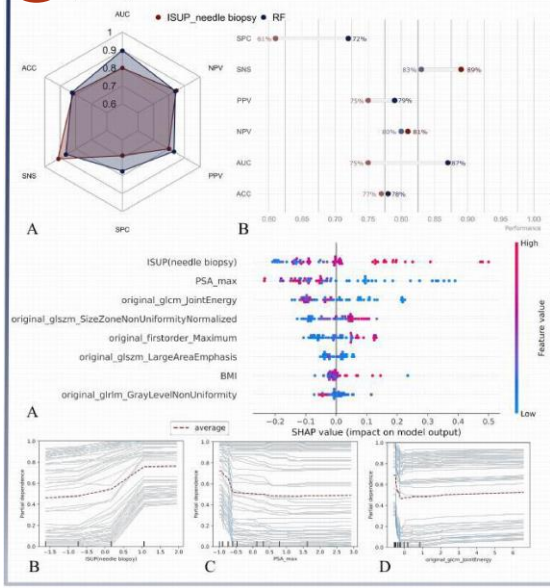

Fig. 8. The comparison of predictive performance between needle biopsy and RF. A. The radar chart showed the overall performance of RF is better than that of needle biopsy; **B.** The lollipop plot showed compared to needle biopsy, the SPC, PPV, ACC and AUC of RF to predict Gleason grading were elevated by 18% (0.61 vs 0.72), 7% (0.75 vs 0.79) 1% (0.77 vs 0.78) and 11% (0.75 vs 0.87) respectively while the SNS and NPV were decreased by 7% (0.89 vs 0.83) and 1% (0.81 vs 0.80).

Fig. 9. The most 8 important features in the RF model to predict Gleason grading of PCa. A. The SHAP value plot showed the most important 8 features and the correlation of these 8 features with ISUP. **B-D.** The partial importance plots of the top 3 features confirmed the relationship between the feature value with ISUP value.

ML-based Data Integration The EBM classification algorithm were applied to the integration of clinical parameters, radiomics data, genomics data and proteomics data. The classification results were validated using 10-fold Monte Carlo cross-validation to ensure robustness of performance metrics. To improve the interpretability of the model, relevant feature importance was derived using permutation feature importance.

Based on the potential prognostic genomic markers (tumor mutational burden and copy number variant burden) and clinical parameters (BCR status and ISUP), the heatmap (**Fig. 1**) showed the distribution of genes with the frequency of ≥10% cases are substantially sparse and there were no significant or meaningful correlation with the prognostic biomarkers. So, in the subsequent ML-based analysis, only pathway-level data will be used to conform to the balanced grouping standards of the machine learning system.

In the trial phase, the SNS, SPC, PPV, NPV, ACC and AUC of three ML-based approaches were respectively calculated and the resulting EBM classification algorithm gave the best performance with 0.75, 0.88, 0.75, 0.88, 0.83 and 0.81 accordingly as shown in **Fig. 2**. Then 10-fold Monte Carlo cross-validation ensures the robustness of performance metrics.

The performance of needle biopsy to predict Gleason grading is 0.62, 0.92, 0.81, 0.81 and 0.77 respectively. Compared to the performance of EBM model, the SNS, NPV, ACC and AUC were elevated by 13%, 7%, 2% and 4% while SPC, PPV were decreased by 4% and 6%.

Conclusion

Our findings demonstrate that our multiomics-based machine learning model has the better performance for the prediction of Gleason grading than the current clinical baseline, which potentially facilitates the clinical decision-making and personalized management of prostate cancer.

Modèle ne remplace pas la biopsie mais la complète

Improving treatment response prediction in lymphoma patients by generating synthetic [18F]-FDG-PET radiomic features using CTGAN

Yashar Ahmadyar[1], Rezvan Samimi[1], Alireza Kamali-Asl[1], Parham Geramifar[2]

[1] Department of Medical Radiation Engineering, Shahid Beheshti University, Tehran, Iran.
[2] Research Center for Nuclear Medicine, Shariati Hospital, Tehran University of Medical Sciences, Tehran, Iran.

June 24-27 2023 SNMMI ANNUAL MEETING Chicago, Illinois, USA

BACKGROUND

Major challenges

- Accurate prediction of lymphoma treatment outcome
- financial and psychological consequences of ineffective treatment
- Limited availability of large clinical datasets poses
- time-consuming of data collection
- most available datasets are small.

✓ Radiomics analysis of [18F]-FDG PET/CT images using machine learning methods provides quantitative information on intratumor heterogeneity for predicting treatment outcomes.

Aim

Generate synthetic PET radiomic features by implementing the **CTGAN algorithm** to develop a prediction model of chemotherapy response in lymphoma patients.

METHODS

1.Clinical Data and Radiomics Feature Extraction:.

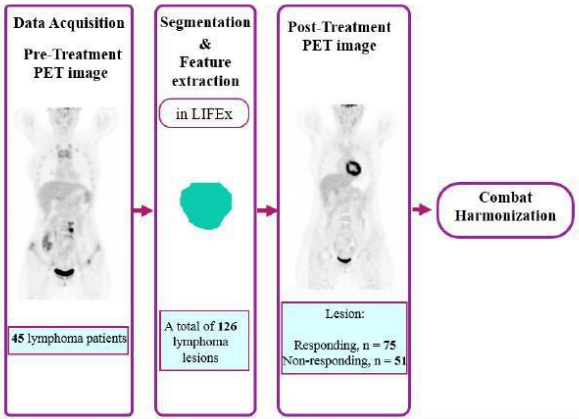

Fig 1. Flowchart of radiomics framework

In this retrospective study, we analysed 126 lymphoma lesions from 45 lymphoma patients from two different centers (75 responders and 51 non-responders to neoadjuvant chemotherapy). We used LIFEx software to extract radiomic features (shape, intensity, and texture) from pre-treatment PET images. Then we applied ComBat harmonization to each feature set to correct site variability.

Improving treatment response prediction in lymphoma patients by generating synthetic [18F]-FDG-PET radiomic features using CTGAN

Yashar Ahmadyar[1], Rezvan Samimi[1], Alireza Kamali-Asl[1], Parham Geramifar[2]

[1] Department of Medical Radiation Engineering, Shahid Beheshti University, Tehran, Iran.
[2] Research Center for Nuclear Medicine, Shariati Hospital, Tehran University of Medical Sciences, Tehran, Iran.

June 24-27 2023 SNMMI ANNUAL MEETING Chicago, Illinois, USA

BACKGROUND

Major challenges

- ❑ Accurate prediction of lymphoma treatment outcome
- ❑ financial and psychological consequences of ineffective treatment
- ❑ Limited availability of large clinical datasets poses
- ❑ time-consuming of data collection
- ❑ most available datasets are small.

✓ Radiomics analysis of [18F]-FDG PET/CT images using machine learning methods provides quantitative information on intratumor heterogeneity for predicting treatment outcomes.

Aim

Generate synthetic PET radiomic features by implementing the **CTGAN algorithm** to develop a prediction model of chemotherapy response in lymphoma patients.

METHODS

1.Clinical Data and Radiomics Feature Extraction:.

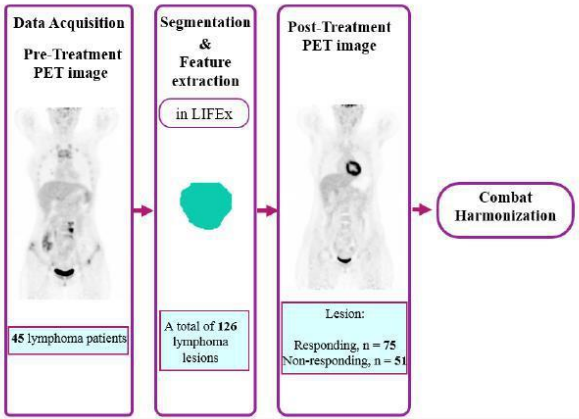

Fig 1. Flowchart of radiomics framework

2.Synthetic Feature Generation [1]:

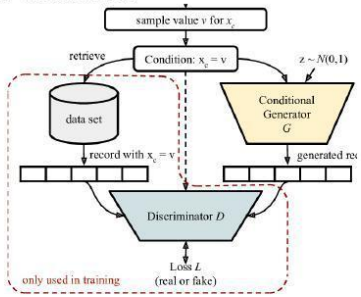

Fig 2. The CTGAN model operates by first sampling a condition and combining it with a random input to generate a sample. [2]

3. Model Development:

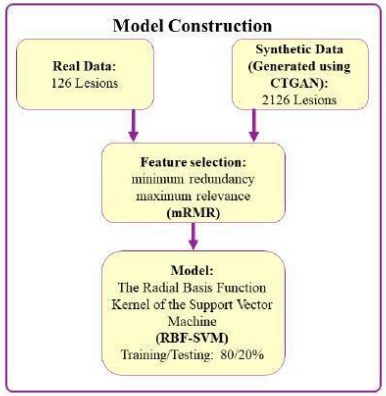

Fig 3. Model Development and Evaluation.

For synthetic feature generation, a Conditional tabular GAN (CTGAN) model has been used. CTGAN is a GAN-based model created to synthesize tabular data and transforms continuous values of a distribution into bounded vectors, which are appropriate for neural networks. In this model, the conditional generator has been used to resolve the problem of data imbalance during the sampling process. For the generator and discriminator, fully-connected networks were used to capture all correlations between columns. batch-normalization and Relu activation function applied in the generator. Using a mix activation functions, the synthetic row is generated after fully connected layers. In discriminator, leaky relu function and dropout on each hidden layer. Utilizing this model, 1000 synthetic patients with new features for complete response and 1000 patients with progressive disease were generated separately in 1000 epochs. The Radial Basis Function Kernel of the Support Vector Machine (RBF-SVM) model was developed by radiomic features before and after data augmentation using CTGAN. The minimum redundancy maximum relevance feature selection (mRMR) algorithm was used to select the ten most important features and eliminate the rest to reduce the computations in the algorithm. We utilized 80/20% splitting patient datasets for training/testing, respectively. We assessed the performance of the models, using the area under the receiver operator characteristic curve (AUC), accuracy, sensitivity, and specificity.

Improving treatment response prediction in lymphoma patients by generating synthetic [18F]-FDG-PET radiomic features using CTGAN

Yashar Ahmadyar[1], Rezvan Samimi[1], Alireza Kamali-Asl[1], Parham Geramifar[2]

[1] Department of Medical Radiation Engineering, Shahid Beheshti University, Tehran, Iran.
[2] Research Center for Nuclear Medicine, Shariati Hospital, Tehran University of Medical Sciences, Tehran, Iran.

June 24-27 2023 SNMMI ANNUAL MEETING Chicago, Illinois, USA

BACKGROUND

Major challenges

- Accurate prediction of lymphoma treatment outcome
- financial and psychological consequences of ineffective treatment
- Limited availability of large clinical datasets poses
- time-consuming of data collection
- most available datasets are small.

✓ Radiomics analysis of [18F]-FDG PET/CT images using machine learning methods provides quantitative information on intratumor heterogeneity for predicting treatment ou

Gener
develo

MET

1.Cli

While both models could accurately predict response to therapy, the performance of the predictive model was improved after data augmentation using CTGAN. The ROC curve of these models for the test set are shown in Figure 1. The AUC and accuracy increased following augmentation from 0.85 to 0.92 and from 0.84 to 0.92, respectively. The SVM model achieves sensitivity and specificity of 0.92 and 0.91 with data augmentation. Specificity increased by 19% and Sensitivity increased by 3% after increasing the number of data to 2126 using CTGAN.

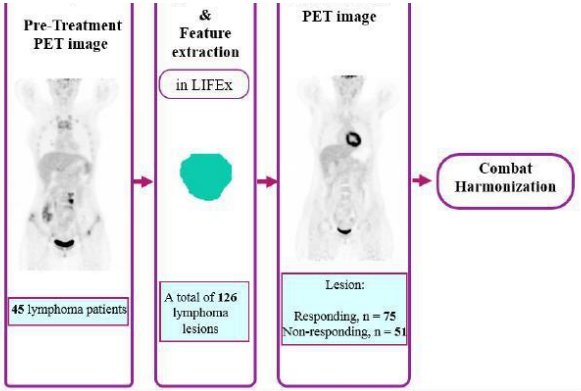

Fig 1. Flowchart of radiomics framework

2.Synthetic Feature Generation [1]:

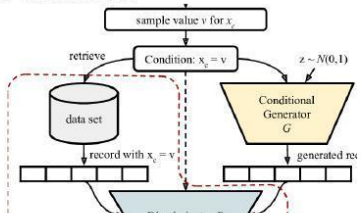

Fixer les effectifs du test set !!

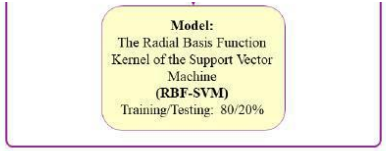

Fig 3. Model Development and Evaluation.

RESULTS

•The ROC curve of the models for the test set are seen in Figure 4.

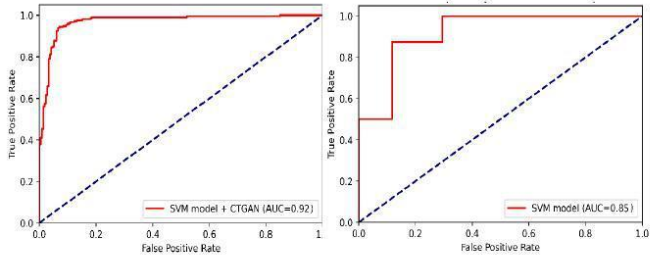

Fig 4. The ROC curve of SVM classifier with (left) and without (right) data augmentation using CTGAN

TABLE 1. Evaluation Metrics for SVM and SVM+CTGAN models

Model	ACC	AUC	SEN	SPE
SVM	84%	85%	88%	72%
SVM+CTGAN	92%	92%	92%	91%

CONCLUSION

This study demonstrated:

- the capability of data augmentation using CTGAN for treatment response prediction of lymphoma patients.
- incorporating synthetic PET radiomics features can improve the performance of SVM models when there is insufficient data available.

REFERENCES:

1. Xu L, Skoularidou M, Cuesta-Infante et al. 2019.
2. Borisov, Leemann et al. 2022

Evaluation of clinical variables affecting myocardial glucose uptake in diabetic patients

Yeongjoo Lee, M.D.[1], J aehyuk J ang, M.D[2], Sae Jung Na, M.D. PhD.[1]
[1]Division of Nuclear Medicine Department of Radiology, Uijeongbu St. Mary's Hospital, College of Medicine, The Catholic University of Korea, Seoul, Republic of Korea
[2]Division of Cardiology, Department of Internal Medicine, Uijeongbu St. Mary's Hospital, College of Medicine, The Catholic University of Korea, Seoul, Republic of Korea

Backgrounds

- ✓ About 39% of adults were overweight in 2016, and 13% were obese worldwide
  - World Health Organization, 2021
- ✓ Lipotoxic status such as obesity and type 2 diabetes shift the heart toward more fat use.
  - Nuclear cardiology & multimodal cardiovascular imaging, 2021. Chapter 19. Peterson et al.
- ✓ According to the ASNC Imaging guideline/SNMMI procedure standard (2016), the patient preparation for F-18 FDG PET cardiac viability assessment is solely based on the blood glucose (BG) level.
- ✓ Diabetic patients sometimes show insufficient myocardial glucose uptake, which leads to difficulties in interpretation.

- No conflict of Interest.
- This study was not funded.

Objective

To evaluate several clinical variables that may affect myocardial glucose metabolism in diabetic patients.

Evaluation of clinical variables affecting myocardial glucose uptake in diabetic patients

Yeongjoo Lee, M.D.[1], J aehyuk J ang, M.D[2], Sae Jung Na, M.D. PhD.[1]
[1]Division of Nuclear Medicine Department of Radiology, Uijeongbu St. Mary's Hospital, College of Medicine, The Catholic University of Korea, Seoul, Republic of Korea
[2]Division of Cardiology, Department of Internal Medicine, Uijeongbu St. Mary's Hospital, College of Medicine, The Catholic University of Korea, Seoul, Republic of Korea

Backgrounds

- ✓ About 39% of adults were overweight in 2016, and 13% were obese worldwide
  - World Health Organization, 2021
- ✓ Lipotoxic status such as obesity and type 2 diabetes shift the heart toward more fat use.
  - Nuclear cardiology & multimodal cardiovascular imaging, 2021. Chapter 19. Peterson et al.
- ✓ According to the ASNC Imaging guideline/SNMMI procedure standard (2016), the patient preparation for F-18 FDG PET cardiac viability assessment is solely based on the blood glucose (BG) level.
- ✓ Diabetic patients sometimes show insufficient myocardial glucose uptake, which leads to difficulties in interpretation.

- No conflict of Interest.
- This study was not funded.

Objective

To evaluate several clinical variables that may affect myocardial glucose metabolism in diabetic patients.

Material and Methods (1)

- Retrospective study (May, 2018 ~ November, 2022)
- Single center with single PET/CT machine.

Inclusion criteria

1) Cardiac FDG PET/CT images for myocardial viability assessment
2) Clinically diagnosed diabetes type 2 patients

Material and Methods (2)

1. Patient preparation

- Acipimox (lipid lowering agent): 250 mg
- Oral glucose loading of 50 g (46.1±9.1)
- With/without RI (regular insulin) depends on the blood sugar level after oral glucose loading

2. PET/CT scan:

(1) F-18 FDG PET/CT
- 40 True-point with true V, Siemens Medical Solutions, Knoxville, TN, USA
- Average dose of 370 MBq (10.4 ± 0.58 mCi)

(2) Measurement
3cm sized sphere of Region of Interest (ROI):
- SUVmax of LV (left ventricle)
- SUVmean of liver

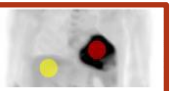

Myocardial Glucose Uptake Ratio (MGUR) = $\frac{SUVmax\ of\ LV}{SUVmean\ of\ liver}$

- Fasting BST (Blood Sugar Test)
- BST after glucose loading
- BST at radiotracer injection
- Injection to imaging time

3. Clinical parameters

- height, weight, age, sex
- HbA1c, Total cholesterol, LDL, HDL, Triglyceride, troponin T, CK-MB
- All lab data were acquired within a month (3.54 ± 11.3 d) from PET/CT image

4. Data analysis

Group comparisons after dichotomization according to MGUR (below average vs. above average) and BMI (Body Mass Index; Non-obese group, BMI<25 vs Obese group, BMI ≥ 25)

Statistical Package for the Social Science version 24.0 (IBM corporation, Armonk, New York, USA)
Pearson correlation test, student's t-test, Multiple linear regression

Evaluation of clinical variables affecting myocardial glucose uptake in diabetic patients

Yeongjoo Lee, M.D.[1], J aehyuk J ang, M.D[2], Sae Jung Na, M.D. PhD.[1]
[1]Division of Nuclear Medicine Department of Radiology, Uijeongbu St. Mary's Hospital, College of Medicine, The Catholic University of Korea, Seoul, Republic of Korea
[2]Division of Cardiology, Department of Internal Medicine, Uijeongbu St. Mary's Hospital, College of Medicine, The Catholic University of Korea, Seoul, Republic of Korea

Results (1)

Table 1. Comparison of the variables between low MGUR and high MGUR group

Patients	N = 109		
Variables	Low MGUR group (n=57, 2.8±1.1)	High MGUR group (n=52, 5.9±1.4)	*p*-value
Sex (M:F)	57 (43: 14)	52 (42: 10)	N/A
Age (mean ±SD)	67.9 ± 11.6	65.6 ± 9.1	0.236
Height	163.1 ± 8.9	164.9 ± 9.7	0.302
Weight	69.1 ± 14.2	65.4 ± 12.1	0.150
BMI	25.8 ± 4.0	24.0 ± 3.6	0.016*
Fasting BST	138.5 ± 46.4	138.9 ± 33.4	0.960
Loading BST	217.8 ± 59.4	229.3 ± 54.7	0.299
Injection BST	216.3 ± 58.4	223.0 ± 44.7	0.506
Insulin dose	2.6 ± 2.0	3.4 ± 2.4	0.068
Total cholesterol	150.4 ± 61.4	145.6 ± 46.9	0.647
Triglyceride	167.6 ± 118.2	126.8 ± 75.9	0.038*
HDL	38.1 ± 9.1	39.5 ± 11.9	0.495
LDL	81.2 ± 52.9	83.7 ± 44.3	0.798
Troponin T	0.64 ± 1.68	0.78 ± 1.85	0.662
CK-MB	11.8 ± 29.4	18.2 ± 52.8	0.429
HbA1c	7.8 ± 1.5	7.4 ± 1.9	0.209

MGUR

*Statistically significant

Table 2. Comparison of the variables between non-obese and obese group

Patients	N = 109		
Variables	Non-obese group (BMI < 25, n=55)	Obese group (BMI ≥ 25, n=54)	*p*-value
Sex (M:F)	55 (42: 13)	54 (43: 11)	N/A
Age (year)	67.4 ± 11.0	66.2 ± 10.0	0.549
Height	164.5 ±10.1	164.1 ± 9.5	0.825
Weight	59.2 ± 9.9	75.6 ± 11.0	<0.001*
Fasting BST	141.9 ± 41.9	135.4 ± 39.2	0.404
Loading BST	225.9 ± 58.2	220.8 ± 56.7	0.651
Injection BST	222.9 ± 55.4	216.0 ± 49.0	0.488
Insulin dose	3.2 ± 2.2	2.7 ± 2.2	0.258
Injection to image time	76.1 ± 34.4	79.5 ± 33.2	0.596
Total cholesterol	144.8 ± 51.9	151.3 ± 57.6	0.538
Triglyceride	129.5 ± 82.2	166.4 ± 115.9	0.061
HDL	40.6 ± 13.1	36.8 ± 6.7	0.066
LDL	79.4 ± 43.8	85.3 ± 53.5	0.532
Troponin T	0.62 ± 1.74	0.80 ± 1.78	0.590
CK-MB	11.7 ± 36.4	18.0 ± 47.4	0.440
HbA1c	7.6 ± 1.7	7.6 ± 1.7	0.946
MGUR	4.7 ± 2.2	3.8 ±1.6	0.016*

*Statistically significant

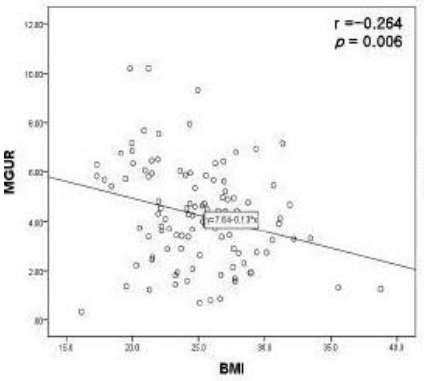

Figure 1. A scatter plot of BMI and MGUR; BMI has a negative correlation with MGUR.

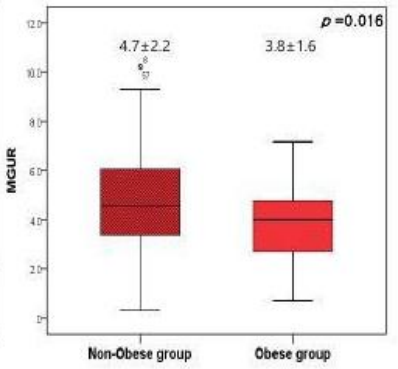

Figure 2. A box plot of group comparison after dichotomization according to the BMI
(Non-obese: BMI<25, Obese: BMI≥ 25)

Cases

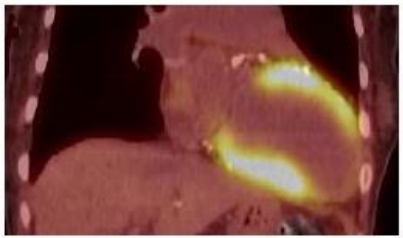

(A) F/66 BMI 17.9, insulin 4 U, FDG: 10.6 mCi, 120 min image, SUVmax: 10.8, MGUR: 5.7

(B) F/83, BMI: 35.6, insulin 4 U, FDG: 10.1 mCi, 120 min image, SUVmax: 4.5, MGUR: 1.3

Conclusion

- Among many clinical variables, obesity had a negative correlation with myocardial glucose uptake in patients with diabetes.
- In obese and diabetic patients, sufficient insulin administration is required to enhance myocardial glucose uptake.

Chimeric Antigen Receptor T-cell Treatment for Non-Hodgkin Lymphoma: A Comprehensive Bone Marrow Evaluation with FDG PET/CT

Bimash B Shrestha[1] , Shashi Singh[2], Miraziz Ismoilov[1] Saira Khan Niazi[1], Malia Ahmed[1], Niloofaralsadat Motamedi[1], Thomas J. Werner[1], Mona-Elisabeth R Revheim[3], Poul Flemming Høilund-Carlsen[4], Abass Alavi[1], William Y Raynor[5]

[1]Department of Radiology, University of Pennsylvania, Philadelphia, PA; [2]Department of Radiology, Stanford University School of Medicine, Palo Alto, CA; [3]Oslo University Hospital and University of Oslo, Oslo, Norway; [4] Department of Clinical Research, University of Southern Denmark, Odense Oslo University Hospital and University of Oslo, Oslo, Norway; [5]Rutgers Robert Wood Johnson Medical School

Purpose

- To measure the global bone marrow uptake of ^{18}F-fluorodeoxyglucose (FDG) before and after treatment in non-Hodgkin lymphoma (NHL) patients who underwent Chimeric Antigen Receptor T-cell (CAR-T) therapy in order to characterize response to therapy.

Chimeric Antigen Receptor T-cell Treatment for Non-Hodgkin Lymphoma: A Comprehensive Bone Marrow Evaluation with FDG PET/CT

Bimash B Shrestha[1] , Shashi Singh[2], Miraziz Ismoilov[1] Saira Khan Niazi[1], Malia Ahmed[1], Niloofaralsadat Motamedi[1], Thomas J. Werner[1], Mona-Elisabeth R Revheim[3], Poul Flemming Høilund-Carlsen[4], Abass Alavi[1], William Y Raynor[5]

[1]Department of Radiology, University of Pennsylvania, Philadelphia, PA; [2]Department of Radiology, Stanford University School of Medicine, Palo Alto, CA; [3]Oslo University Hospital and University of Oslo, Oslo, Norway; [4] Department of Clinical Research, University of Southern Denmark, Odense Oslo University Hospital and University of Oslo, Oslo, Norway; [5]Rutgers Robert Wood Johnson Medical School

Purpose

- To measure the global bone marrow uptake of ^{18}F-fluorodeoxyglucose (FDG) before and after treatment in non-Hodgkin lymphoma (NHL) patients who underwent Chimeric Antigen Receptor T-cell (CAR-T) therapy in order to characterize response to therapy.

Methods

- Retrospective FDG PET/CT data of 60 NHL patients (mean age 60.3 ± 12.48 years, range 29-81, females 22) who underwent CAR-T therapy were included (3 patients excluded as their baseline scans were performed at an outside facility). All scans were acquired 60 min following intravenous injection of 4 MBq/kg of FDG.
- Baseline scans before initiation of CAR-T therapy for relapsed or refractory NHL and scans at first follow-up after an average of 72 days (ranges 21-179 days) after treatment were analyzed.
- Images were analyzed using an iterative thresholding algorithm that delineates a continuous region based on Hounsfield units (OsiriX MD version 12.5.2 software; Pixmeo SARL; Bernex, Switzerland), allowing for segmentation of the total skeleton on a fused FDG PET/CT image.
- This enabled the quantification of FDG uptake representing the entire skeleton, providing a global SUVmean that considers all bone marrow involvement.
- Global SUVmean were compared before and after treatment using Wilcoxon signed-rank test.

Figure 1

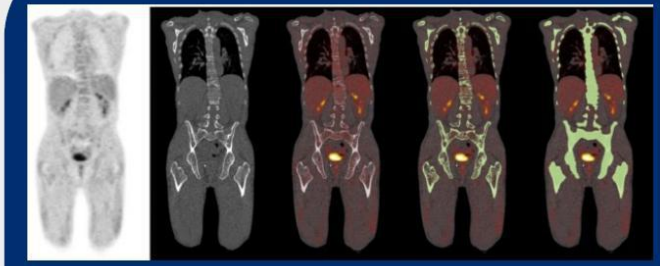

FDG PET, CT, and fused FDG PET-CT images demonstrating CT-based segmentation of bone marrow activity.[1] An iterative Hounsfield unit threshold was applied, followed by a morphological closing algorithm. Global SUVmean was calculated as the average SUV of all voxel contained within the region of interest.

Figure 2

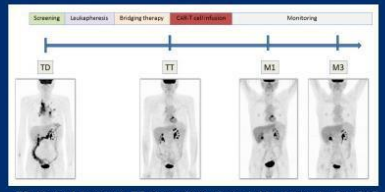

Maximum intensity projections demonstrating serial FDG PET/CT imaging in a lymphoma patient receiving CAR-T therapy.[2]

TD (time of decision), TT (time of transfusion), M1 (1 month after CAR-T cell infusion), and M3 (3 months evaluation after CAR-T cells infusion)

Chimeric Antigen Receptor T-cell Treatment for Non-Hodgkin Lymphoma: A Comprehensive Bone Marrow Evaluation with FDG PET/CT

Bimash B Shrestha[1] , Shashi Singh[2], Miraziz Ismoilov[1] Saira Khan Niazi[1], Malia Ahmed[1], Niloofaralsadat Motamedi[1], Thomas J. Werner[1], Mona-Elisabeth R Revheim[3], Poul Flemming Høilund-Carlsen[4], Abass Alavi[1], William Y Raynor[5]

[1]Department of Radiology, University of Pennsylvania, Philadelphia, PA; [2]Department of Radiology, Stanford University School of Medicine, Palo Alto, CA; [3]Oslo University Hospital and University of Oslo, Oslo, Norway; [4] Department of Clinical Research, University of Southern Denmark, Odense Oslo University Hospital and University of Oslo, Oslo, Norway; [5]Rutgers Robert Wood Johnson Medical School

Purpose

- To measure the global bone marrow uptake of ^{18}F-fluorodeoxyglucose (FDG) before and after treatment in non-Hodgkin lymphoma (NHL) patients who underwent Chimeric Antigen Receptor T-cell (CAR-T) therapy in order to characterize response to therapy.

Methods

- Retrospective FDG PET/CT data of 60 NHL patients (mean age 60.3 ± 12.48 years, range 29-81, females 22) who underwent CAR-T therapy were included (3 patients excluded as their baseline scans were performed at an outside facility). All scans were acquired 60 min following intravenous injection of 4 MBq/kg of FDG.
- Baseline scans before initiation of CAR-T therapy for relapsed or refractory NHL and scans at first follow-up after an average of 72 days (ranges 21-179 days) after treatment were analyzed.
- Images were analyzed using an iterative thresholding algorithm that delineates a continuous region based on Hounsfield units (OsiriX MD version 12.5.2 software; Pixmeo SARL; Bernex, Switzerland), allowing for segmentation of the total skeleton on a fused FDG PET/CT image.
- This enabled the quantification of FDG uptake representing the entire skeleton, providing a global SUVmean that considers all bone marrow involvement.
- Global SUVmean were compared before and after treatment using Wilcoxon signed-rank test.

Figure 1

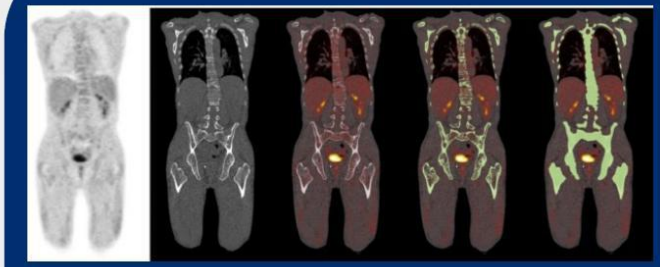

FDG PET, CT, and fused FDG PET-CT images demonstrating CT-based segmentation of bone marrow activity.[1] An iterative Hounsfield unit threshold was applied, followed by a morphological closing algorithm. Global SUVmean was calculated as the average SUV of all voxel

in a lymphoma patient receiving CAR-T therapy.[2]

TD (time of decision), TT (time of transfusion), M1 (1 month after CAR-T cell infusion), and M3 (3 months evaluation after CAR-T cells infusion)

Lien avec la réponse aux traitements ? Quelle(s) différence(s) entre les patients Δ+ et Δ- ?

Results

- The average global SUVmean before treatment was 1.27 ± 0.34 (range 0.84 to 2.39), whereas the average after treatment was 1.15 ± 0.29 (range 0.69 to 2.82).
- The average change was -0.13 ± 0.36 (range -1.55 to 1.01) (p= 0.003). The calculated global SUVmean uptake decreased after initiation of treatment in 39 (68.4%) and increased in 18 (31.6%) of the cases.

Conclusion

- This study demonstrated a significant decrease in FDG uptake from baseline to post-treatment in the bone marrow of NHL patients who had undergone CAR-T therapy.
- This decrease in FDG uptake in the bone marrow potentially signifies a reduction in bone marrow tumor burden following CAR-T therapy.
- Thus, global assessment of the bone marrow by FDG PET/CT imaging is a useful tool for the assessment of the effects of CAR-T therapy in the bone marrow of patients with NHL.

References

1. Raynor WY, Al-Zaghal A, Zadeh MZ, Seraj SM, Alavi A. Metastatic Seeding Attacks Bone Marrow, Not Bone: Rectifying Ongoing Misconceptions. PET Clin. 2019 Jan;14(1):135-144. doi: 10.1016/j.cpet.2018.08.005. PMID: 30420215.
2. Linguanti F, Abenavoli EM, Berti V, Lopci E. Metabolic Imaging in B-Cell Lymphomas during CAR-T Cell Therapy. Cancers (Basel). 2022 Sep 27;14(19):4700. doi: 10.3390/cancers14194700. PMID: 36230629; PMCID: PMC9562671.

Influence of Metabolic Tumor Burden on reference tissues' Standardized Uptake Values in ^{18}F-FDG PET/CT sequential imaging of lymphoma patients

Ahmed Kandeel, MD, Marwa Maamoun, MD, Ahmed Badawy, MD, Hoda Anwar, MD.

Kasr Alainy Center of Radiation Oncology and Nuclear Medicine (NEMROCK), Cairo, Egypt.

Chicago, Illinois, USA 2023

Objectives and Aim of Work

Background: ^{18}F-FDG PET/CT has become a crucial technique for guiding response-adapted treatment in lymphoma patients by implementing the Deauville five-point scale. FDG distribution in normal organs and neoplastic tissues can be influenced by multiple biological and procedural factors with intra-patient variability in reference organs that can create a sink effect that reduces tracer availability to other tissues thus potentially affecting the reliability of reference organs in sequential PET/CT scans.

Aim of work: To correlate the values of metabolic tumor burden (MTB) with the standardized uptake values (SUV) in different normal reference tissues in both the initial staging and follow-up PET/CT studies; in order to determine the potential effect of tumor burden on established PET-CT-based criteria for evaluating the response.

Influence of Metabolic Tumor Burden on reference tissues' Standardized Uptake Values in ^{18}F-FDG PET/CT sequential imaging of lymphoma patients

Ahmed Kandeel, MD, Marwa Maamoun, MD, Ahmed Badawy, MD, Hoda Anwar, MD.

Kasr Alainy Center of Radiation Oncology and Nuclear Medicine (NEMROCK), Cairo, Egypt.

Chicago, Illinois, USA 2023

Objectives and Aim of Work

Background: ^{18}F-FDG PET/CT has become a crucial technique for guiding response-adapted treatment in lymphoma patients by implementing the Deauville five-point scale. FDG distribution in normal organs and neoplastic tissues can be influenced by multiple biological and procedural factors with intra-patient variability in reference organs that can create a sink effect that reduces tracer availability to other tissues thus potentially affecting the reliability of reference organs in sequential PET/CT scans.

Aim of work: To correlate the values of metabolic tumor burden (MTB) with the standardized uptake values (SUV) in different normal reference tissues in both the initial staging and follow-up PET/CT studies; in order to determine the potential effect of tumor burden on established PET-CT-based criteria for evaluating the response.

Methods

Our prospective study was done on **54 patients** who were referred for sequential PET/CT examinations for various types of malignant lymphomas.

- Mean values for BMI, blood glucose level, injected dose, and interval uptake period did not significantly change between the two studies, in addition, no changes to equipment, software, or imaging protocol were made.

. Maximum SUVs were obtained from reference organs (liver, blood pool, brain, and muscles) taking into consideration not to involve areas with abnormal ^{18}F-FDG uptake such as disease involvement, focal muscle uptake, focal atherosclerotic disease...etc.

- Values were correlated with metabolic tumor burden (MTB) (the sum of the TLG values of all lesions) in each patient.

- Patients were divided according to their response to therapy -in reference to Deauville criteria- into **3 groups**:

. **Progression** in 11 patients (20%).

. **Regression** in 37 patients (68%).

. **Resolution** in 6 patients (12%).

- **Correlation and Comparison analyses** were done between initial and follow-up scans regarding the % change in MTB and % change of SUV in reference organs in each response group.

Influence of Metabolic Tumor Burden on reference tissues' Standardized Uptake Values in ^{18}F-FDG PET/CT sequential imaging of lymphoma patients

Ahmed Kandeel, MD, Marwa Maamoun, MD, Ahmed Badawy, MD, Hoda Anwar, MD.

Kasr Alainy Center of Radiation Oncology and Nuclear Medicine (NEMROCK), Cairo, Egypt.

Chicago, Illinois, USA 2023

Objectives and Aim of Work

Background: ^{18}F-FDG PET/CT has become a crucial technique for guiding response-adapted treatment in lymphoma patients by implementing the Deauville five-point scale. FDG distribution in normal organs and neoplastic tissues can be influenced by multiple biological and procedural factors with intra-patient variability in reference organs that can create a sink effect that reduces tracer availability to other tissues thus potentially affecting the reliability of reference organs in sequential PET/CT scans.

Aim of work: To correlate the values of metabolic tumor burden (MTB) with the standardized uptake values (SUV) in different normal reference tissues in both the initial staging and follow-up PET/CT studies; in order to determine the potential effect of tumor burden on established PET-CT-based criteria for evaluating the response.

Methods

Our prospective study was done on **54 patients** who were referred for sequential PET/CT examinations for various types of malignant lymphomas.

- Mean values for BMI, blood glucose level, injected dose, and interval uptake period did not significantly change between the two studies, in addition, no changes to equipment, software, or imaging protocol were made.

. Maximum SUVs were obtained from reference organs (liver, blood pool, brain, and muscles), taking into consideration not to involve areas with abnormal ^{18}F -FDG uptake such as disease involvement, focal muscle uptake, focal atherosclerotic disease...etc.

- Values were correlated with metabolic tumor burden (MTB) (the sum of the TLG values of all lesions) in each patient.

- Patients were divided according to their response to therapy -in reference to Deauville criteria- into **3 groups**:

. **Progression** in 11 patients (20%).

. **Regression** in 37 patients (68%).

. **Resolution** in 6 patients (12%).

- **Correlation and Comparison analyses** were done between initial and follow-up scans regarding the % change in MTB and % change of SUV in reference organs in each response group.

Results

- Correlation analysis: there **was** a significant negative correlation between % change in MTB with % change of SUV in liver, blood pool, brain but not in muscles.

- Comparison analysis: There **was** a significant difference between **progression and regression groups** in the % of MTB change and % of SUV change in the liver and brain.

- There **was** a significant difference between **progression and resolution groups in the** % of MTB change and % of SUV change in the brain only.

- There **was no** significant difference between **regression and resolution groups** in the % of MTB change and % of SUV change in any of the reference organs.

Table 1. Correlation Analysis between percent of change of metabolic tumor burden and percent of change in SUVmax of different reference organs during ^{18}F-FDG PET/CT sequential Imaging in 54 lymphoma patients.

Metabolic Tumor Burden	Liver SUV% change = 4.79%	Blood pool SUV % change = 6.56%	Brain SUV % change = 8.62%	Muscles SUV % change = 0.66%
MTB % change = 318.95%	R= -0.467 P= <0.001	R= -0.291 P= <0.033	R= -0.417 P=0.002	Non Sig.

Table 2. Comparison between different response groups in 54 lymphoma patients.

In lymphoma cases % of change in:		MTB	Liver SUVmax	Blood pool SUVmax	Brain SUVmax	Muscle SUVmax
Progression VS Regression	Mean difference	2026.826	-17.256	-19.491	-26.786	-6.852
	P value	<0.001	0.001	NS	<0.001	NS
Progression VS Resolution	Mean difference	2033.663	-10.050	-10.770	-34.290	8.882
	P value	<0.001	NS	NS	0.002	NS
Regression VS Resolution	Mean difference	6.837	7.206	8.722	-7.504	15.734
	P value	NS	NS	NS	NS	NS

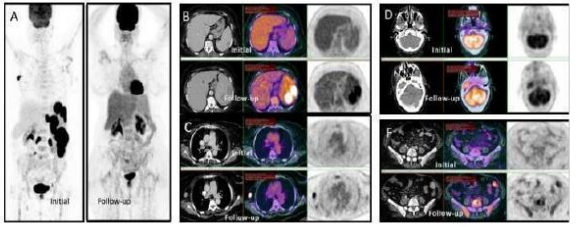

Female patient, 65-year-old with a history of Non-Hodgkin lymphoma, showing marked metabolic regression after chemotherapy treatment.

A. MIP images of initial study (MTB=6020) and at follow-up study (MTB=34) with (% of change = -99.4%).

B. Liver; 3 cm ROI within the right lobe in initial study (SUVmax=3.1) and at follow-up study (SUVmax=3.7) with (% of change=19.3%).

C. Mediastinal Blood Pool; 1.2 cm ROI within descending aorta in initial study (SUVmax=2.1) and at follow-up study (SUVmax=2.8) with (% of change=33.3%).

D. Brain; 1.2 cm ROI at the right cerebellum in initial study (SUVmax=7.2) and at follow-up study (SUVmax=9) with (% of change=25%).

F. Muscles; 1.2 cm ROI within right psoas major muscle in initial study (SUVmax=1) and at follow-up study (SUVmax=1) with (% of change=0%).

Influence of Metabolic Tumor Burden on reference tissues' Standardized Uptake Values in ^{18}F-FDG PET/CT sequential imaging of lymphoma patients

Ahmed Kandeel, MD, Marwa Maamoun, MD, Ahmed Badawy, MD, Hoda Anwar, MD.
Kasr Alainy Center of Radiation Oncology and Nuclear Medicine (NEMROCK), Cairo, Egypt.

Chicago, Illinois, USA 2023

Objectives and Aim of Work

Background: ^{18}F-FDG PET/CT has become a crucial technique for guiding response-adapted treatment in lymphoma patients by implementing the Deauville five-point scale. FDG distribution in normal organs and neoplastic tissues can be influenced by multiple biological and procedural factors with intra-patient variability i
tracer availability
erence organs in

Aim of work: To
with the standar
tissues in both t
to determine the
based criteria fo

Tester si différence significative de SUVmean(organes) entre TEP0 et TEP1 suivant le groupe de patients ?

Our prospective
quential PET/CT e

- Mean values for
period did not significantly change between the two studies, in addition, no changes to equipment, software, or imaging protocol were made.
. Maximum SUVs were obtained from reference organs (liver, blood pool, brain, and muscles), taking into consideration not to involve areas with abnormal ^{18}F -FDG uptake such as disease involvement, focal muscle uptake, focal atherosclerotic disease...etc.
- Values were correlated with metabolic tumor burden (MTB) (the sum of the TLG values of all lesions) in each patient.
- Patients were divided according to their response to therapy -in reference to Deauville criteria- into **3 groups**:
. **Progression** in 11 patients (20%).
. **Regression** in 37 patients (68%).
. **Resolution** in 6 patients (12%).
- **Correlation and Comparison analyses** were done between initial and follow-up scans regarding the % change in MTB and % change of SUV in reference organs in each response group.

Results

- **Correlation analysis:** there **was** a significant negative correlation between % change in MTB with % change of SUV in liver, not in muscles.

lysis: There **was** a significant difference be-
and regression groups in the % of MTB
V change in the liver and brain.

ificant difference between **progression and**
in the % of MTB change and % of SUV
nly.

- There **was no** significant difference between **regression and resolution groups** in the % of MTB change and % of SUV change in any of the reference organs.

Conclusion

Metabolic tumor burden can potentially affect ^{18}F-FDG biodistribution in reference organs, which has a negative impact on semiquantitative analysis during the interpretation of sequential studies. In lymphoma patients, normalizing tumor FDG uptake can be done to muscles as a potential stable reference tissue given that all other factors that could alter biodistribution (e.g. blood glucose level) were taken into consideration.

Table 1. Correlation Analysis between percent of change of metabolic tumor burden and percent of change in SUVmax of different reference organs during ^{18}F-FDG PET/CT sequential Imaging in 54 lymphoma patients.

Metabolic Tumor Burden	Liver SUV% change = 4.79%	Blood pool SUV % change = 6.56%	Brain SUV % change = 8.62%	Muscles SUV % change = 0.66%
MTB % change = 318.95%	R= -0.467 P= <0.001	R= -0.291 P= <0.033	R= -0.417 P=0.002	Non Sig.

Table 2. Comparison between different response groups in 54 lymphoma patients.

In lymphoma cases % of change in:		MTB	Liver SUVmax	Blood pool SUVmax	Brain SUVmax	Muscle SUVmax
Progression VS Regression	Mean difference	2026.826	-17.256	-19.491	-26.786	-6.852
	P value	<0.001	0.001	NS	<0.001	NS
Progression VS Resolution	Mean difference	2033.663	-10.050	-10.770	-34.290	8.882
	P value	<0.001	NS	NS	0.002	NS
Regression VS Resolution	Mean difference	6.837	7.206	8.722	-7.504	15.734
	P value	NS	NS	NS	NS	NS

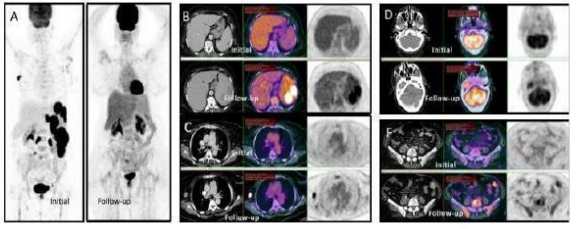

Female patient, 65-year-old with a history of Non-Hodgkin lymphoma, showing marked metabolic regression after chemotherapy treatment.

A. MIP images of initial study (MTB=6020) and at follow-up study (MTB=34) with (% of change = -99.4%).

B. Liver; 3 cm ROI within the right lobe in initial study (SUVmax=3.1) and at follow-up study (SUVmax=3.7) with (% of change=19.3%).

C. Mediastinal Blood Pool; 1.2 cm ROI within descending aorta in initial study (SUVmax=2.1) and at follow-up study (SUVmax=2.8) with (% of change=33.3%).

D. Brain; 1.2 cm ROI at the right cerebellum in initial study (SUVmax=7.2) and at follow-up study (SUVmax=9) with (% of change=25%).

F. Muscles; 1.2 cm ROI within right psoas major muscle in initial study (SUVmax=1) and at follow-up study (SUVmax=1) with (% of change=0%).

A Novel Mitochondrial-Targeted [^{18}F]F-AraG Positron Emission Tomography (PET) Biomarker for Early Diagnosis and Monitoring of Cardiotoxicity

UCSF Department of Radiology and Biomedical Imaging

Uttam M. Shrestha, PhD[1], Jelena Levi, PhD[2], Heedon Chae, *PhD[2],* Joseph Blecha, *PhD[1],* Henry VanBrocklin, *PhD[1],* John Sunwoo, MD[3], A. Dimitrios Colevas, MD[3], *Youngho Seo, PhD[1]*

[1]*Department of Radiology and Biomedical Imaging, University of California, San Francisco, CA, USA*
[2]*CellSight Technologies, Inc., San Francisco, CA, USA*
[3]*Stanford School of Medicine, Stanford, CA, USA.*

CELLSIGHT TECHNOLOGIES Imaging Immunotherapies

PURPOSE & BACKGROUND

Cardiotoxicity caused by anthracyclines, and more selective, targeted therapies, such as kinase inhibitors and immune checkpoint inhibitors (ICIs) may give rise to irreversible myocardial injury with significant reduction of left ventricular ejection fraction. The development of noninvasive imaging methods for early detection and monitoring of cardiotoxicity is pivotal for the better management of cardiac complications associated with cancer therapy. In this retrospective study, we report the preliminary results on cardiac imaging using a novel mitochondrial-targeted [^{18}F]F-AraG PET in cancer patients undergoing immunotherapy.

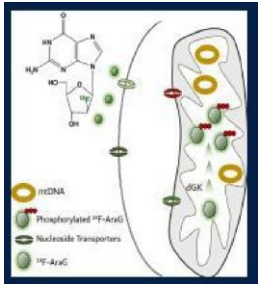

Fig. 1: [^{18}F]F-AraG, an imaging agent to visualize immune response. [^{18}F]F-AraG enters T cells via nucleoside transporters and is trapped intracellularly through phosphorylation primarily by deoxyguanosine kinase (dGK). The key to [^{18}F]F-AraG's ability to visualize activated T cells lies in its association with mitochondrial biogenesis mediated through the action of mitochondrial dGK. Non-invasive tracking of activated T cells may allow assessment of proper or aberrant immune function and enable timely treatment and interventions.

Fig. 2 A: Possible mechanism of ICI cardiotoxicity. The therapeutic mechanism of ICI is based on targeting immunosuppressive checkpoints, such as cytotoxic T lymphocyte-associated protein-4 (CTLA-4), programmed cell death protein-1 (PD-1), and PD-1 ligand (PD-L1). While activating anti-tumor T cells, ICI can produce a series of autoimmune toxicities resulting in the occurrence of immune-related adverse events (irAEs). The exaggerated immune response against the cancer cell antigens can also hinder the proper function of the myocytes as they share the same antigens (PD-L1 also exists in cardiomyocytes) with cancer cells resulting T cell-mediated cytotoxicity, cardiomyopathy and coronary artery disease (CAD). The infiltration of T cells into the injured myocardial tissue may also lead to ICI-related myocarditis, with very high mortality rate.

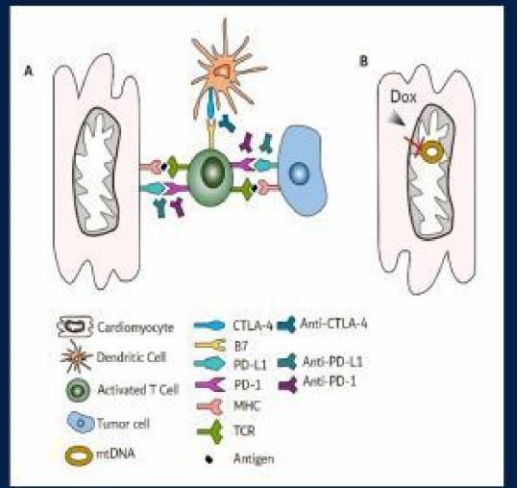

Fig. 2 B: Doxorubicin-induced cardiotoxicity. Doxorubicin-induced cardiotoxicity is the result of the direct interference in the mitochondrial process in the cardiomyocytes. Doxorubicin readily enters mitochondria and interferes with mtDNA synthesis. Following phosphorylation by dGK, [18F]F-AraG can be incorporated into mtDNA and thus report on the status of its synthesis. It also indirectly affects cellular process through nuclear-mediated effect such as inhibition of topoisomerase 2β in cardiomyocytes.

A Novel Mitochondrial-Targeted [^{18}F]F-AraG Positron Emission Tomography (PET) Biomarker for Early Diagnosis and Monitoring of Cardiotoxicity

UCSF Department of Radiology and Biomedical Imaging

Uttam M. Shrestha, PhD[1], Jelena Levi, PhD[2], Heedon Chae, *PhD[2],* Joseph Blecha, *PhD[1],* Henry VanBrocklin, *PhD[1],* John Sunwoo, MD[3], A. Dimitrios Colevas, MD[3], *Youngho Seo, PhD[1]*

[1]Department of Radiology and Biomedical Imaging, University of California, San Francisco, CA, USA
[2]CellSight Technologies, Inc., San Francisco, CA, USA
[3]Stanford School of Medicine, Stanford, CA, USA.

CellSight Technologies — Imaging Immunotherapies

METHODS & RESULTS

Healthy controls

Fig. 3: Healthy controls. Six healthy subjects (3F, 3M mean age 45 ± 15 y) participated in the study. Each subject received a bolus injection of [^{18}F]F-AraG (244 to 329 MBq) prior to PET/MR whole-body scans (SIGNA, GE Healthcare). Dixon MRI was also acquired for MR-based attenuation correction implemented in PET reconstruction (TOF-OSEM). (Scale: 0 to 5 SUV).

Pre-ICI therapy

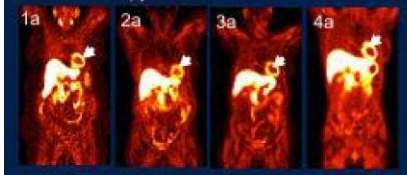

Post-ICI therapy

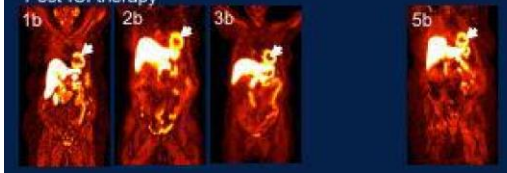

Fig. 4: Pre and post ICI therapy (Cancer). Five head-and-neck non-squamous cancer patients (5F, mean age 71 ± 15 y) undergoing immunotherapy (4 with nivolumab and 1, a combination of docetaxel and cetuximab) were investigated. Out of 5 patients, patients #1,2,3 had paired pre and post therapy of [^{18}F]F-AraG scans while patient #4 had only pre and patient #5 had post therapy F-AraG scans. The whole-body PET data were acquired with PET/CT (3 patients with Siemens Biograph mCT 128 and 2 with GE Discovery MI) each at approximately 60 min after the injection of a single dose (134–324 MBq) of [^{18}F]F-AraG . Post therapy scans were performed 3 to 4 weeks after the first course of ICI therapy. CT-based attenuation correction was implemented in PET reconstruction (Scale: 0-10 SUV).

A Novel Mitochondrial-Targeted [^{18}F]F-AraG Positron Emission Tomography (PET) Biomarker for Early Diagnosis and Monitoring of Cardiotoxicity

UCSF Department of Radiology and Biomedical Imaging

Uttam M. Shrestha, PhD[1], Jelena Levi, PhD[2], Heedon Chae, *PhD[2],* Joseph Blecha, *PhD[1],* Henry VanBrocklin, *PhD[1],* John Sunwoo, MD[3], A. Dimitrios Colevas, MD[3], *Youngho Seo, PhD[1]*

[1]Department of Radiology and Biomedical Imaging, University of California, San Francisco, CA, USA
[2]CellSight Technologies, Inc., San Francisco, CA, USA
[3]Stanford School of Medicine, Stanford, CA, USA.

CellSight Technologies — Imaging Immunotherapies

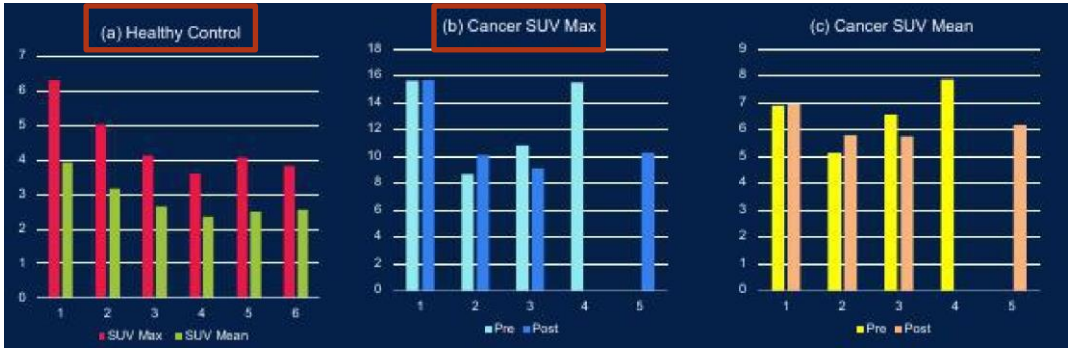

Fig. : [^{18}F]F-AraG myocardial uptake. The extent of uptake of [^{18}F]F-AraG in the myocardium was evaluated semi-quantitatively by drawing ROI and calculating the mean standardized uptake value (SUV) of the total left ventricle myocardium. Healthy controls (HC) (Fig. 4) represent non-cancer patients with no known or documented heart diseases. The cancer patients (Fig. 5), who have been previously treated with chemotherapy, demonstrated elevated level of of [^{18}F]F-AraG uptake in the myocardium both in pre and post ICI therapies (b, c) compared to HC (a). Higher myocardial uptake of [^{18}F]F-AraG in cancer patients may indicate potential mitochondrial dysfunction in the myocytes and/or T cell infiltration.

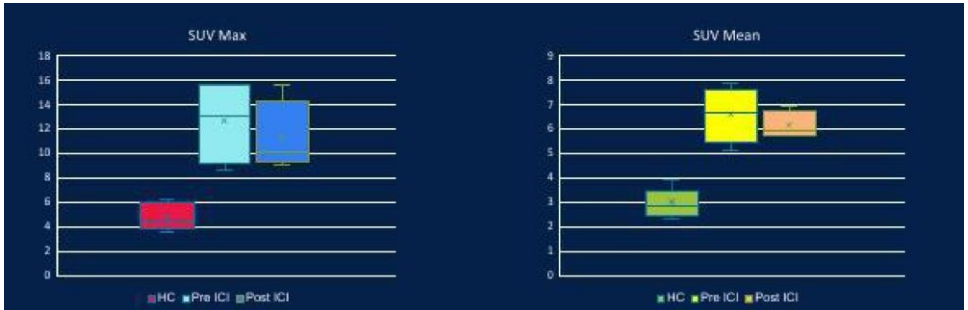

Fig. 6: [^{18}F]F-AraG comparison. The difference in the mean SUV between healthy controls and cancer patients are highly significant (SUVmean = 3.02 ± 0.73 vs. 6.6 ± 1.13 (pre-ICI) and 6.16 ± 0.55 (post-ICI) , p<0.001). However, the pre and post ICI therapy groups did not show any significant difference (p=0.56). The observed higher signal in the cancer patients may be due to cardiotoxicity of the previous cancer therapy or cancer itself, as it is a systemic disease that could be affecting the myocardial function.

Fig. 7: Representative trans-axial images of sex-, age- and BMI-matched cancer patient (a) and healthy subject (b). The observed difference in age (71 ± 15 y vs. 45 ± 15 y) and BMI (28 ± 12 kg/m2 vs. 25 ± 5 kg/m2) between cancer and healthy controls might have contributed the difference in SUVs. However, the age- and BMI-matched (F, 51y, 18kg/m2) and (F, 55y, 19 kg/m2)) individuals have also shown the significant difference in SUVs between cancer patients and healthy controls. (mean SUV = 10.03 vs. 3.03).

SUVs pre-traitement ≠ SUVs contrôles
Prendre des pts à baseline

A Novel Mitochondrial-Targeted [18F]F-AraG Positron Emission Tomography (PET) Biomarker for Early Diagnosis and Monitoring of Cardiotoxicity

UCSF Department of Radiology and Biomedical Imaging

Uttam M. Shrestha, PhD[1], Jelena Levi, PhD[2], Heedon Chae, *PhD[2],* Joseph Blecha, *PhD[1],* Henry VanBrocklin, *PhD[1],* John Sunwoo, MD[3], A. Dimitrios Colevas, MD[3], *Youngho Seo, PhD[1]*

[1]Department of Radiology and Biomedical Imaging, University of California, San Francisco, CA, USA
[2]CellSight Technologies, Inc., San Francisco, CA, USA
[3]Stanford School of Medicine, Stanford, CA, USA.

CellSight Technologies — Imaging Immunotherapies

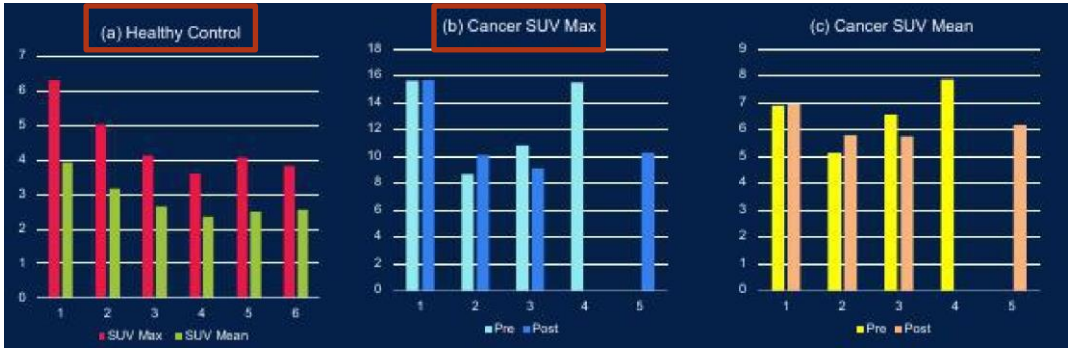

Fig. : [18F]F-AraG myocardial uptake. The extent of uptake of [18F]F-AraG in the myocardium was evaluated semi-quantitatively by drawing ROI and calculating the mean standardized uptake value (SUV) of the total left ventricle myocardium. Healthy controls (HC) (Fig. 4) represent non-cancer patients with no known or documented heart diseases. The cancer patients (Fig. 5), who have been previously treated with chemotherapy, demonstrated elevated level of of [18F]F-AraG uptake in the myocardium both in pre and post ICI therapies (b, c) compared to HC (a). Higher myocardial uptake of [18F]F-AraG in cancer patients may indicate potential mitochondrial dysfunction in the myocytes and/or T cell infiltration.

CONCLUSIONS

Our preliminary results show that the noninvasive detection of myocardial dysfunction in patients undergoing cancer therapies is feasible using [18F]F-AraG PET. This imaging method may overcome the inability of currently used methods such as echocardiography to detect subclinical cardiac involvement in cancer therapy for better management of possible cardiac complications. Further study is needed to evaluate whether T cell infiltration or damage to mitochondria-rich myocytes alone is responsible for the the underlying mechanism of cardiotoxicity in cancer therapy. Moreover, cancer itself is a systemic disease and could affect the myocardial function.

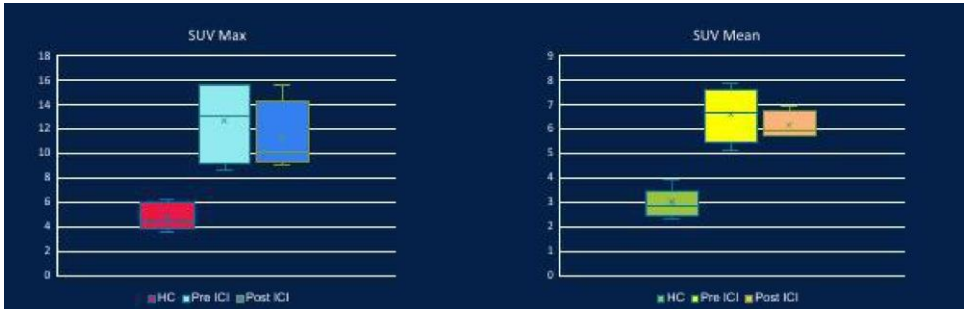

Fig. 6: [18F]F-AraG comparison. The difference in the mean SUV between healthy controls and cancer patients are highly significant (SUVmean = 3.02 ± 0.73 vs. 6.6 ± 1.13 (pre-ICI) and 6.16 ± 0.55 (post-ICI) , p<0.001). However, the pre and post ICI therapy groups did not show any significant difference (p=0.56). The observed higher signal in the cancer patients may be due to cardiotoxicity of the previous cancer therapy or cancer itself, as it is a systemic disease that could be affecting the myocardial function.

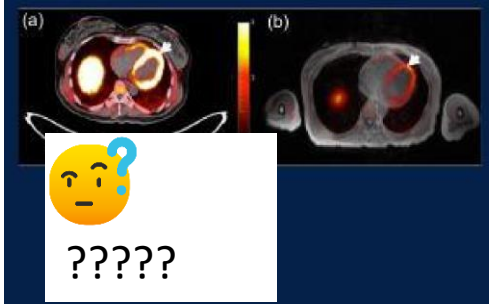

Fig. 7: Representative trans-axial images of sex-, age- and BMI-matched cancer patient (a) and healthy subject (b). The observed difference in age (71 ± 15 y vs. 45 ± 15 y) and BMI (28 ± 12 kg/m2 vs. 25 ± 5 kg/m2) between cancer and healthy controls might have contributed the difference in SUVs. However, the age- and BMI-matched (F, 51y, 18kg/m2) and (F, 55y, 19 kg/m2)) individuals have also shown the significant difference in SUVs between cancer patients and healthy controls. (mean SUV = 10.03 vs. 3.03).

A Novel Mitochondrial-Targeted [^{18}F]F-AraG Positron Emission Tomography (PET) Biomarker for Early Diagnosis and Monitoring of Cardiotoxicity

UCSF Department of Radiology and Biomedical Imaging

Uttam M. Shrestha, PhD[1], Jelena Levi, PhD[2], Heedon Chae, *PhD[2],* Joseph Blecha, *PhD[1],* Henry VanBrocklin, *PhD[1],* John Sunwoo, MD[3], A. Dimitrios Colevas, MD[3], *Youngho Seo, PhD[1]*

[1]Department of Radiology and Biomedical Imaging, University of California, San Francisco, CA, USA
[2]CellSight Technologies, Inc., San Francisco, CA, USA
[3]Stanford School of Medicine, Stanford, CA, USA.

CellSight Technologies — Imaging Immunotherapies

PURPOSE & BACKGROUND

Cardiotoxicity caused by anthracyclines, and more selective, targeted therapies, such as kinase inhibitors and immune checkpoint inhibitors (ICIs) may give rise to irreversible myocardial injury with significant reduction of left ventricular ejection fraction. The development of noninvasive imaging methods for early detection and monitoring of cardiotoxicity is pivotal for the better management of cardiac complications associated with cancer therapy. In this retrospective study, we report the preliminary results on cardiac imaging using a novel mitochondrial-targeted [^{18}F]F-AraG PET in cancer patients undergoing immunotherapy.

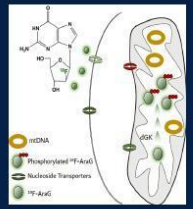

Fig. 1: [^{18}F]F-AraG, an imaging agent to visualize immune response. [^{18}F]F-AraG enters T cells via nucleoside transporters and is trapped intracellularly through phosphorylation primarily by deoxyguanosine kinase (dGK). The key to [^{18}F]F-AraG's ability to visualize activated T cells lies in its association with mitochondrial biogenesis mediated through the action of mitochondrial dGK. Non-invasive tracking of activated T cells may allow assessment of proper or aberrant immune function and enable timely treatment and interventions.

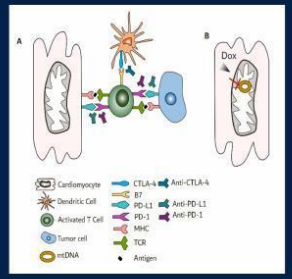

Fig. 2 A: Possible mechanism of ICI cardiotoxicity. The therapeutic mechanism of ICI is based on targeting immunosuppressive checkpoints, such as cytotoxic T lymphocyte-associated protein-4 (CTLA-4), programmed cell death protein-1 (PD-1), and PD-1 ligand (PD-L1). While activating anti-tumor T cells, ICI can produce a series of autoimmune toxicities resulting in the occurrence of immune-related adverse events (irAEs). The exaggerated immune response against the cancer cell antigens can also hinder the proper function of the myocytes as they share the same antigens (PD-L1 also exists in cardiomyocytes) with cancer cells resulting T cell-mediated cytotoxicity, cardiomyopathy and coronary artery disease (CAD). The infiltration of T cells into the injured myocardial tissue may also lead to ICI-related myocarditis, with very high mortality rate.

Fig. 2 B: Doxorubicin-induced cardiotoxicity. Doxorubicin-induced cardiotoxicity is the result of the direct interference in the mitochondrial process in the cardiomyocytes. Doxorubicin readily enters mitochondria and interferes with mtDNA synthesis. Following phosphorylation by dGK, [18F]F-AraG can be incorporated into mtDNA and thus report on the status of its synthesis. It also indirectly affects cellular process through nuclear-mediated effect such as inhibition of topoisomerase 2β in cardiomyocytes.

METHODS & RESULTS

Fig. 3: Healthy controls. Six healthy subjects (3F, 3M mean age 45 ± 15 y) participated in the study. Each subject received a bolus injection of [^{18}F]F-AraG (244 to 329 MBq) prior to PET/MR whole-body scans (SIGNA, GE Healthcare). Dixon MRI was also acquired for MR-based attenuation correction implemented in PET reconstruction (TOF-OSEM). (Scale: 0 to 5 SUV).

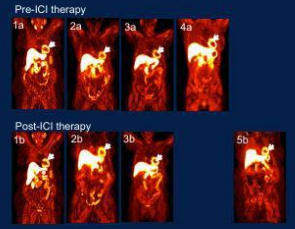

Fig. 4: Pre and post ICI therapy (Cancer). Five head-and-neck non-squamous cancer patients (5F, mean age 71 ± 15 y) undergoing immunotherapy (4 with nivolumab and 1, a combination of docetaxel and cetuximab) were investigated. Out of 5 patients, patients #1,2,3 had paired pre and post therapy of [^{18}F]F-AraG scans while patient #4 had only pre and patient #5 had post therapy F-AraG scans. The whole-body PET data were acquired with PET/CT (3 patients with Siemens Biograph mCT 128 and 2 with GE Discovery MI) each at approximately 60 min after the injection of a single dose (134–324 MBq) of [^{18}F]F-AraG . Post therapy scans were performed 3 to 4 weeks after the first course of ICI therapy. CT-based attenuation correction was implemented in PET reconstruction (Scale: 0-10 SUV).

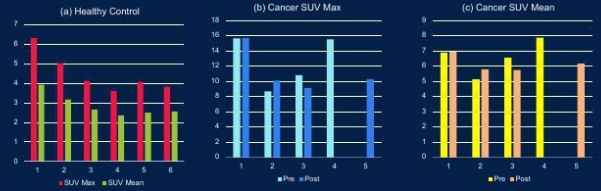

Fig. : [^{18}F]F-AraG myocardial uptake. The extent of uptake of [^{18}F]F-AraG in the myocardium was evaluated semi-quantitatively by drawing ROI and calculating the mean standardized uptake value (SUV) of the total left ventricle myocardium. Healthy controls (HC) (Fig. 4) represent non-cancer patients with no known or documented heart diseases. The cancer patients (Fig. 5), who have been previously treated with chemotherapy, demonstrated elevated level of of [^{18}F]F-AraG uptake in the myocardium both in pre and post ICI therapies (b, c) compared to HC (a). Higher myocardial uptake of [^{18}F]F-AraG in cancer patients may indicate potential mitochondrial dysfunction in the myocytes and/or T cell infiltration.

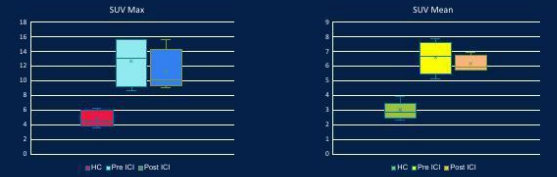

Fig. 6: [^{18}F]F-AraG comparison. The difference in the mean SUV between healthy controls and cancer patients are highly significant (SUVmean = 3.02 ± 0.73 vs. 6.6 ± 1.13 (pre-ICI) and 6.16 ± 0.55 (post-ICI) , p<0.001). However, the pre and post ICI therapy groups did not show any significant difference (p=0.56). The observed higher signal in the cancer patients may be due to cardiotoxicity of the previous cancer therapy or cancer itself, as it is a systemic disease that could be affecting the myocardial function.

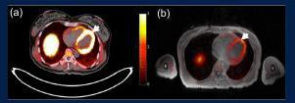

Fig. 7: Representative trans-axial images of sex-, age- and BMI-matched cancer patient (a) and healthy subject (b). The observed difference in age (71 ± 15 y vs. 45 ± 15 y) and BMI (28 ± 12 kg/m2 vs. 25 ± 5 kg/m2) between cancer and healthy controls might have contributed the difference in SUVs. However, the age- and BMI-matched (F, 51y, 18kg/m2) and (F, 55y, 19 kg/m2)) individuals have also shown the significant difference in SUVs between cancer patients and healthy controls. (mean SUV = 10.03 vs. 3.03).

CONCLUSIONS

Our preliminary results show that the noninvasive detection of myocardial dysfunction in patients undergoing cancer therapies is feasible using [^{18}F]F-AraG PET. This imaging method may overcome the inability of currently used methods such as echocardiography to detect subclinical cardiac involvement in cancer therapy for better management of possible cardiac complications. Further study is needed to evaluate whether T cell infiltration or damage to mitochondria-rich myocytes alone is responsible for the the underlying mechanism of cardiotoxicity in cancer therapy. Moreover, cancer itself is a systemic disease and could affect the myocardial function.

References

Levi, Jelena, et al. "Biodistribution of a mitochondrial metabolic tracer,[18F] F-AraG, in healthy volunteers." *Molecular Imaging* 2022 (2022).

Patel, Rushin P., et al. "Cardiotoxicity of immune checkpoint inhibitors." *Current Oncology Reports* 23 (2021).

Levi, Jelena, et al. "18F-AraG PET for CD8 profiling of tumors and assessment of immunomodulation by chemotherapy." *Journal of Nuclear Medicine* 62.6 (2021): 802-807.

Levi, Jelena, et al. "Imaging of activated T cells as an early predictor of immune response to anti-PD-1 therapy." *Cancer research* 79.13 (2019): 3455-3465.

The study was supported in part by the National Institutes of Health under grants R01 **HL160688-01**

UCSF


TORONTO IS
EXCITED TO HOST
SNMMI
SOCIETY OF
NUCLEAR MEDICINE &
MOLECULAR IMAGING

JUNE 8–11, 2024

TORONTO LOOKS FORWARD TO WELCOMING

SNMMI SOCIETY OF NUCLEAR MEDICINE & MOLECULAR IMAGING

METRO TORONTO CONVENTION CENTRE

June 24-27
2023
Chicago, Illinois, USA
SNMMI ANNUAL MEETING
EYE ON THE PATIENT

Debate: Should Deep Learning Replace Radiomics?

Speakers:

Joyita Dutta, PhD, UMass Amherst

Irène Buvat, PhD, Institut Curie

Abhinav Jha, PhD, WashU St. Louis

Eliot Siegel, MD, UMaryland

The team thanks **Fereshteh Yousefirizi**, who could not attend the conference!!

Overview

- Radiomics involves the high-throughput extraction a multitude of features from diagnostic medical images which can then be used to predict treatment response and enable disease prognostication.

- Handcrafted radiomics: Predefined feature representations fed into a ML model that predict an outcome

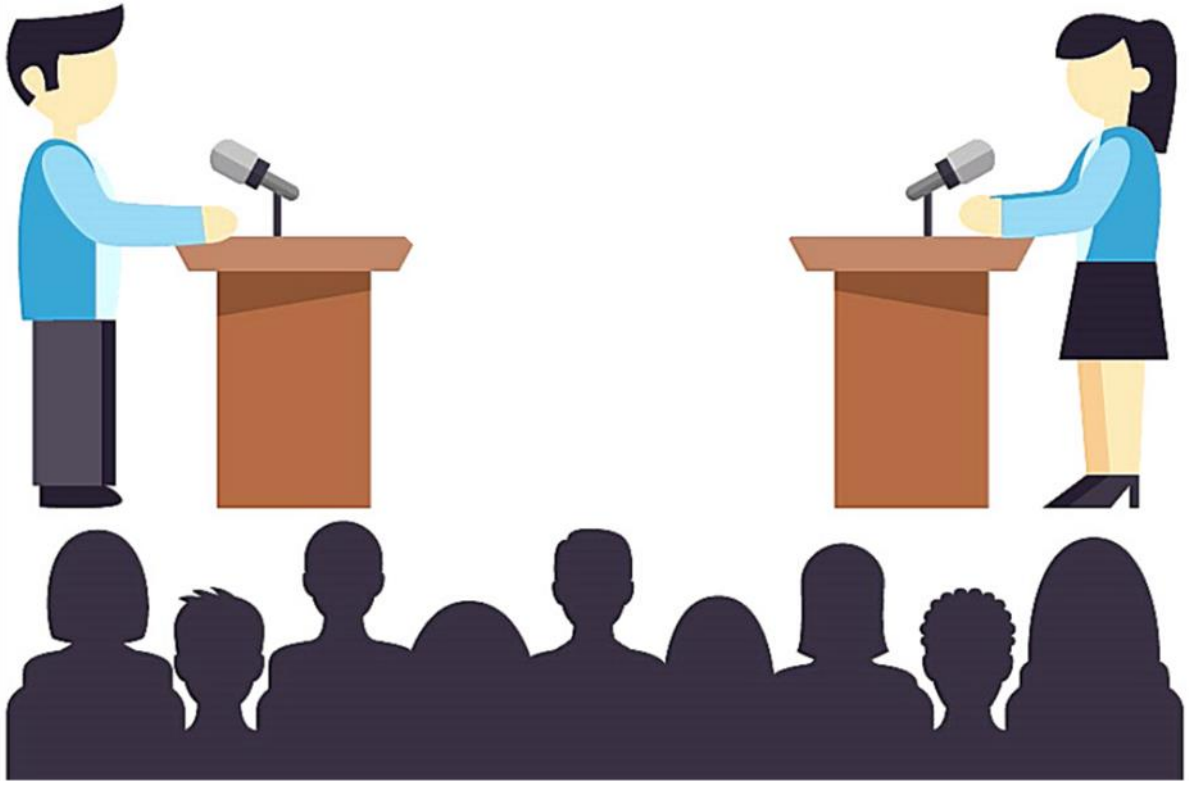

- Deep learning radiomics: Neural network trained to discover new features representations that accurately predict an outcome

Should Deep Learning Replace Radiomics?

Overview

- Radiomics involves the high-throughput extraction a multitude of features from diagnostic medical images which can then be used to predict treatment response and enable disease prognostication.

- Handcrafted radiomics: Predefined feature representations fed into a ML model that predict an outcome

- Deep learning radiomics: Neural network trained to discover new features representations that accurately predict an outcome

Should Deep Learning Replace Radiomics?

Radiomics with Feature Handcrafting

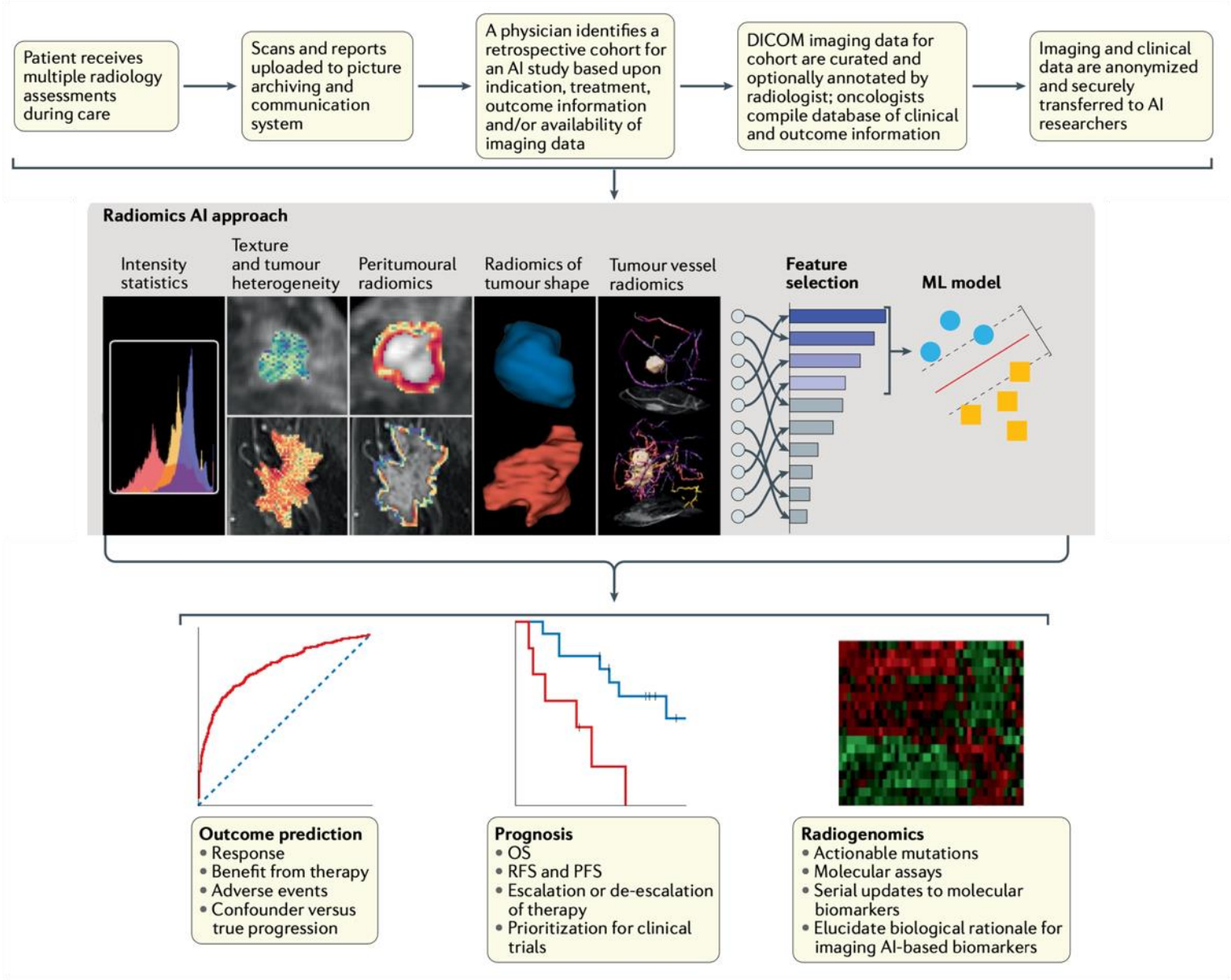

Bera K, *Nat Rev Clin Oncol*. 2022

Radiomics with Deep Learning

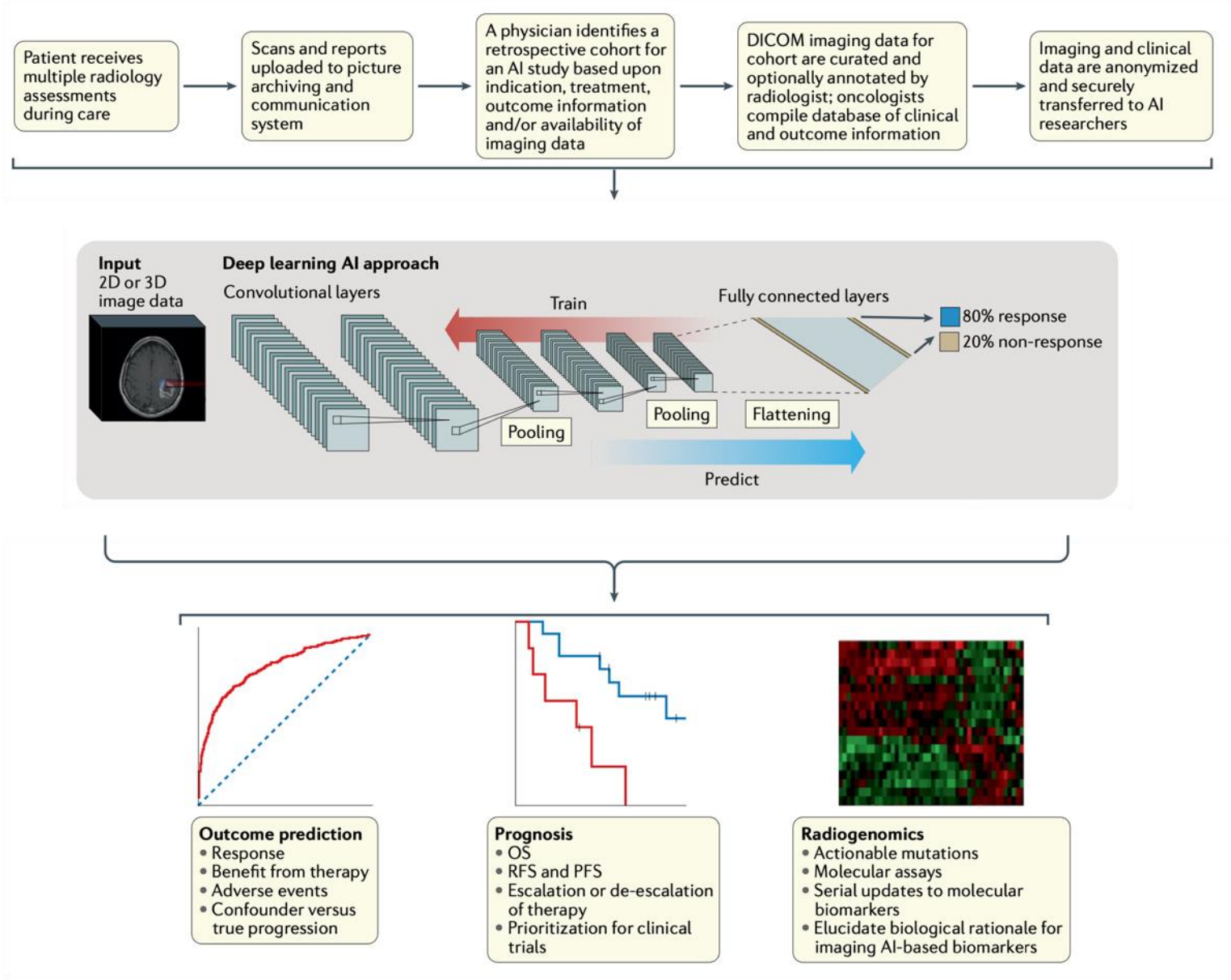

Bera K, *Nat Rev Clin Oncol*. 2022

Should Deep Learning Replace Radiomics?

Interesting to see that none of her examples was from Nuc Med !

Joyita Dutta, PhD
University of Massachusetts Amherst

Argument 1: Higher Accuracies with Deep Features

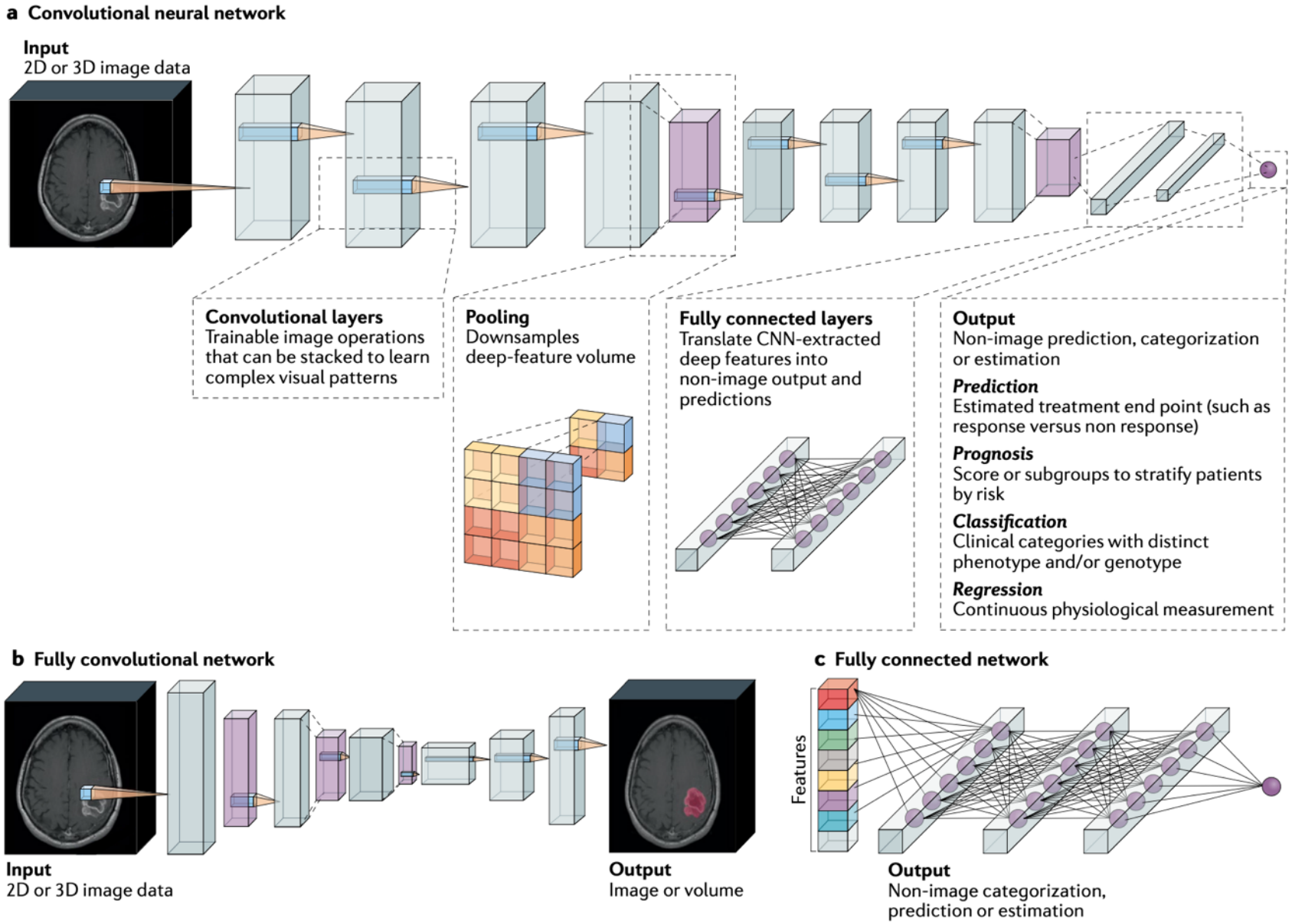

Bera K, *Nat Rev Clin Oncol*. 2022

Argument 1: Examples

- End-to-end approach predicting neoadjuvant chemoradiation treatment (nCRT) response in patients with locally advanced rectal cancer (LARC)
- Handcrafted and DL-based features were extracted from the apparent diffusion coefficient (ADC) map of the DWI using conventional computer-aided diagnosis methods and a pre-trained convolution neural network, respectively.
- Least absolute shrinkage and selection operator (LASSO)-logistic regression models were constructed using extracted features for predicting treatment response.

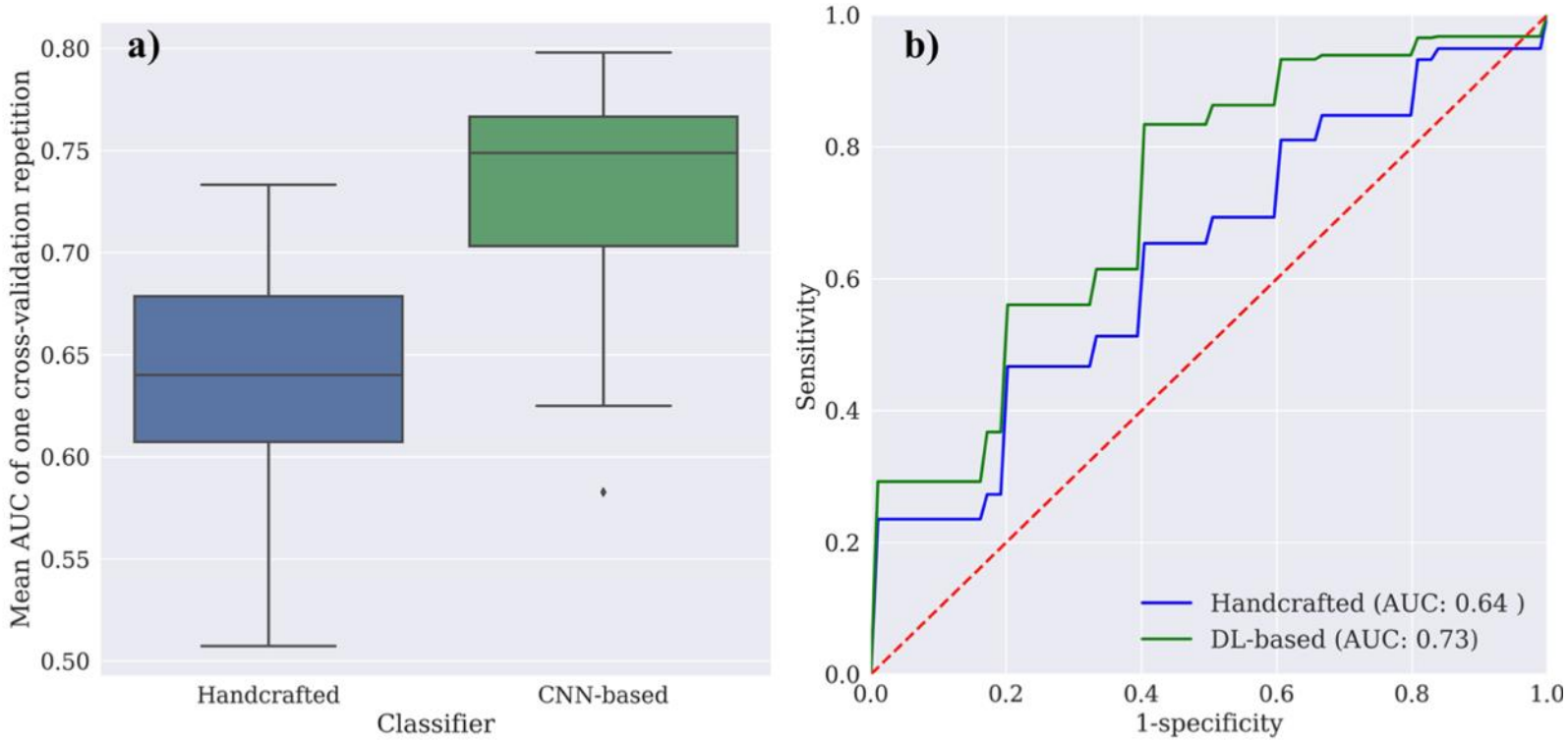

Figure 3. (a) Boxplots of the AUC results of 20 cross-validation repetitions for the handcrafted and DL-based classifiers. The minimum (bottom line), 25th percentile (bottom of the box), median (central line), 75th percentile (top of the box), and maximum (top line) are shown. An outlier is drawn as a diamond sign. (b) The ROC curves for two classifiers in predicting good response versus non-good response using repeated stratified 4-fold cross-validation. AUC results are averaged over 20 × 4 testing sets.

DL-based features extracted from pre-treatment DWIs achieved significantly better classification performance compared with handcrafted features for predicting nCRT response in patients with LARC.

Fu J. et al.. *Physics in Medicine and Biology.* 2020

Argument 1: Examples

- End-to-end approach predicting axillary lymph node (ALN) metastasis using breast ultrasound
- Investigation on the value of both intratumoral and peritumoral regions in ALN metastasis prediction
- 479 breast cancer patients with 2,395 breast ultrasound images
- CNNs were built using DenseNet, and handcrafted radiomics models were built using random forest
- CNNs led to consistently higher SUVs than handcrafted radiomics.

CNN - Training

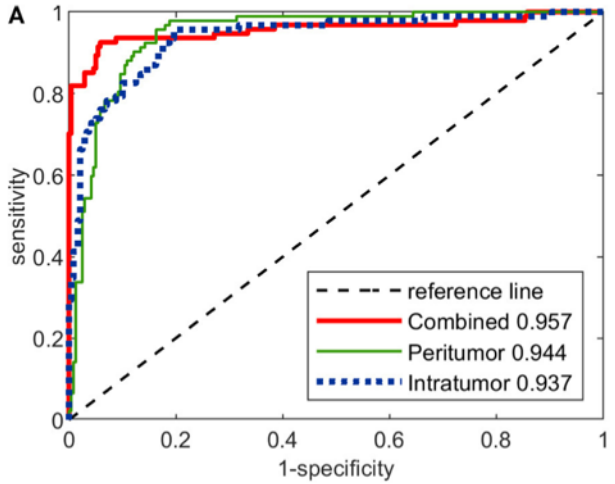

CNN - Validation

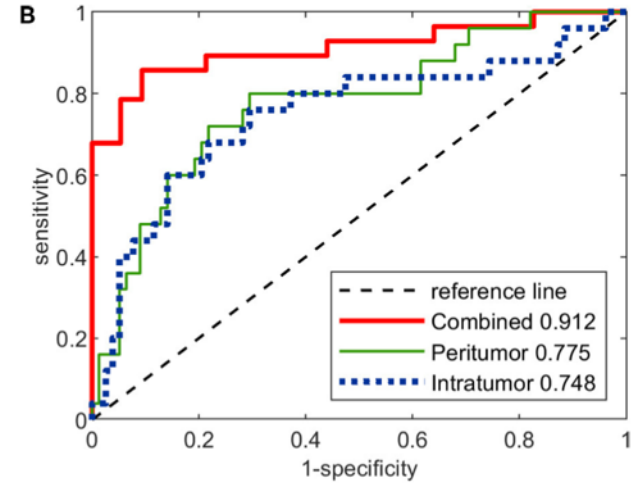

Handcrafted Radiomics - Training

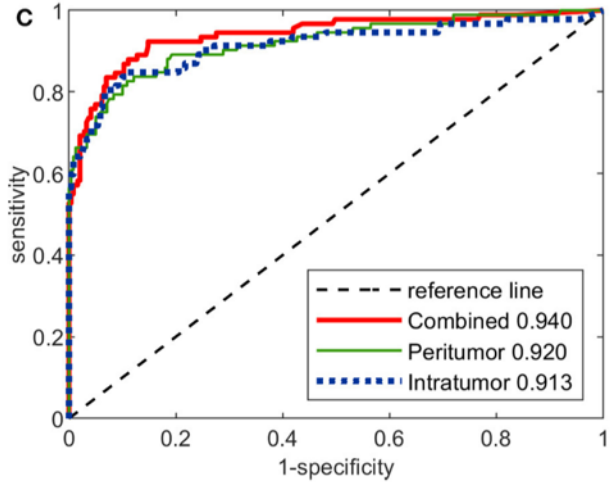

Handcrafted Radiomics - Validation

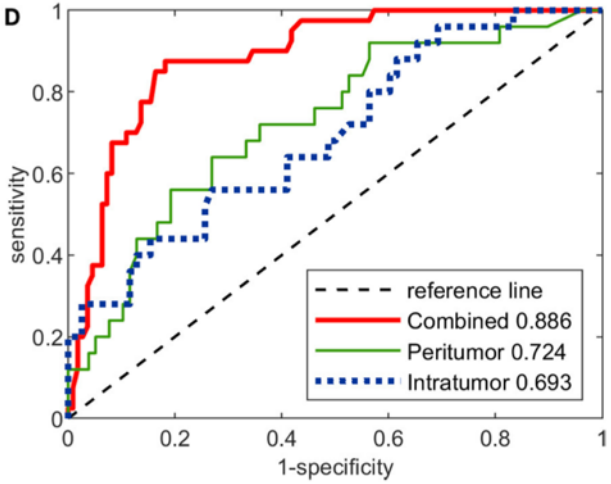

Sun Q. et al. *Frontiers in Oncology.* 2020

Argument 2: Segmentation-Free Analysis

- Neural networks have the potential to automatically identify the parts of the image that are most relevant for the task of interest thus obviating the need for a separate and isolated segmentation step prior to analysis, in contrast to handcrafted features where an area of interest needs to be specified for feature extraction

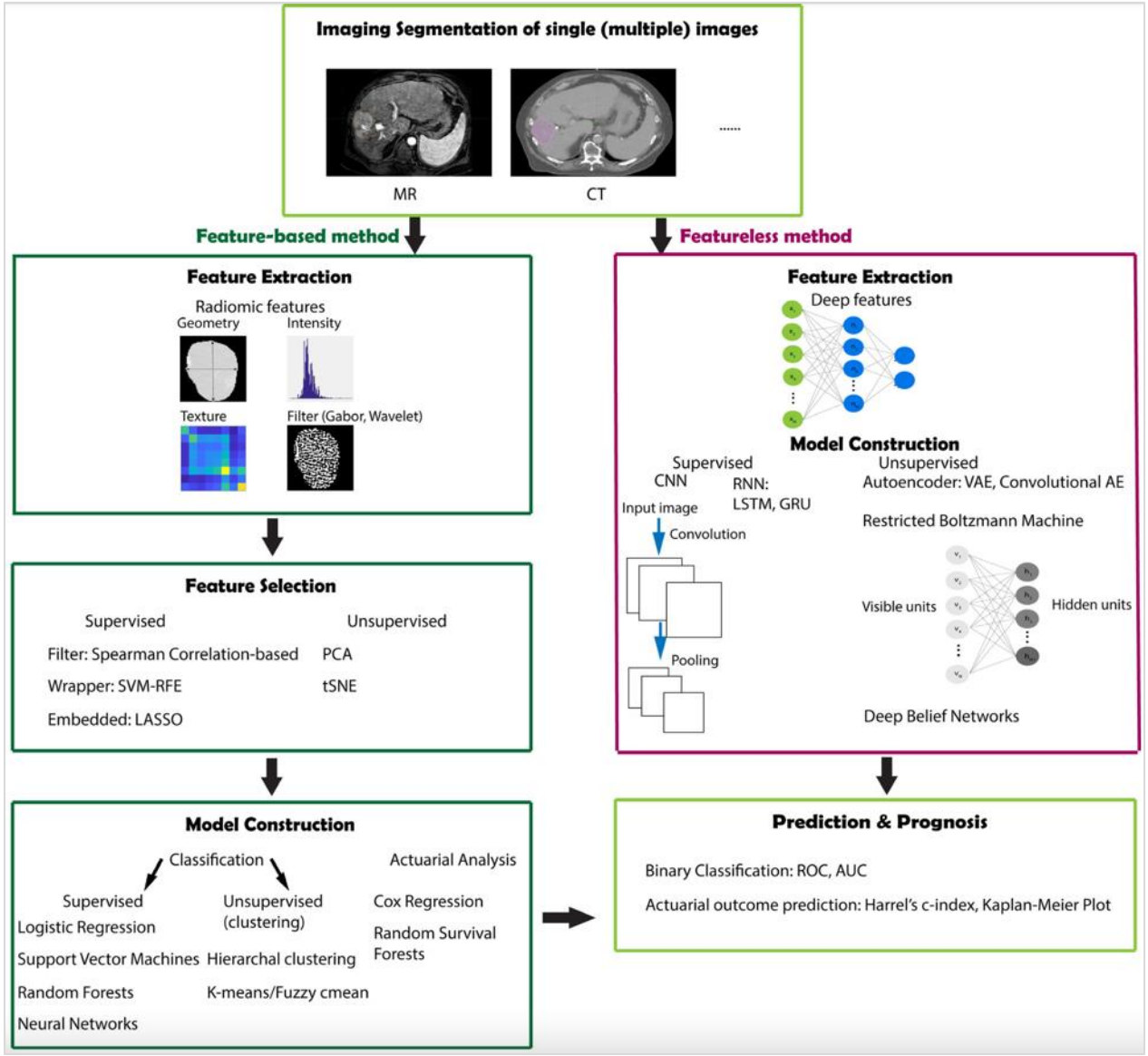

Argument 2: Example

- End-to-end approach for cancer recurrence prediction
- 245 patients with high-grade serous ovarian cancer (HGSOC)
- Goal: To extract prognostic biomarkers from preoperative CT images for non-invasive recurrence prediction in HGSOC.
- 3-year recurrence prediction AUCs: 0.772 and 0.825 in two validation cohorts

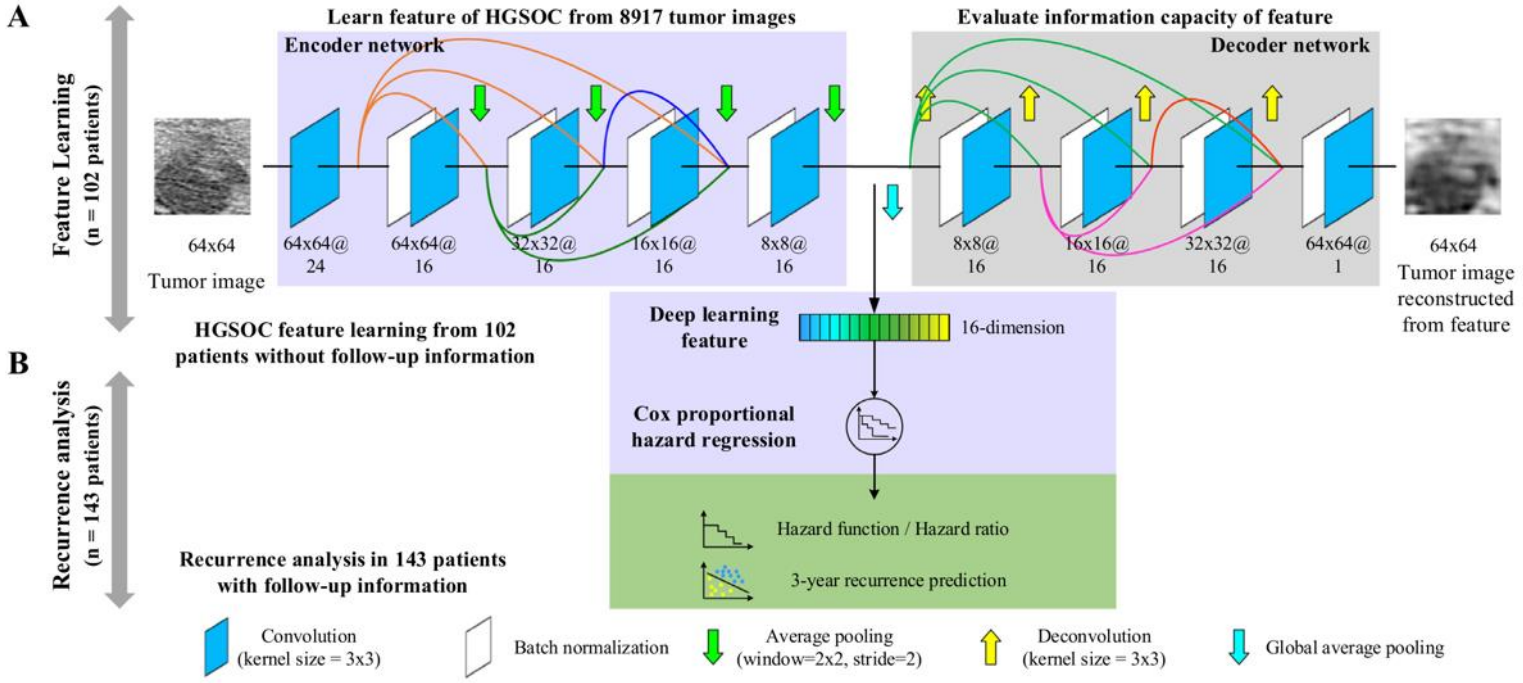

Wang, S. et al.. *Radiother. Oncol.* 2019

Argument 3: AI is Promising for Feature Discovery

- Using handcrafted features alone fails to exploit the potential of AI in discovering novel features
- The discovery of new features could in turn further improve cancer prognostication and treatment decisions for patients by extracting information that is not yet considered in current workflows

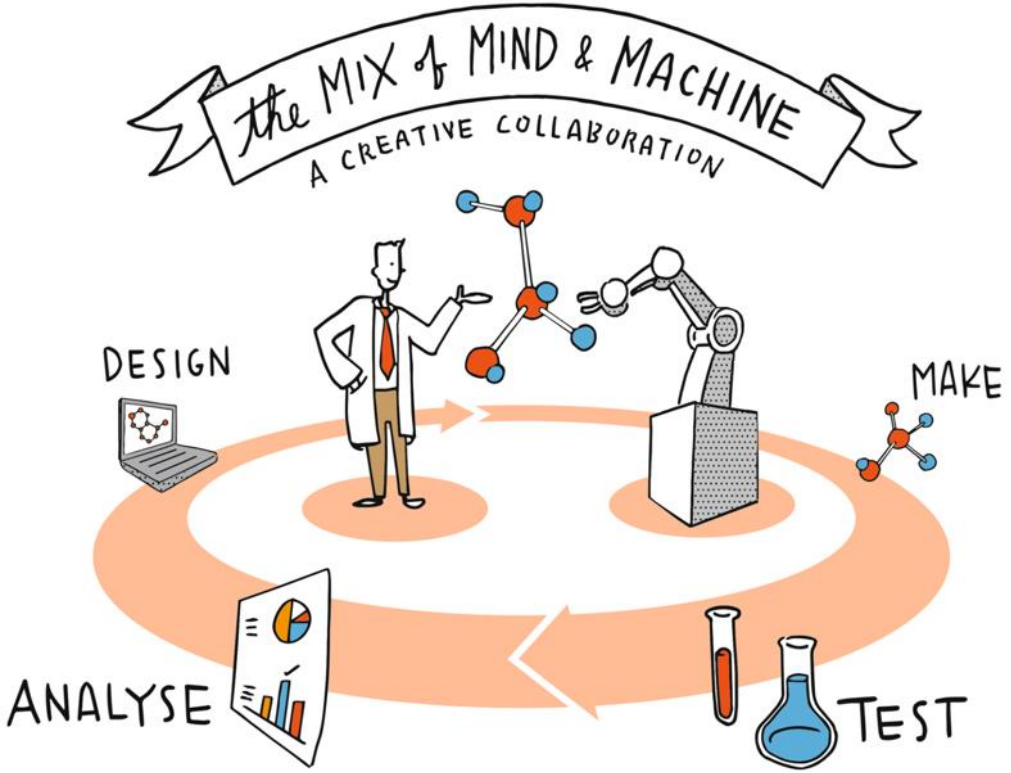

Schneider P, *Nat Rev Drug Discov*. 2020

Argument 3: Examples

- In digital pathology, AI techniques have been used to identify novel features linked to disease outcomes

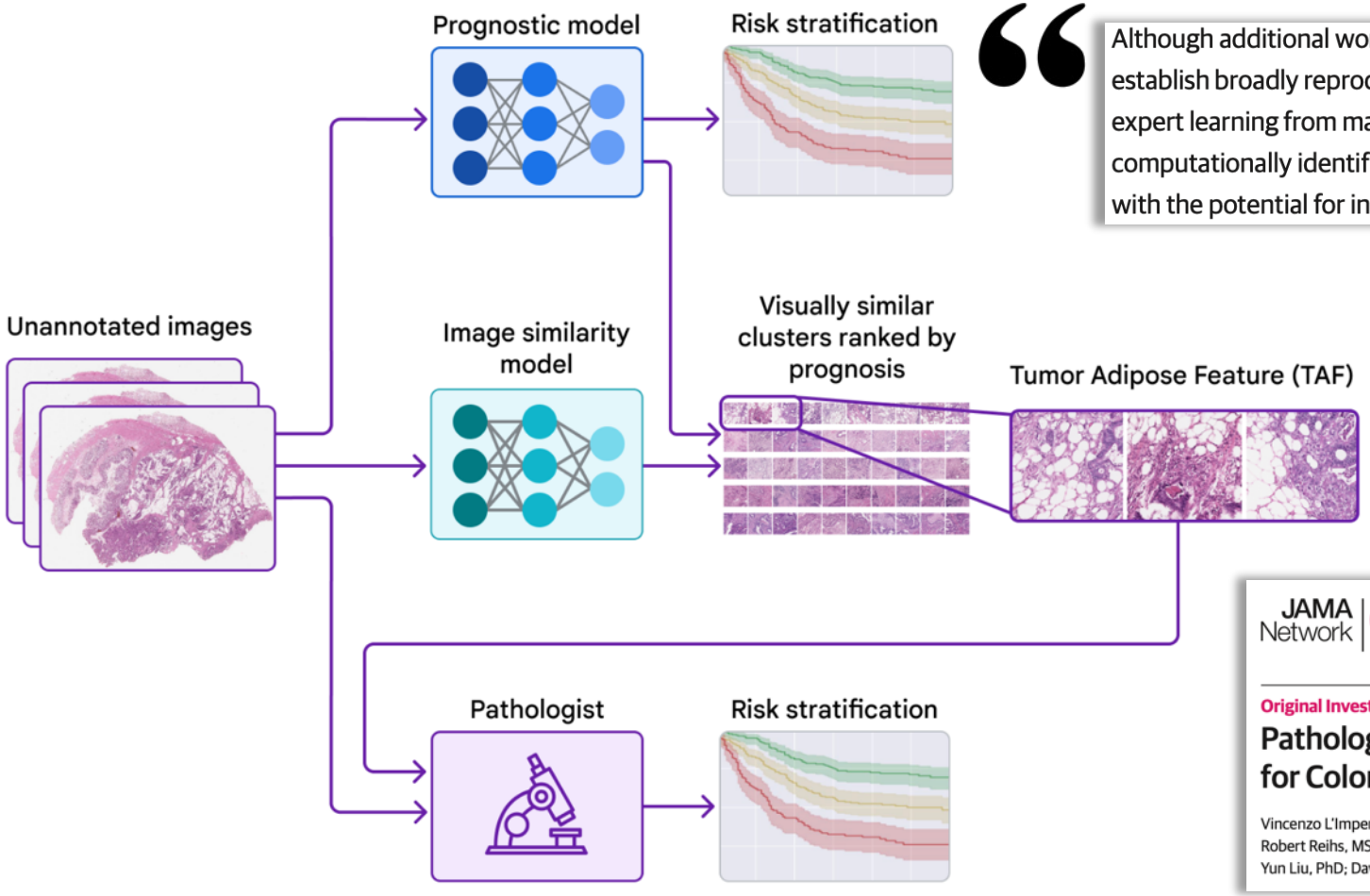

> Although additional work is warranted to understand the biological significance of this feature and to establish broadly reproducible TAF scoring, this work represents the first validation to date of human expert learning from machine learning in pathology. Specifically, this validation demonstrates that a computationally identified histologic feature can represent a human-identifiable, prognostic feature with the potential for integration into pathology practice.

JAMA Network | Open

Original Investigation | Pathology and Laboratory Medicine

Pathologist Validation of a Machine Learning–Derived Feature for Colon Cancer Risk Stratification

Vincenzo L'Imperio, MD; Ellery Wulczyn, MS; Markus Plass, MSc; Heimo Müller, PhD; Nicolò Tamini, MD; Luca Gianotti, MD; Nicola Zucchini, MD; Robert Reihs, MS; Greg S. Corrado, PhD; Dale R. Webster, PhD; Lily H. Peng, MD, PhD; Po-Hsuan Cameron Chen, PhD; Marialuisa Lavitrano, MD, PhD; Yun Liu, PhD; David F. Steiner, MD, PhD; Kurt Zatloukal, MD; Fabio Pagni, MD

L'Imperio V, *JAMA Network Open. 2023*

Argument 3: Examples

- In digital pathology, AI techniques have been used to identify novel features linked to disease outcomes

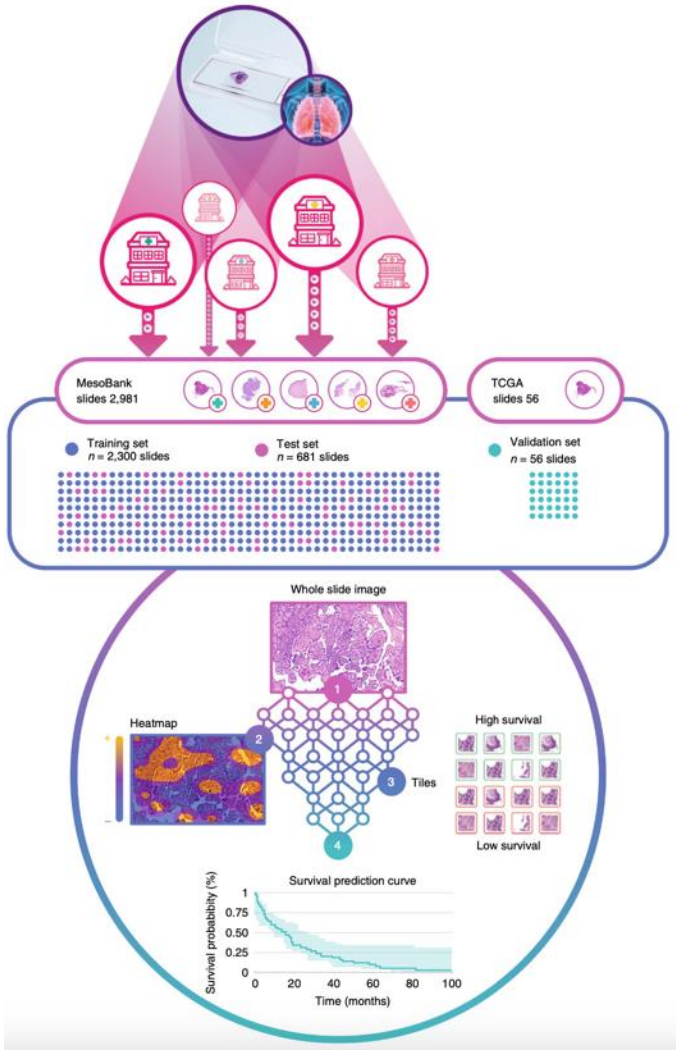

> …unlike classical black-box deep learning methods, MesoNet identified regions contributing to patient outcome prediction. Strikingly, we found that these regions are mainly located in the stroma and are histological features associated with inflammation, cellular diversity and vacuolization. These findings suggest that deep learning models can identify new features predictive of patient survival and potentially lead to new biomarker discoveries.

nature medicine

LETTERS

https://doi.org/10.1038/s41591-019-0583-3

Deep learning-based classification of mesothelioma improves prediction of patient outcome

Pierre Courtiol[1,8], Charles Maussion[1,8], Matahi Moarii[1], Elodie Pronier[1], Samuel Pilcer[1], Meriem Sefta[1], Pierre Manceron[1], Sylvain Toldo[1], Mikhail Zaslavskiy[1], Nolwenn Le Stang[2], Nicolas Girard[3,4], Olivier Elemento[5], Andrew G. Nicholson[6], Jean-Yves Blay[7], Françoise Galateau-Sallé[2,8], Gilles Wainrib[1,8] and Thomas Clozel[1,8]*

Courtial P, *Nature Medicine*, 2019

Should Deep Learning Replace Radiomics?

Irène Buvat, PhD
Institut Curie

Deep learning does not always outperform handcrafted radiomics!

MICCAI2022 Singapore

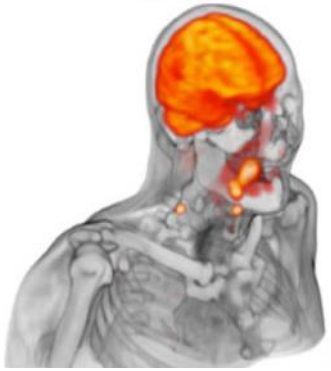

Prediction of the RFS of H&N cancer patients from FDG PET/CT scans
Training: **488 patients**, Blind test: 339 patients

Results: Podium for Task 2

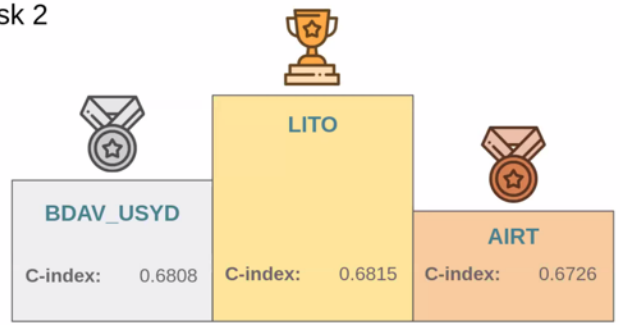

And the winning team:
Louis Rebaud, Thibault Escobar, Fahad Khalid, Kibrom Girum and Irène Buvat "*Head and Neck Tumor and Lymph Node Segmentation and Outcome Prediction from 18F-FDG PET/CT Images: Simplicity is All You Need*" from the Laboratory of Translational Imaging in Oncology in Paris-Saclay, France

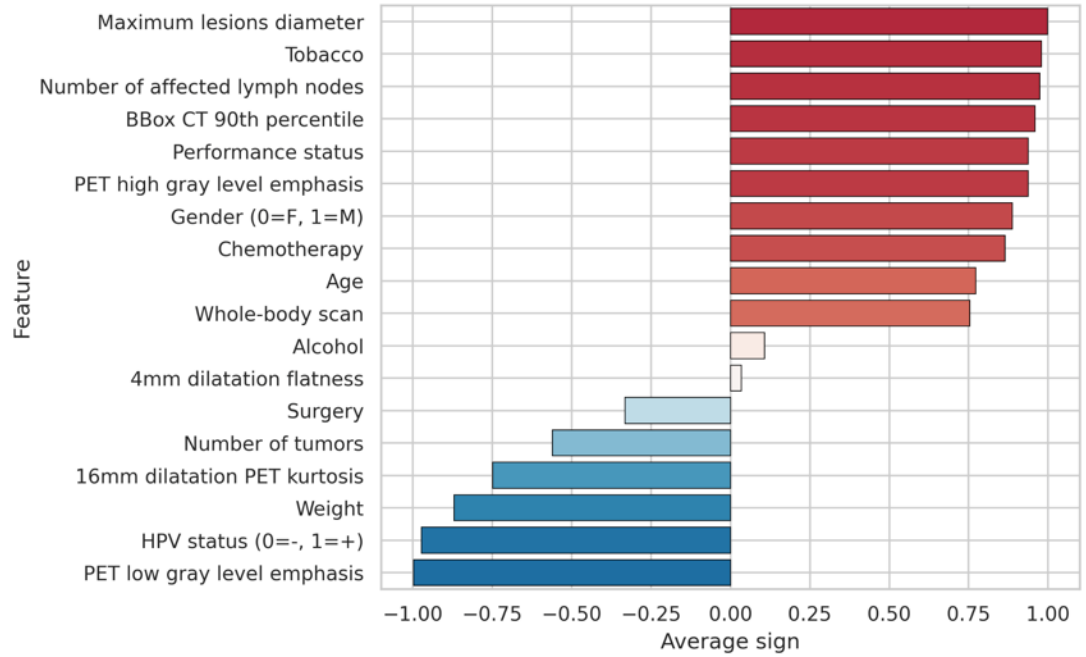

Andrearczyk et al, Lecture Notes in Computer Science, vol 13626, 1-30
Rebaud et al, Lecture Notes in Computer Science, vol 13626, 121-134

Handcrafted features can be biologically informed

What about the spread of the disease?

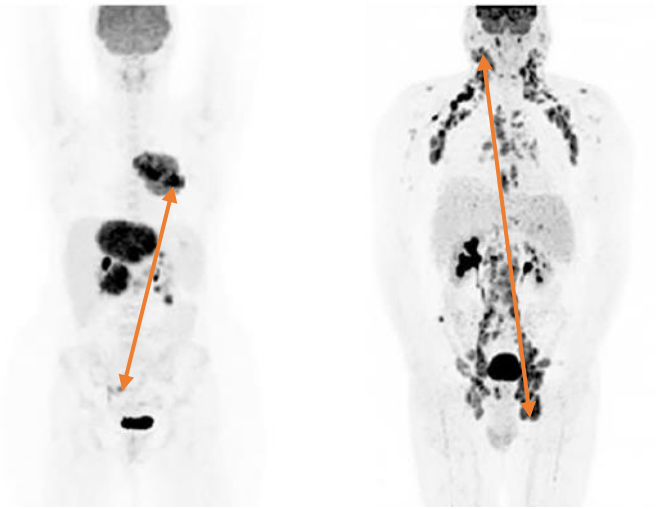

Cottereau et al, J Nucl Med 2021

First Author	N Pts	Lymphoma Variant	Early (I–II)/Advanced (III–IV) Stage Acc Ann Arbor	M:F	Median Age (Range)	Main Results	
Cottereau, A.S. [10]	95	DLBCL	0:95	53:42	46 (18–59)	Dmax was significantly associated with PFS and OS. The combination of MTV and Dmax helped to stratify patients	☑
Weisman, A.J. [14]	100	HL	0:100	60:40	15.8 (5.2–21.4)	Moderate reproducibility in the Dmax measurement between fully automated software and physicians	☑
Cottereau, A.S. [15]	290	DLBCL	26:264	170:120	Nr (60–80)	SDmax was significantly associated with PFS and OS. The combination of MTV and SDmax helped to stratify patients	☑
Zhou, Y. [16]	65	HL	36:29	45:20	29 (8–72)	Dmax was significantly associated with PFS and OS	☑
Cottereau, A.S. [17]	290	DLBCL	26:264	170:120	Nr (60–80)	Comparison of different ways to calculate dissemination features	☑
Vergote, V.K.J. [18]	83	MCL	12:71	62:21	66 (58–72)	Dmax was not associated with prognosis	✗
Durmo, R. [19]	155	HL	77:78	79:76	Nr	Dmax was significantly associated with PFS. Dmax and interim metabolic treatment response helped to stratify patients	☑
Li, H. [20]	126	FL	22:104	63:63	53 (21–76)	Dmax and TLG were significantly associated with PFS	☑
Ceriani, L. [21]	240	DLBCL	104:136	119:121	Nr	SDmax was included in a radiomics model with a prognostic value	☑
Drees, E.E.E. [22]	30	HL	Nr	Nr	36 * (18–66)	Blood-based markers, EV-miRNA, and sTARC were moderately related to dissemination features	☑
Driessen, J. [23]	105	HL	Nr	47:58	30 (13–66)	Good reproducibility of Dmax between 6 different segmentation methods	☑
Eertink, J.J. [24]	317	DLBCL	51:266	161:156	65 (23–80)	$Dmax_{bulk}$ was one of the best predictors of treatment outcome	☑
Eertink, J.J. [25]	296	DLBCL	48:248	152:144	65 (55–72)	Dissemination features were the best predictors of progression	☑
Girum, K.B. [26]	382	DLBCL	Nr	207:175	62.1 * (34–73)	Dmax was significantly associated with PFS and OS. The combination of MTV and Dmax helped to stratify patients	☑
Gong, H. [27]	81	AITL	5:76	53:28	63	Dmax was significantly associated with PFS and OS. The combination of MTV and Dmax helped to stratify patients	☑
Jo, J.H. [28]	63	DLBCL	26:39	28:35	57.3 * (21–87)	Dmax and end-of-treatment metabolic treatment response were significantly associated with TTP	☑
Xie, Y. [29]	95	PTCL	10:85	59:46	64 (16–84)	Dmax and bone marrow biopsy were significantly associated with PFS and OS	☑
Eertink, J.J. [30]	323	DLBCL	77:246	185:138	63 (53–71)	Baseline radiomics features were significantly associated with PFS	☑

Albano et al, Cancers 2023

Handcrafted features can be biologically informed

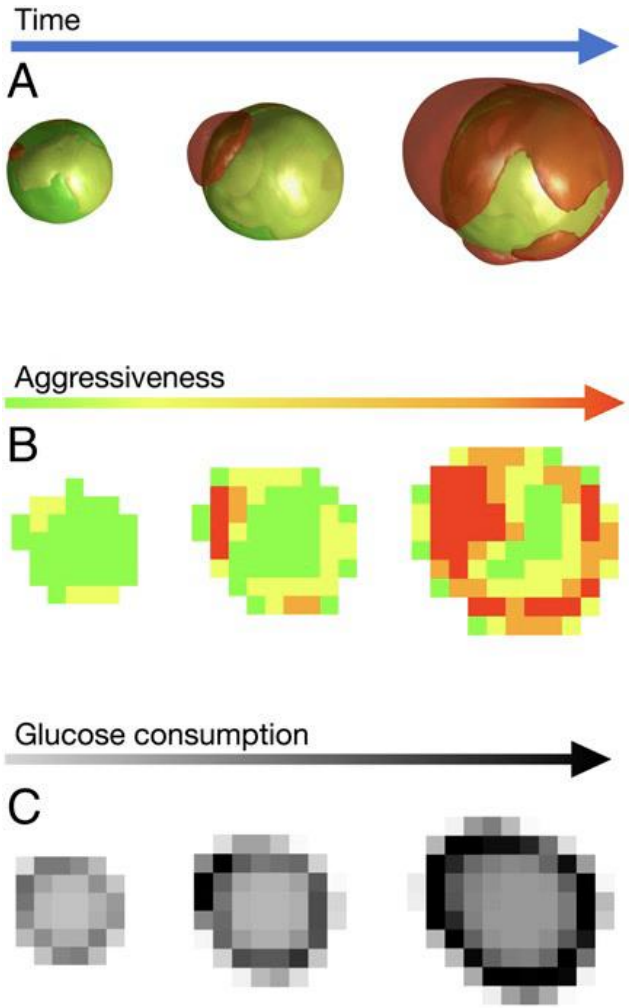

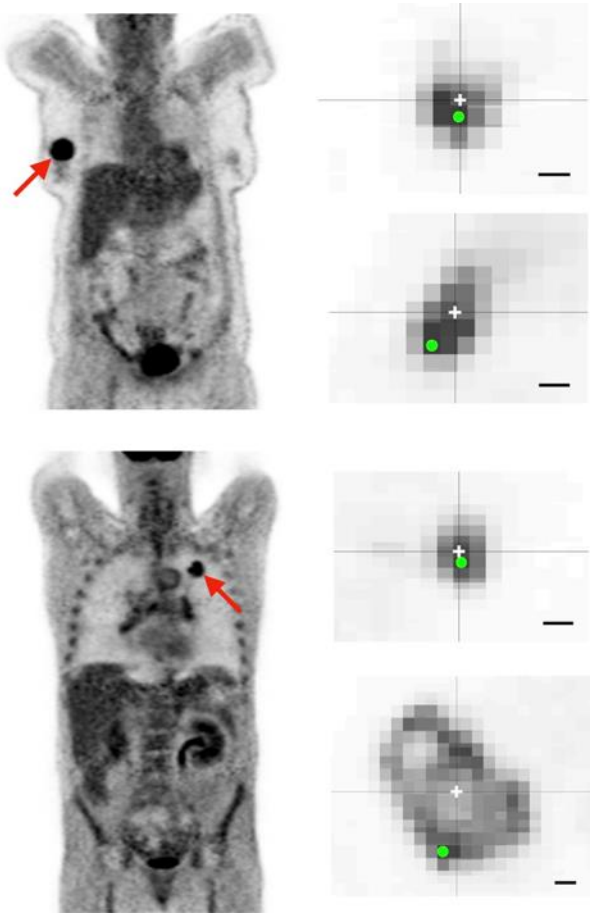

Jimenez-Sanchez et al, PNAS 2021

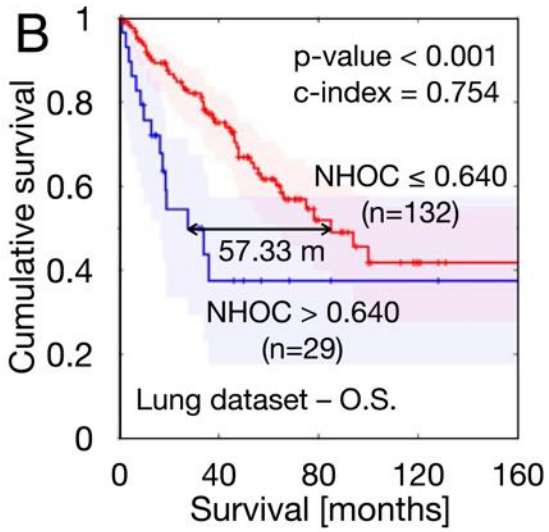

Jimenez-Sanchez et al, PNAS 2021

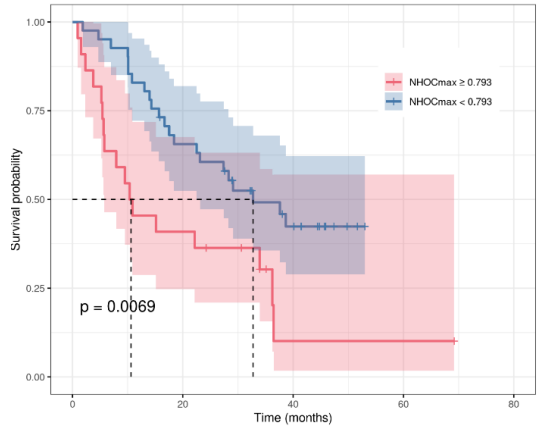

Hovhannisyan et al, SNMMI 2023

Beyond features, radiomic models can generalize well

Prediction of relapse location after re-irradiation of H&N cancer patients from FDG PET/CT scans

Original model designed on a cohort from Paris

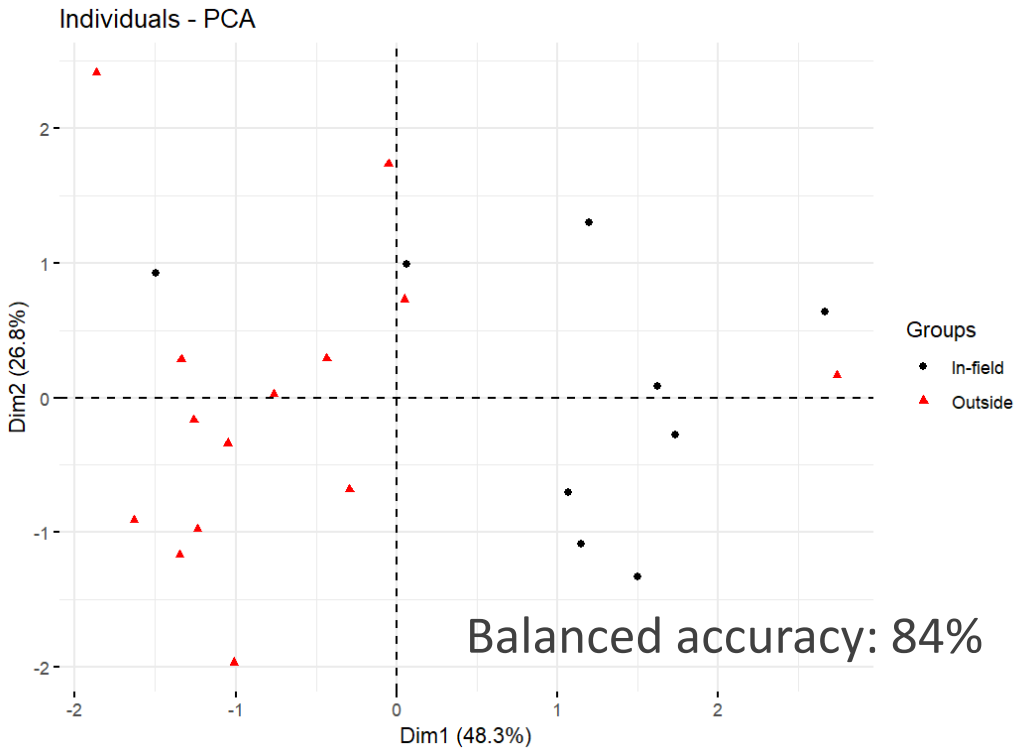

Balanced accuracy: 84%

Beddok et al, Eur J Nucl Med Mol Imaging 2023

Patients from Boston are well classified using exactly the same model

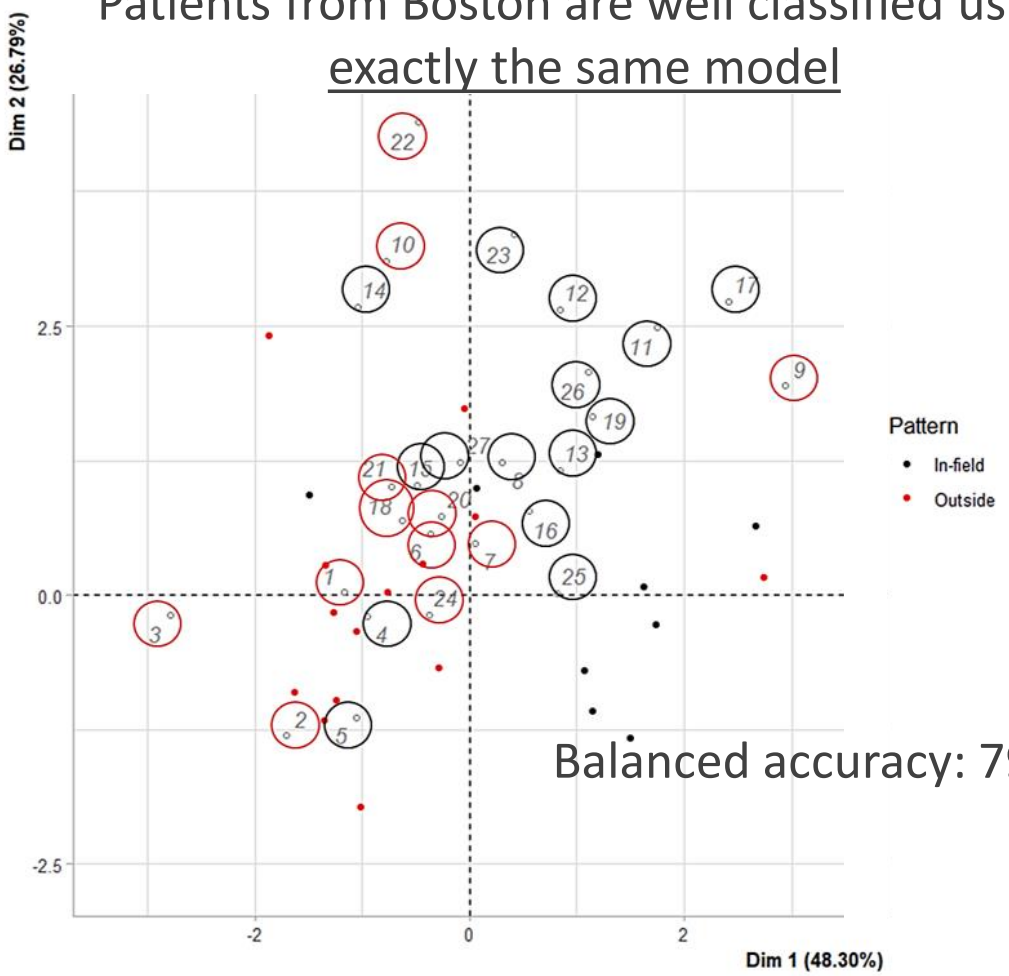

Balanced accuracy: 79%

Beddok et al, submitted

Handcrafted features are easier to standardize

IBSI
image biomarker standardisation initiative

ORIGINAL RESEARCH · COMPUTER APPLICATIONS

Radiology

The Image Biomarker Standardization Initiative:
Standardized Quantitative Radiomics for High-Throughput Image-based Phenotyping

Alex Zwanenburg, PhD • Martin Vallières, PhD* • Mahmoud A. Abdalah, PhD • Hugo J. W. L. Aerts, PhD • Vincent Andrearczyk, PhD • Aditya Apte, PhD • Saeed Ashrafinia, PhD • Spyridon Bakas, PhD • Roelof J. Beukinga, PhD • Ronald Boellaard, PhD • Marta Bogowicz, PhD • Luca Boldrini, PhD • Irène Buvat, PhD • Gary J. R. Cook, PhD • Christos Davatzikos, PhD • Adrien Depeursinge, PhD • Marie-Charlotte Desseroit, PhD • Nicola Dinapoli, PhD • Cuong Viet Dinh, PhD • Sebastian Echegaray, PhD • For the Group[1]*

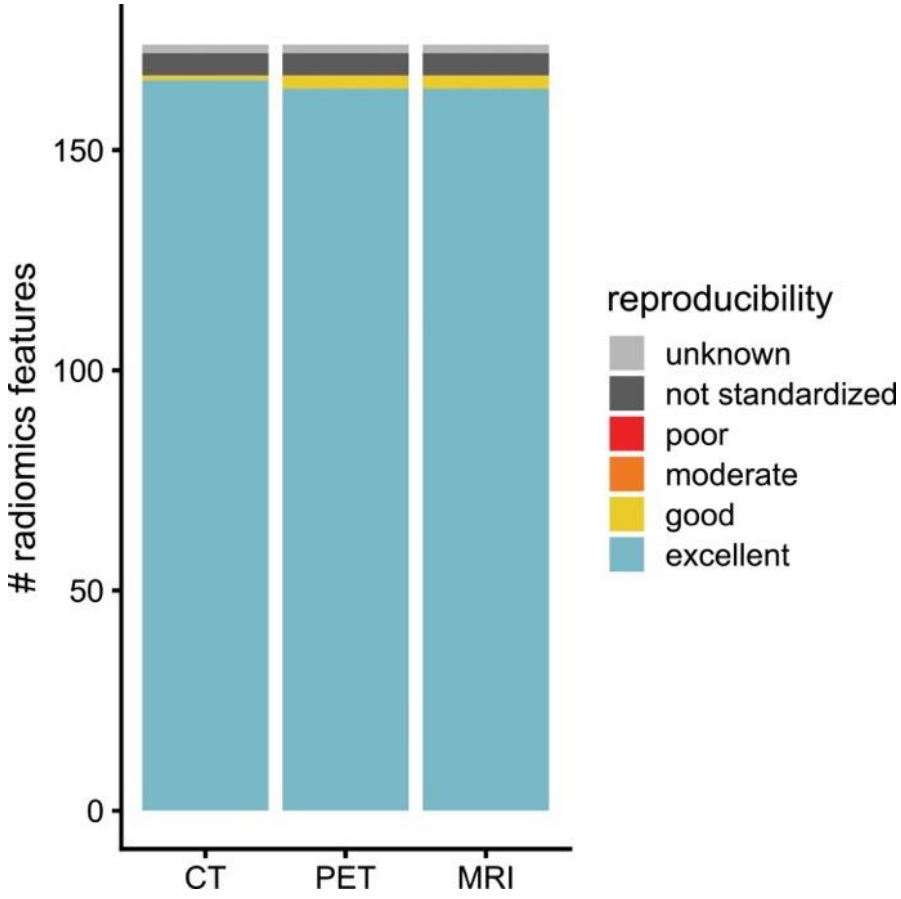

Zwanenburg et al, Radiology 2020

Models can be explained with high spatial resolution

Deep learning activation maps

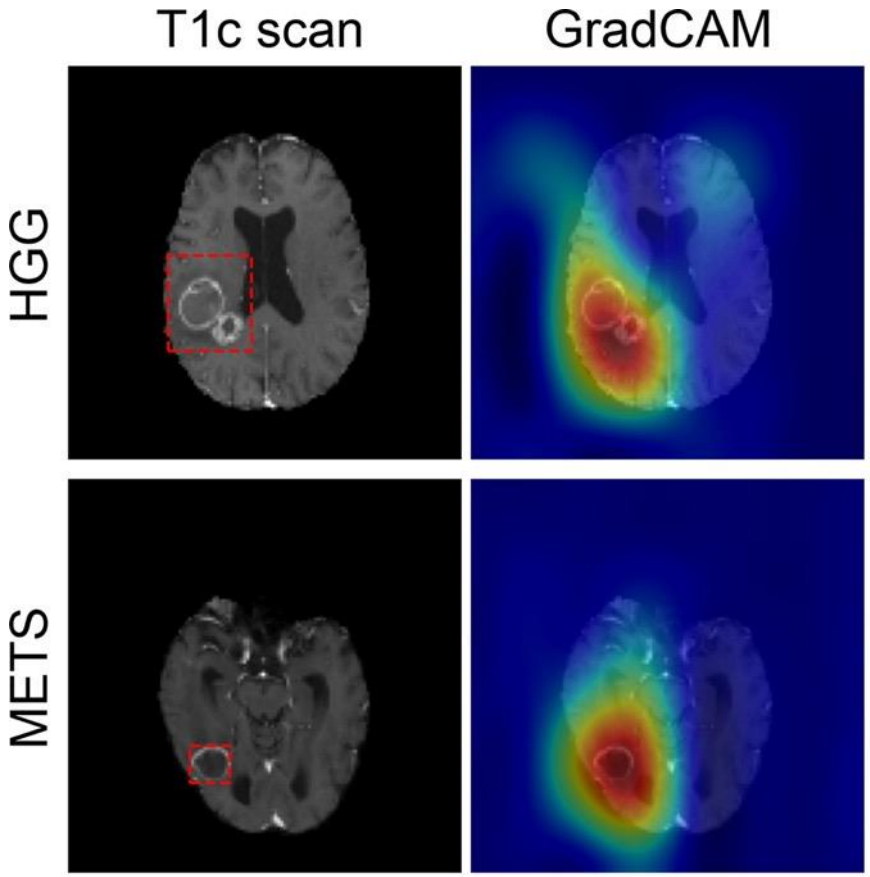

Chakrabarty et al, Radiology AI 2021

Radiomic activation maps

local

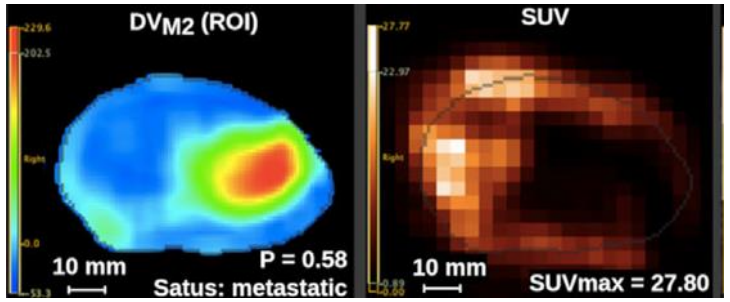

Escobar et al, Med Phys 2022

whole-body

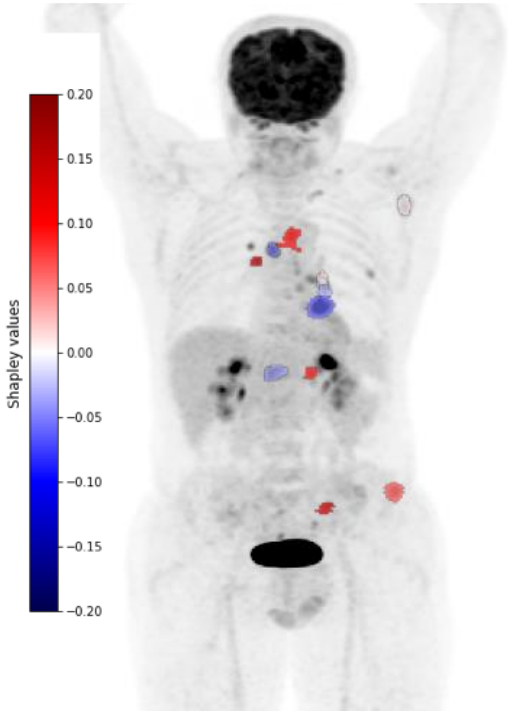

Captier et al, SNMMI 2023

Leveraging deep learning for radiomics

Deep learning

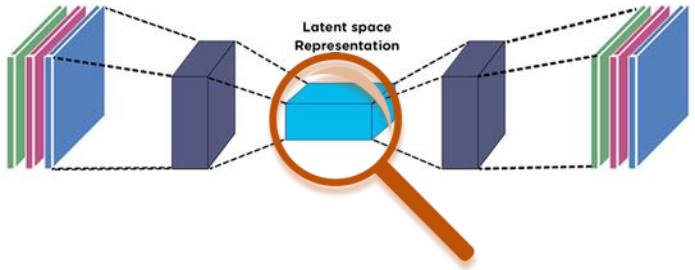

1. Decipher informative deep features and interpret model

2. Validate model interpretation using dedicated experiments

Radiomics

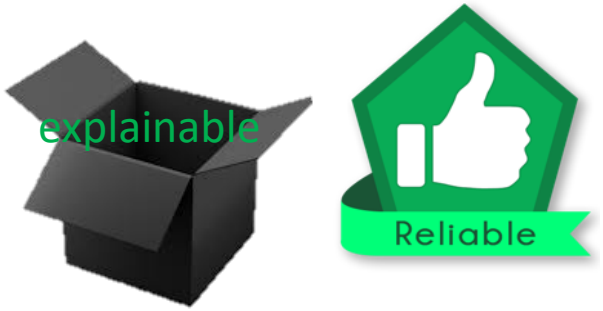

3. Re-engineer model to make it explainable and more robust

Robust model and new biological/medical knowledge

Should Deep Learning Replace Radiomics?

Abhinav Jha, PhD
Washington University in St. Louis

Context for my arguments

We conducted a survey among patient-advocate groups to capture their thoughts on machine learning for clinical-decision making*

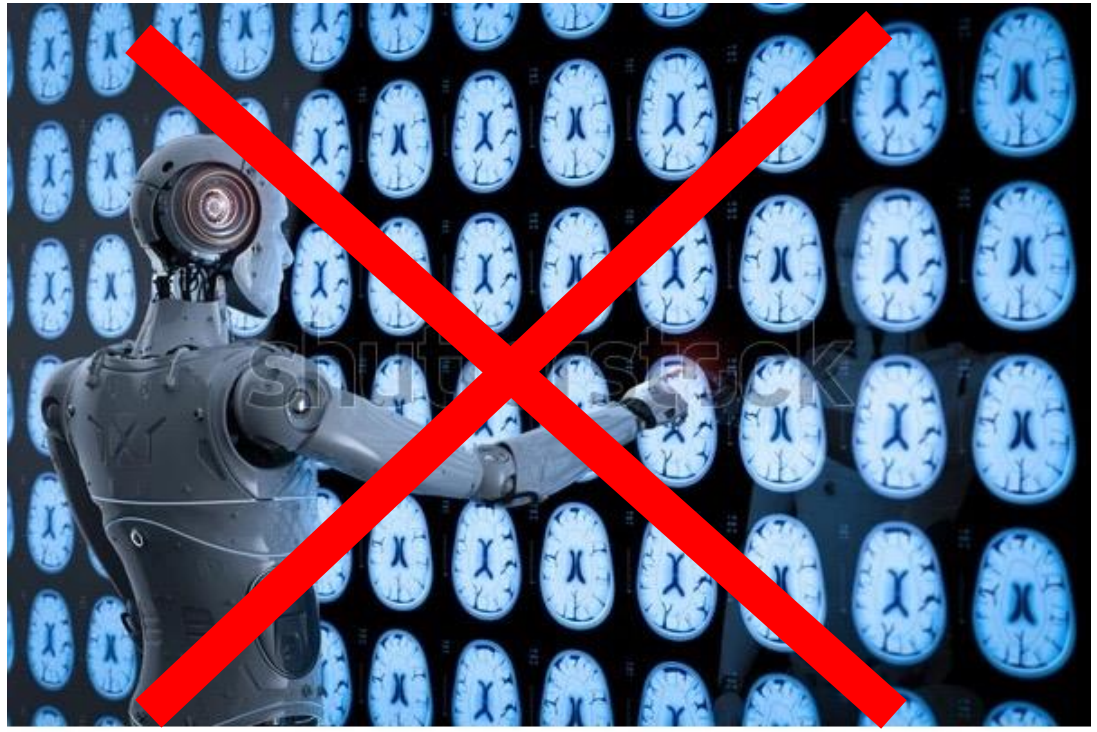

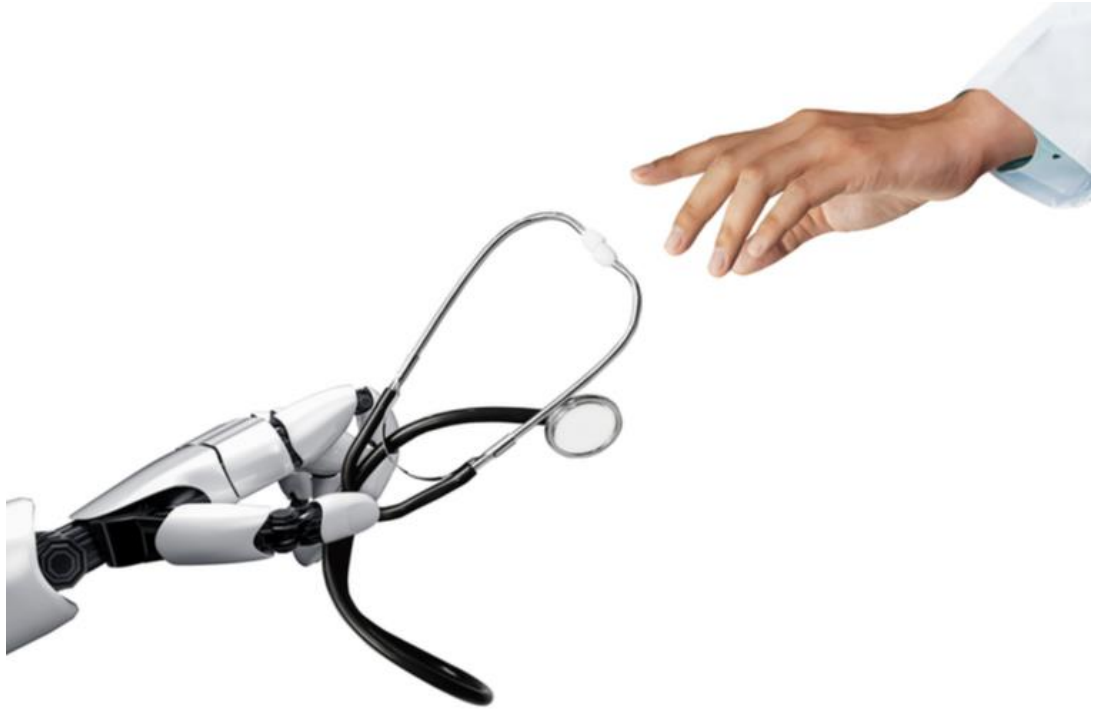

Patients want machine learning, but to help physicians*

*Birch et al, Nature Medicine, 2022

*Photo credit: Shutterstock

Desired properties in computer-aided tools that can help physicians

- Tool should be reliable and reproducible
- Less burdensome for the physicians to use the tool
- The tool should complement physicians, identifying features that may be difficult to conceive manually

Potentially more reproducible and reliable

Time to embrace deep learning?

Less burdensome for physicians

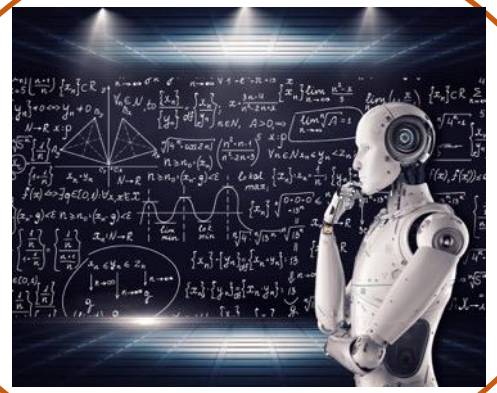

Can learn from large datasets and identify hidden features

Potentially more reproducible and reliable

Time to embrace deep learning?

Less burdensome for physicians

Ability to learn from large datasets and identify hidden features

Radiomics: What are we quantifying?

The original lesion

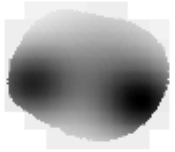

PET system

Noisy sinogram

Reconstruction

Reconstructed lesion image

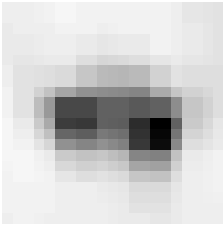

Ideal goal: Quantify features of the lesion

Not in AI ?

Reality: Quantify features of the lesion image*

- Typically, in radiomics, we quantify features of the "image of the abnormality"*.
- These features may simply arise due to noise and other image-degrading processes. This puts a question on the biological interpretability of these features.

Eur Radiol. 2021; 31(1): 1–4.
Published online 2020 Aug 7. doi: 10.1007/s00330-020-07108-w
PMCID: PMC7755615
PMID: 32767103

A decade of radiomics research: are images really data or just patterns in the noise?

Daniel Pinto dos Santos,[1] Matthias Dietzel,[2] and Bettina Baessler[3]

> Eur J Nucl Med Mol Imaging. 2013 Jun;40(6):967-8. doi: 10.1007/s00259-013-2381-3. Epub 2013 Mar 23.

Area under the cumulative SUV-volume histogram is not a viable metric of intratumoral metabolic heterogeneity

Frank J Brooks

*Barrett et al, Phys. Med. Biol. 2016

Radiomics: The sensitivity to measurement process

- Medical image databases are heterogeneous with scanner and imaging protocol variability
- Radiomic features: Sensitive to these variations[1,2]

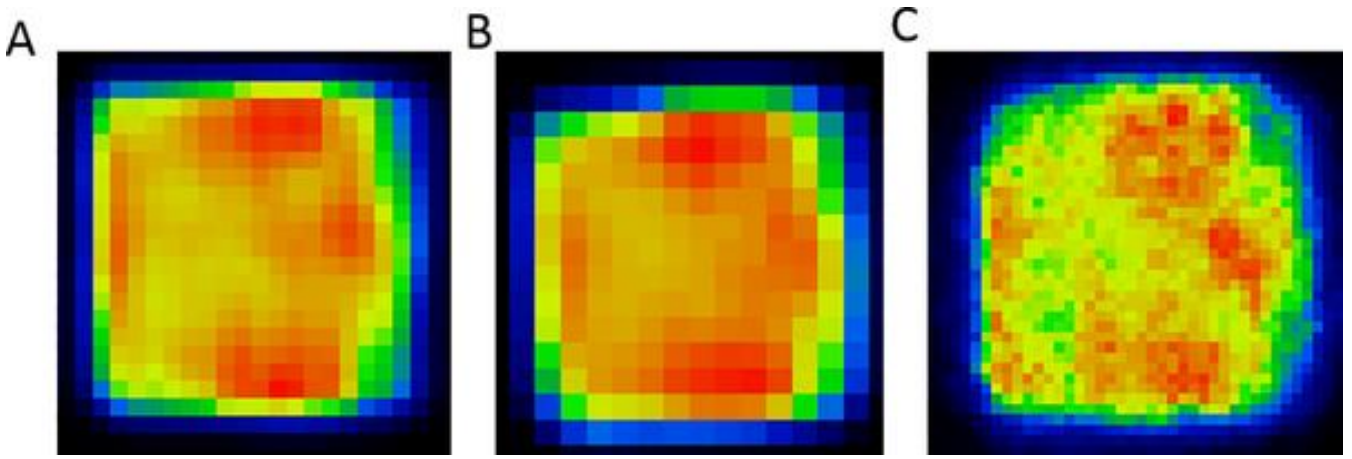

Are AI models not sensitive to such variations?

Representative transaxial slices of the **same heterogeneous lesion** measured and reconstructed by **three different scanners** (A) GE Discovery MI PET/CT, (B) Mediso AnyScan PET/CT, (C) Mediso nanoScan PET/MRI*

[1]Nyflot et al, J Med. Imag. 2016
[2]Pfaehlr et al, Med. Phys. 2018

*Image source: Forgacs et al, Plos One, 2019

Deep learning: Potentially more reproducible

- The heart of deep learning: Universal approximation theorem

  Give me enough data, I will learn to mimic most functions

- With enough data, deep learning can potentially model heterogeneities due to scanner and imaging protocol variability

JACC Cardiovasc Imaging. Author manuscript; available in PMC 2019 Nov 1.
Published in final edited form as:
JACC Cardiovasc Imaging. 2018 Nov; 11(11): 1654–1663.
Published online 2018 Mar 14. doi: 10.1016/j.jcmg.2018.01.020

PMCID: PMC6135711
NIHMSID: NIHMS939910
PMID: 29550305

Deep Learning for Prediction of Obstructive Disease from Fast Myocardial Perfusion SPECT: A Multicenter Study

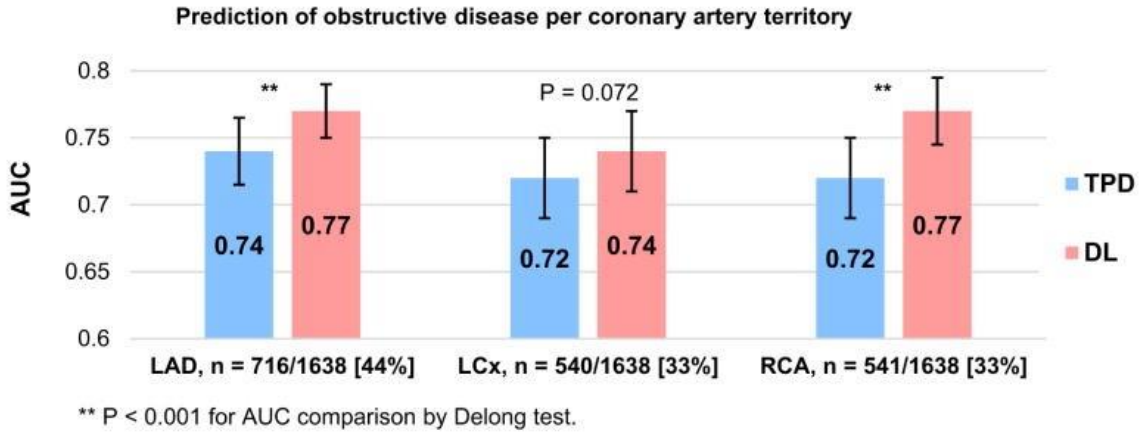

1638 patients and task automation

AUC (and 95% CI) for left anterior descending (LAD), left circumflex (LCx) and right coronary arteries (RCA) artery disease prediction by per-vessel TPD and by deep learning using raw and quantitative perfusion polar maps.

Potentially more reproducible and reliable

Time to embrace deep learning?

Less burdensome for physicians

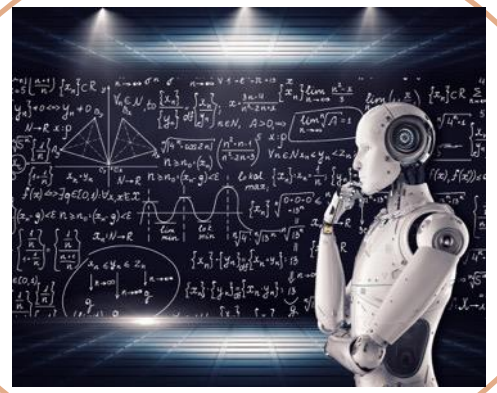

Ability to learn from large datasets and identify hidden features

Deep learning can be less burdensome for physicians

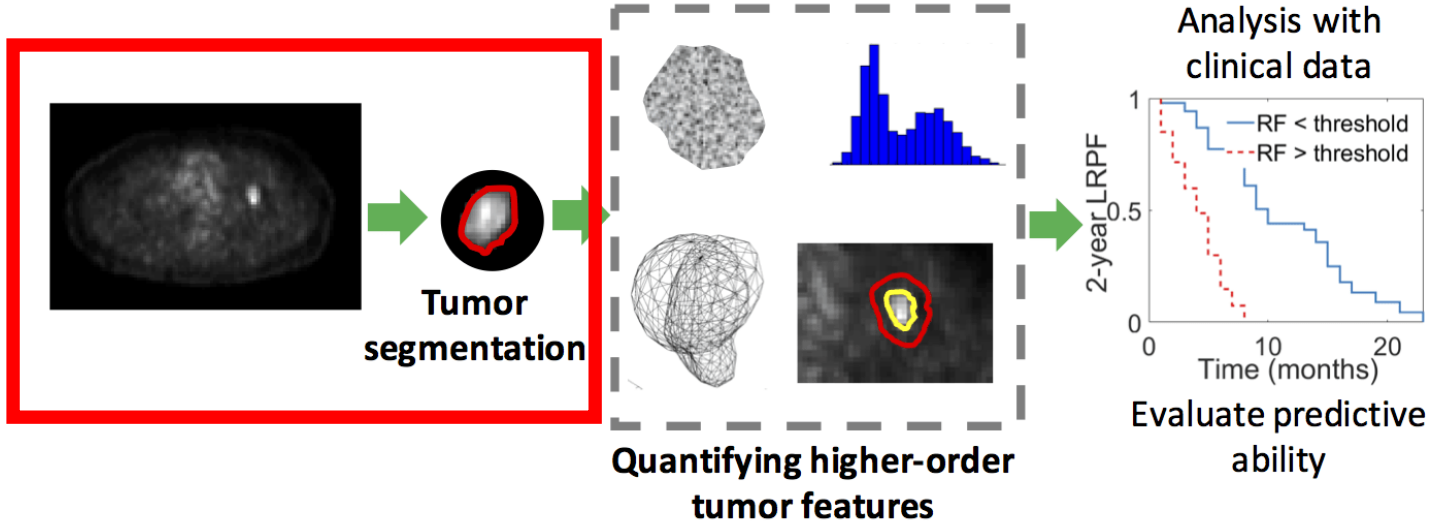

- In radiomics, burden to segment the tumor accurately may fall on the physician: A tedious and time-consuming process that also introduces variability
- An end-to-end deep-learning approach does not require such manual intervention: More convenient for physicians

But segmentation can now be automated using DL !

Potentially more reproducible and reliable

Time to embrace deep learning?

Less burdensome for physicians

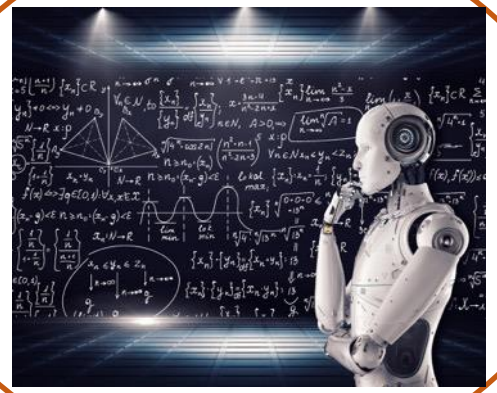

Ability to learn from large datasets and identify hidden features

Radiomic features are manually conceived, not really hidden

Understanding Changes in Tumor Texture Indices in PET: A Comparison Between Visual Assessment and Index Values in Simulated and Patient Data

Fanny Orlhac, Christophe Nioche, Michaël Soussan and Irène Buvat

Journal of Nuclear Medicine March 2017, 58 (3) 387-392; DOI: https://doi.org/10.2967/jnumed.116.181859

Yes, useful for as a discovery approach !

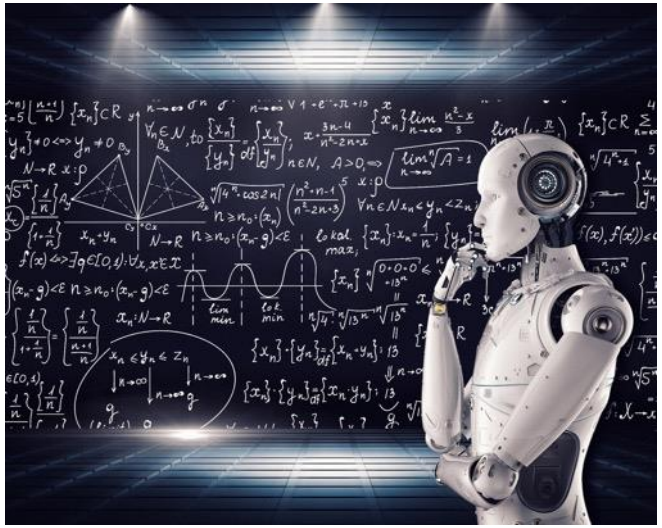

With deep learning, we can identify hidden features in tumors, other portions of images, other patient images, and clinical data

Identifying deep “hidden” features can also yield improved performance

Model		AUC
Image-only CNN	Intra	0.767
	Peri	0.850
	Cmb	0.950
Image-only radiomics	Intra	0.533
	Peri	0.533
	Cmb	0.833

Deep learning could identify hidden features from high-dimensional large datasets that would manually be challenging to conceive

Not sure !

*Sun et al, Front Oncol, 2020

And then there is research on explainability of these features

Be careful, this study does not assess the impact of explainability

Prospective study (N = 240 patients) to assess impact of explainable DL on physician interpretation of myocardial perfusion SPECT images*

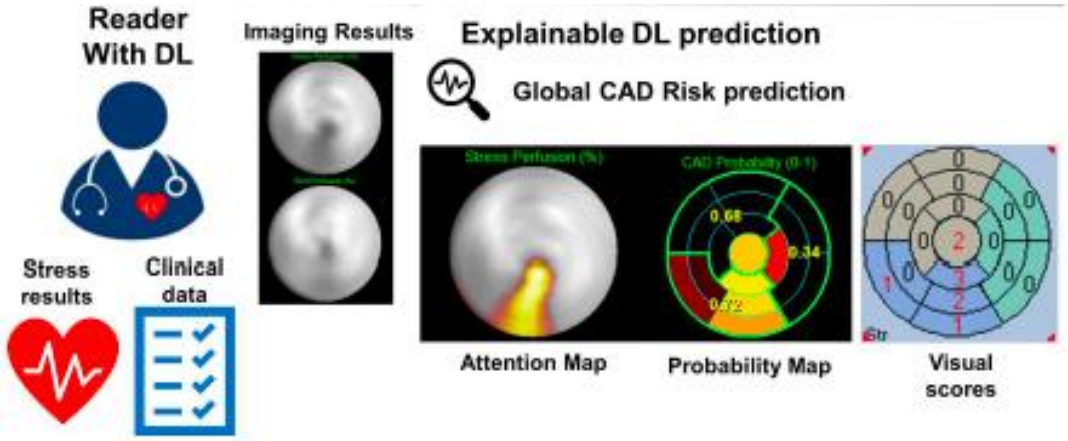

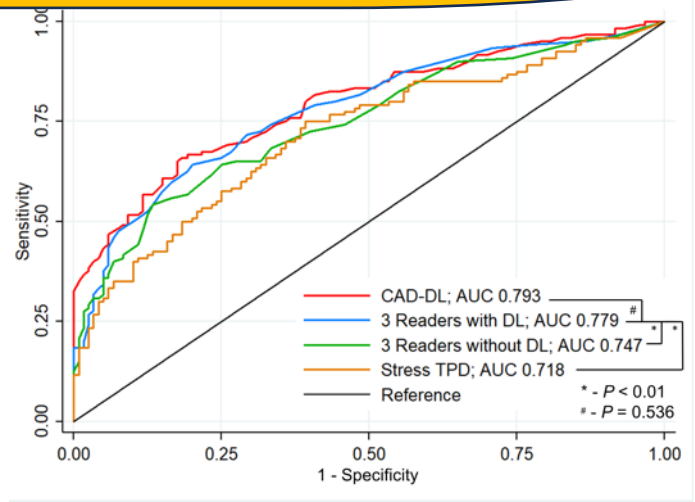

AUC for each of the three readers was increased when using explainable DL

Explainable AI improved physician interpretation of myocardial perfusion SPECT*

Deep learning could thus complement the physicians!

*Miller et al, J. Nuc. Med., 2022